2016

Near-Field Electromagnetic Interactions in SWNT/REI Complexes

Benjamin Sofka
Lehigh University

Near-Field Electromagnetic Interactions in SWNT/REI Complexes

by

Benjamin J. Sofka

A Dissertation
Presented to the Graduate Committee
of Lehigh University
in Candidacy for the Degree of
Doctor of Philosophy
in
Physics

Lehigh University
September 4, 2016

Approved and recommended for acceptance as a dissertation in partial fulfillment of the requirements for the degree of Doctor of Philosophy.

Benjamin J. Sofka
Near-Field Electromagnetic Interactions in SWNT/REI Complexes

---

Defense Date

Slava V. Rotkin, Dissertation Director, Chair

Accepted Date

Committee Members

Volkmar Dierolf

Ivan Biaggio

Michael Stavola

W. Beall Fowler

Anand Jagota

Dedication

First, I would like to express my gratitude to my fiancée Sarah who has stuck with me through the whole process. Thank you for putting up with late nights, working weekends, not eating dinner until 9 or 10 o'clock some nights waiting for me, and dealing with me being annoyed and frustrated when something in my research was not going right. You've supported me through the entire process with all its ups and downs and I couldn't have done it without you.

I also couldn't have done this without the full support of my family (and soon to be family). To my family: Mom, Dad, Holly, Pop-pop, Auntie - thank you for being understanding and putting up with my hectic schedule. With working late nights and weekends, we didn't get to see each other as often as I wanted to. You've rooted me on from the beginning and I'm grateful to have your support. Nana and Grammy - I know you'd both be proud of me. Also a huge thank you to my soon to be family: Russell, Linda, Ellen, Paul, Rachael, Jeff, Jason, Justin, Cortney, Jaimy, and Josh; and the kids (they were kids when I started grad school...): Haylee, Brayden, Natalya, Jocelyn, Bryanna, Julianne, and Jenna. Your support meant a lot to me. And Jocelyn, your "JoJo waz here" drawing is still on my whiteboard.

I would also like to thank many of the faculty members here at Lehigh. I'll start with my advisor, Dr. Slava V. Rotkin - you've pushed me to become a better physicist. I began in this group with no previous theoretical experience and no prior knowledge of what a carbon nanotube was (other than it was a nano-sized tube of carbon) and you were patient while I got over the learning curve. You gave me the freedom to find my own research path but helped steer my research in the right direction when I started veering off course. You challenged me to be the best

researcher I could be.

I would like to thank the members of my committee for all of their help: Dr. Volkmar Dierolf, Dr. Ivan Biaggio, Dr. Michael Stavola, Dr. W. Beall Fowler, and Dr. Anand Jagota. They always helped keep things on track in my committee meetings and made sure I didn't get caught up in the little details that I forgot the big picture of what was going on. Their research suggestions were always helpful, as well. If I was stuck, someone always had a suggestion on how to get past it and it always worked. And any time I had a question, their doors were always open.

There are also other physics faculty members who helped me along the way include and deserve thanks. Thanks go to Dr. John Huennekens for all his graduate advising knowledge, helping to make sense of Jackson's E&M textbook, and pitching our summer softball team, the Psi Stars, to two straight summer league titles. To Dr. Gary DeLeo for allowing me to accompany him on outreach visits, for enlightening and entertaining conversations about TV and movies, and for being there to listen and help give advice when things weren't going smoothly. Dr. Yong Kim and Dr. Jim Gunton - thanks for always asking how things were going every time I ran into you in the hallway.

I would also like to extend my thanks to my undergraduate professors at Moravian College: Mr. Joseph Powlette, Dr. Kelly Krieble, and Dr. Edward Roeder for all of their help and support. I couldn't have been more prepared for what I have faced thanks to everything you've done for me. I'd especially like to thank Dr. Roeder and Mr. Powlette for independently pulling me aside in freshman physics and convincing me that I should pursue physics as a career. Both of you saw something in me and I wouldn't be here getting my Ph.D. in physics if it weren't for your belief in me.

I would, of course, like to thank the members of my group: Dr. Massooma Pirbhai, Michael Blades, Dr. Tetyana Ignatova, Dan You, and Dr. Andrei Nemelentsau. Grad school is less stressful when you're surrounded by awesome people. Thanks to Massooma for organizing group lunches where we could all get together and destress. All of you were always there to listen and offer whatever advice you could to try to help whenever something wasn't working right. We have a very tight-knit

group and we just want each other to succeed.

I couldn't have asked for a better group of people to get through all of the coursework and the qualifiers with than the other grad students in my year: Brandon Mitchell, Kebra Ward, Kara Richter, and Donovan Ruth. Whether it was staying until 10pm working on Jackson's E&M problems or spending our entire Winter Break in the conference room going over old qualifier exams and memorizing stacks of equation note cards, we all got through it together.

Finally, I would also like to thank the other grad students who were always there for a good laugh. Thanks to Dr. Josh Jones for our intellectual discussions and tastings of whiskey, for hallway golf with Carl's clubs (sorry Carl), and for being an awesome shortstop for turning double plays with in softball. Thanks to Phil and Gaby Weiser for being awesome and supportive. Both of you will be done soon! Vinnie Zoutenbier - thanks for always being punny and making everyone crack a smile. And Natalie Hernandez for stopping by to see Massooma but ending up having to talk to me instead.

Thank you, everyone, for all that you have done. This was not a journey I went on alone.

Contents

List of Tables

List of Figures

Abstract

We theoretically study the near-field electromagnetic effects of a single-walled carbon nanotube (SWNT) antenna. We develop a model for plasmon resonances on the SWNT surface by treating the SWNT as a transmission line (TL). By defining TL parameters such as resistance, capacitance, and inductance per unit length of the SWNT antenna, we effectively model the plasmon resonances which have fundamental modes in the THz frequency range.

We also include excitonic effects into our SWNT antenna to model the antenna response in the visible/NIR frequency range. A quasi-classical expression for the excitonic conductivity is derived. From Maxwell's equations, an integral equation for the induced current distribution due to an external field is solved. The scattered field from the excitonic antenna can be calculated from the current distribution and localized hotspots are observed. By placing rare earth ions (REIs) in the local hotspots of the SWNT antenna, we can calculate the excitation enhancements of multiple REI transitions and multiple chirality SWNT antennas. REI excitation enhancements ranging from 1-200% are calculated. Evidence of exciton-polariton modes due to the coupling of photons to the antenna resonances are also observed. These modes are allowed when the real part of the complex dielectric function is negative. The polariton modes follow a π/L wave vector dependence.

Chapter 1

Introduction

1.1 Carbon Nanotubes

1.1.1 Uses and Applications

Carbon nanotubes (CNTs) were theoretically proposed long before they were experimentally discovered. In 1959, Roger Bacon visualized graphite whiskers which were helically wrapped graphene sheets [16]. In 1990, Richard Smalley, who won the 1996 Nobel Prize in Chemistry for the discovery of buckminsterfullerenes [17], or "buckyballs," proposed that if buckyballs get big enough, they could potentially form cylinders. Then, in 1991, CNTs were first experimentally discovered by Sumio Iijima [18]. In his work, he took high resolution electron micrographs from a transmission electron microscope (TEM) which showed lattice fringes - multiple parallel lines on the image which were symmetric about the center. He came to the conclusion that what he was seeing were cross sections of a multi-walled tubular structure of rolled graphene. Since their experimental discovery, CNTs have been the focus of many scientific studies to learn about their unique optical and electronic properties, as well as applications of these materials to many fields of science and engineering.

Lately, single-walled carbon nanotubes (SWNTs) have shown increased interest in the fields of medical and bio-imaging. Many different types of SWNT sensor devices have been developed including transistor based sensors [19, 20], electrochemical

sensors [21, 22, 23], single defect sensors [24, 25, 26], and even sensors on fabric [27]. Label-free bio-imaging was also achieved using SWNTs [28, 29, 30, 31].

Even more recently, SWNT emission energy was measured to shift when in the presence of the electrostatic potential of the cell surface [12]. Understanding the interaction between SWNT excitations and the electrostatic environment are crucial for developing SWNT bio-sensors. SWNT sensors have been used as a label-free detector of cardiac troponin T (cTnT), which is is a biomarker used as a standard indicator of heart attacks [32]. SWNTs have also been used to characterize the permeability of living multicellular environments such as tumor spheriods [33]. A hyperspectral imaging technique was also developed to image single SWNT fluorescence in live cells [34].

1.1.2 Structure

The structure of carbon nanotubes begins with a single sheet of graphene. Graphene is a single layer sheet of carbon atoms arranged in a hexagonal lattice structure [8]. Figure 1.1 shows the different carbon materials that graphene can form [8]. It can be rolled into a 0D "buckyball", rolled into a 1D nanotube, or stacked to form 3D graphite. A single-walled carbon nanotube (SWNT) is a single layer of graphene rolled into a cylinder as shown in the middle of Figure 1.1. As you could imagine, there are many different ways to roll a sheet of graphene into a cylinder. The optical and electronic properties of the SWNT are determined by how the graphene sheet is rolled. SWNTs can be either semiconducting, semi-metallic, or metallic in nature depending on how the graphene sheet is rolled. Figure 1.2 shows the unit cell of a SWNT projected onto the flat surface of a graphene sheet. The unit cell of graphene contains two equivalent carbon atoms. The unit vectors $(\mathbf{a}_1, \mathbf{a}_2)$ of the unit cell are indicated and project the equivalent carbon atoms to the next. The length of the unit vector is $a = \sqrt{3}a_{c-c} = 2.49$ Å with the carbon-carbon distance in graphene $a_{c-c} = 1.44$ Å. To roll up a flat sheet of graphene, we must define two vectors. $\mathbf{C}_h$ is the chiral vector whose length becomes the circumference of the SWNT when rolled and $\mathbf{T}$ is the translational vector which is directed along the SWNT axis. The chiral

vector can be expressed by integer multiples of the unit vectors as

$$\mathbf{C}_h = n\mathbf{a}_1 + m\mathbf{a}_2 = (n, m) \tag{1.1}$$

where n and m are integers. These indices are used to label (n, m) SWNTs. If $n = m$, we classify that type of nanotube to be "armchair", if $m = 0$, we classify that nanotube as zigzag, and the general case of n and m being different integers is classified as "chiral". These three classifications can be seen in Figure 1.3 and are listed in Table 1.1.

Type	θ	$\mathbf{C}_h$
armchair	30°	(n, n)
zigzag	0°	$(n, 0)$
chiral	$0^\circ < \|\theta\| < 30^\circ$	(n, m)

Table 1.1: Classification of carbon nanotubes [1].

The (n, m) indices determine many of the properties of the SWNT. They determine the diameter of the SWNT. The diameter is related to the length of the chiral vector

$$d = |\mathbf{C}_h|/\pi = \frac{a}{\pi}\sqrt{n^2 + m^2 + nm} \tag{1.2}$$

The indices also determine if the SWNT is semiconducting or metallic. If the GCD($n - m$,3) = 1, then the SWNT is a semiconductor, but if the GCD($n - m$,3) = 3 the SWNT is metallic. Here, GCD means the greatest common divisor.

SWNTs are quasi-1D structures due to their large length/diameter aspect ratio of the cylinder, which can be as high as $10^4 - 10^5$. SWNTs have diameters ranging from approximately 0.5 - 2 nm, while multi-walled carbon nanotubes can have diameters much larger. The lengths of SWNTs can vary between tens of nanometers up to centimeters in length.

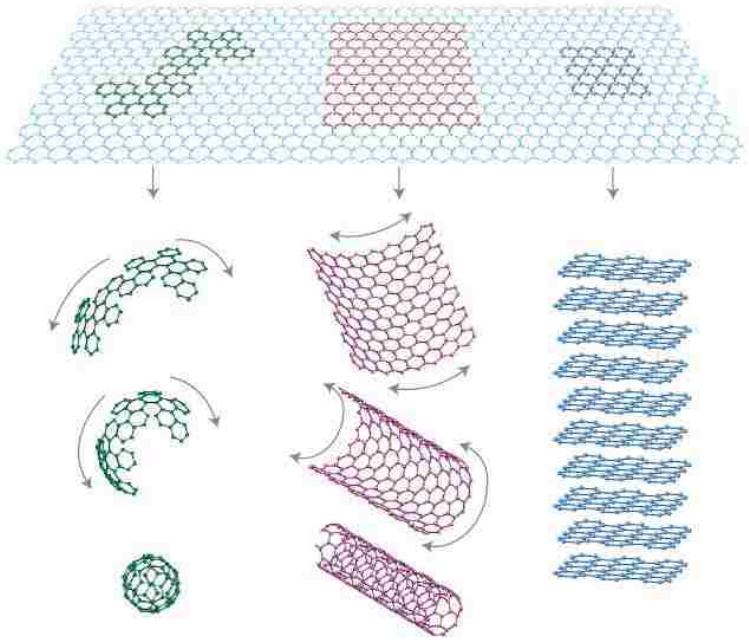

Figure 1.1: Graphene as a 2D building material for carbon structures. It can be wrapped into a 0D buckyball, a 1D SWNT, or stacked into 3D graphite [8].

1.1.3 Single Particle Electronic Structure

The electronic structure of SWNTs begins with that of 2D graphene. For a single sheet of graphene, three σ bonds hybridize in the sp^2 configuration which forms the in-plane bonds. These are from the $2s$, $2p_x$, and $2p_y$ orbitals of each carbon atom in the graphene unit cell (2 atoms - 6 orbitals). The leftover $2p_z$ orbitals are perpendicular to the graphene plane and form the covalent π bonds. These π energy bands are what determines the electronic properties of graphene, as well as SWNTs.

Due to the translational symmetry of the lattice, any wave function of the electron must satisfy Bloch's theorem [1]

$$T_{\mathbf{a}_i}\Psi = e^{i\mathbf{k}\cdot\mathbf{a}_i}\Psi \tag{1.3}$$

where $T_{\mathbf{a}_i}$ is a translational operation along the lattice vector $\mathbf{a}_i$ and $\mathbf{k}$ is the wave vector. One functional form of the wave function that satisfies Equation (1.3) is the

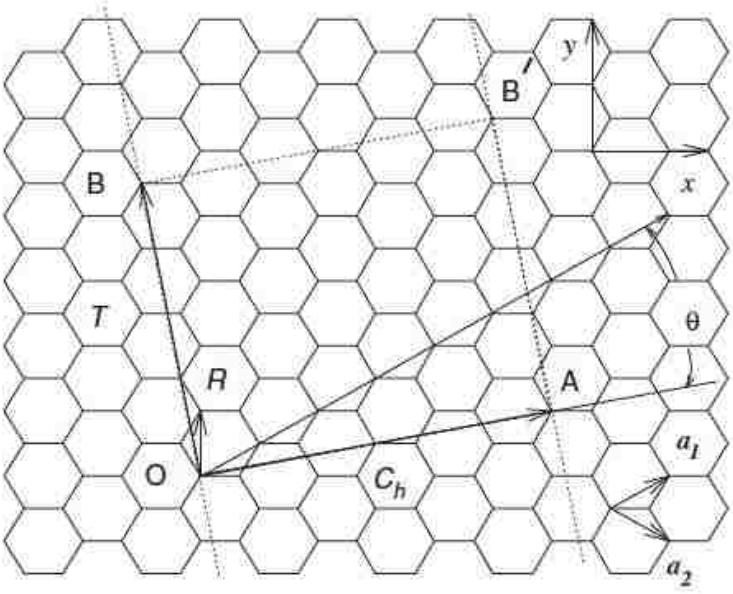

Figure 1.2: Unit cell of a SWNT projected onto a flat graphene surface. The unit vectors $(\mathbf{a}_1, \mathbf{a}_2)$ of the unit cell are indicated. $\mathbf{C}_h$ is the chiral vector whose length becomes the circumference of the SWNT when rolled, $\mathbf{T}$ is the translational vector which is directed along the SWNT axis, $\mathbf{R}$ is a symmetry vector, and θ is the chiral angle. The unit cell is given by the rectangle made by $\mathbf{C}_h$ and $\mathbf{T}$ [9].

tight binding Bloch function

$$\Phi_j(\mathbf{k}, \mathbf{r}) = \frac{1}{\sqrt{N}} \sum_{\mathbf{R}}^{N} e^{i\mathbf{k}\cdot\mathbf{R}} \phi_j(\mathbf{r} - \mathbf{R}), \quad (j = 1, \cdots, n). \tag{1.4}$$

Here, $\mathbf{R}$ is the position of the atom and ϕ_j denotes the atomic wave function in state j. The eigenfunctions satisfying Equation (1.3) are a linear combination of Bloch wave functions

$$\Psi_j(\mathbf{k}, \mathbf{r}) = \sum_{j'=1}^{n} C_{jj'}(\mathbf{k}) \Phi_{j'}(\mathbf{k}, \mathbf{r}) \tag{1.5}$$

The electronic structure comes from solving the secular equation, which is the eigenvalue equation

$$\det[\mathcal{H} - E\mathcal{S}] = 0 \tag{1.6}$$

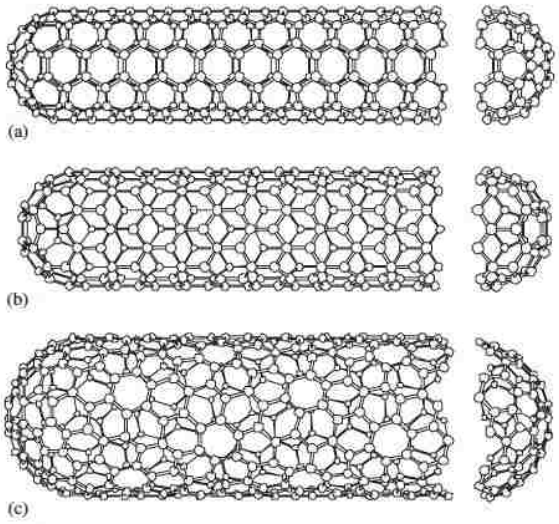

Figure 1.3: Schematic diagram of the three types of SWNTs. (a) is the metallic armchair tube; (b) is the zigzag tube which can be either semiconducting or metallic; and (c) the chiral nanotube which can also be either semiconducting or metallic [9].

which gives all n eigenvalues of $E_j(\mathbf{k}), (j = 1, \cdots, n)$ for a given $\mathbf{k}$. The $j-$th eigenvalue can be expressed as

$$E_j(\mathbf{k}) = \frac{\langle \Psi_j | \mathcal{H} | \Psi_j \rangle}{\langle \Psi_j | \Psi_j \rangle} = \frac{\int \Psi_j^* \mathcal{H} \Psi_j d\mathbf{r}}{\int \Psi_j^* \Psi_j d\mathbf{r}} \tag{1.7}$$

Substituting Equation (1.5) into Equation (1.7) and making a change in subscripts, we get

$$E_i(\mathbf{k}) = \frac{\sum_{j,j'=1}^{n} C_{ij}^* C_{ij'} \langle \Psi_j | \mathcal{H} | \Psi_{j'} \rangle}{\sum_{j,j'=1}^{n} C_{ij}^* C_{ij'} \langle \Psi_j | \Psi_{j'} \rangle} = \frac{\sum_{j,j'=1}^{n} \mathcal{H}_{jj'}(\mathbf{k}) C_{ij}^* C_{ij'}}{\sum_{j,j'=1}^{n} \mathcal{S}_{jj'}(\mathbf{k}) C_{ij}^* C_{ij'}} \tag{1.8}$$

where we can define the transfer integral and overlap integral matrices, respectively, as

$$\mathcal{H}_{jj'}(\mathbf{k}) = \langle \Phi_j | \mathcal{H} | \Phi_{j'} \rangle, \ \mathcal{S}_{jj'}(\mathbf{k}) = \langle \Phi_j | \Phi_{j'} \rangle \ \ (j, j' = 1, \cdots, n) \tag{1.9}$$

For 2D graphene, the $2p_z$ orbitals of the two carbon atoms in the unit cell provide the basis functions for the wave function. In the graphene unit cell, there are two

inequivalent carbon atoms, A and B. Due to the hexagonal arrangement of the carbon atoms, each A atom is bonded with three B atoms, and likewise each B atom is bonded to three A atoms. For the dispersion calculation, we consider the case of the nearest neighbor interactions. In this approximation, we assume that each A atom only interacts with the three nearest B atoms it is bonded to and each B atom only interacts with the three neighboring A atoms. Therefore, our transfer and overlap matrices can be reduced to 2 x 2 matrices. The diagonal terms of the transfer matrix, $\mathcal{H}_{AA}$ and $\mathcal{H}_{BB}$, involve integration over a single atom so that $\mathcal{H}_{AA} = \mathcal{H}_{BB} = \epsilon_{2p}$. For the off diagonal matrix elements, we need to consider the three nearest-neighbor B atoms relative to an A atom which are denoted by the vectors R_1, R_2, and R_3. Then,

$$\begin{aligned} \mathcal{H}_{AB} &= \gamma_0 \left(e^{i\mathbf{k}\cdot\mathbf{R}_1} + e^{i\mathbf{k}\cdot\mathbf{R}_2} + e^{i\mathbf{k}\cdot\mathbf{R}_3} \right) = \gamma_0 \left(e^{ik_x a/\sqrt{3}} + 2e^{-ik_x a/2\sqrt{3}} \cos\left(\frac{k_y a}{2}\right) \right) \\ &= \gamma_0 f(k) \end{aligned} \tag{1.10}$$

where γ_0 is the value of the transfer integral ($\approx 2.7 - 3$ eV), and we have used the unit vectors of the graphene hexagonal lattice

$$\mathbf{a}_1 = \left(\frac{\sqrt{3}}{2}a, \frac{a}{2} \right), \ \mathbf{a}_2 = \left(\frac{\sqrt{3}}{2}a, \frac{-a}{2} \right) \tag{1.11}$$

where $a = \sqrt{3}a_{C-C} = 0.249$ nm is the length of the graphene unit vector. Note here also that $\mathcal{H}_{AB} = \mathcal{H}^*_{BA}$. The matrices can be expressed as

$$\mathcal{H} = \begin{pmatrix} \epsilon_{2p} & \gamma_0 f(k) \\ \gamma_0 f^*(k) & \epsilon_{2p} \end{pmatrix}$$

and

$$\mathcal{S} = \begin{pmatrix} 1 & sf(k) \\ sf^*(k) & 1 \end{pmatrix}$$

where s is the value of the overlap integral as in Equation (1.9). For the case where the overlap integral, s, becomes zero (Slater-Koster scheme), the expression for the electronic structure for the graphene layer, from the secular equation in Equation

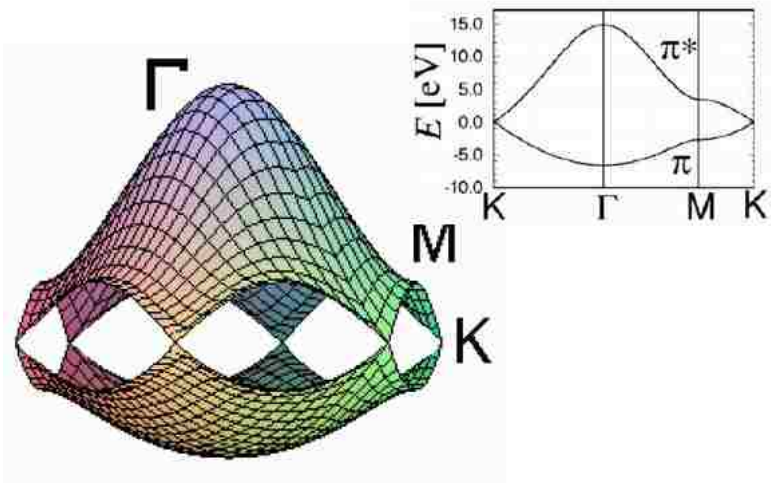

Figure 1.4: Energy dispersion of 2D graphene in the Brillouin zone [9].

(1.6), takes a simple form

$$E_{g2D}(k_x, k_y) = \pm\gamma_0 \left[1 + 4\cos\left(\frac{\sqrt{3}k_x a}{2}\right)\cos\left(\frac{k_y a}{2}\right) + 4\cos^2\left(\frac{k_y a}{2}\right)\right]^{1/2} \quad (1.12)$$

Now that we have the electronic structure of graphene, we can analyze the electronic structure of SWNTs. To account for the rolling of the graphene sheet, we must use periodic boundary conditions in the circumferential direction denoted by $\mathbf{C}_h$. By doing this, the wave vector associated with the azimuthal direction becomes quantized, while the wave vector in the axial direction (along $\mathbf{T}$) remains continuous for an infinite tube. Therefore, the energy bands of SWNTs are a set of one dimensional energy dispersion relations which are cross sections of 2D graphene. The 1D dispersion relations after performing the zone folding scheme are

$$E_\mu(q) = E_{g2D}\left(q\frac{\mathbf{K}_2}{|\mathbf{K}_2|} + \mu\mathbf{K}_1\right), \ (\mu, 0, \cdots, N-1) \text{ and } \left(\frac{-\pi}{T} < q < \frac{\pi}{T}\right) \quad (1.13)$$

where N is the number of hexagons in the unit cell given by

$$N = \frac{2(n^2 + m^2 + nm)}{GCD(2n + m, 2m + n)}, \quad (1.14)$$

T is the length of the translational vector given by

$$T = \frac{\sqrt{3}a\sqrt{n^2 + m^2 + nm}}{GCD(2n + m, 2m + n)}, \tag{1.15}$$

μ is the quantized azimuthal quantum number, and $\mathbf{K}_1$ and $\mathbf{K}_2$ are the reciprocal lattice vectors for the circumferential and axial directions, respectively.

To obtain analytic expressions for the dispersion of SWNTs, we first consider the nanotubes with the highest symmetry: armchair and zigzag. For armchair SWNTs,

$$\begin{aligned} E^a_\mu(q) &= \pm\gamma_0 \left[1 \pm 4\cos\left(\frac{\mu\pi}{n}\right)\cos\left(\frac{qa}{2}\right) + 4\cos^2\left(\frac{qa}{2}\right)\right]^{1/2} \\ &\quad (-\pi < qa < \pi),\ (\mu = 1, \cdots, 2n) \end{aligned} \tag{1.16}$$

and for zigzag SWNTs,

$$\begin{aligned} E^z_\mu(k) &= \pm\gamma_0 \left[1 \pm 4\cos\left(\frac{\sqrt{3}qa}{2}\right)\cos\left(\frac{\mu\pi}{n}\right) + 4\cos^2\left(\frac{\mu\pi}{n}\right)\right]^{1/2} \\ &\quad (-\pi/\sqrt{3} < qa < \pi/\sqrt{3}),\ (\mu = 1, \cdots, 2n) \end{aligned} \tag{1.17}$$

Figure 1.5 shows the calculated dispersion of a (11,11) armchair SWNT calculated from Equation (1.16). Since all armchair SWNTs are metallic, there is no band gap between the conduction and valence bands where there is a band degeneracy. For armchair SWNTs, this occurs at $q = \pm 2\pi/3a$. Figure 1.6 shows the calculated dispersion of a (11,0) semiconducting zigzag SWNT calculated from Equation (1.17). Since this is a semiconducting SWNT, there is a band gap at $q = 0$. In contrast, Figure 1.7 shows a metallic (12,0) zigzag SWNT. This zigzag tube is metallic because $n - m$ is a multiple of 3. At $q = 0$ there is a degeneracy between the conduction and valence band illustrating the metallic behavior.

For the case of chiral SWNTs, the dispersion is given, in general, by Equation (1.13). Chiral nanotubes can be classified into three categories depending on the greatest common divisor of $n - m$. The three classifications of SWNTs are summarized in Table 1.2. Metallic zigzag tubes always fall into the category of Metal-1 while all armchair tubes are Metal-2.

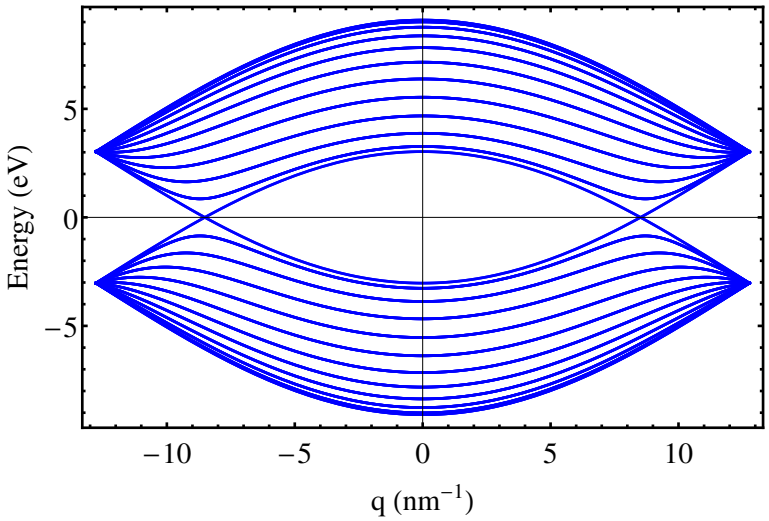

Figure 1.5: Calculated energy dispersion of a (11,11) armchair SWNT in the Brillouin zone from $-\pi/T$ to π/T.

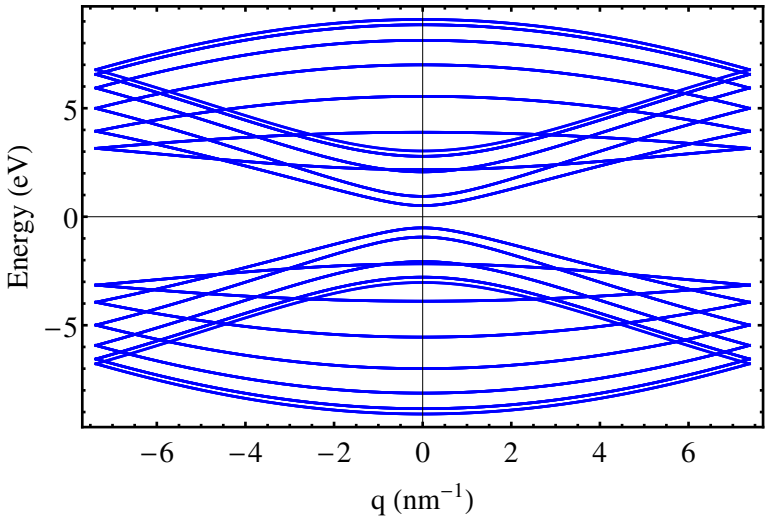

Figure 1.6: Calculated energy dispersion of a (11,0) semiconducting zigzag SWNT in the Brillouin zone from $-\pi/T$ to π/T.

Thus far, we have considered the single electron picture of SWNTs. However, their experimentally measured optical properties, such as absorption and photoluminescence (PL), show something different. Due to the quasi-1D nature of SWNTs, the

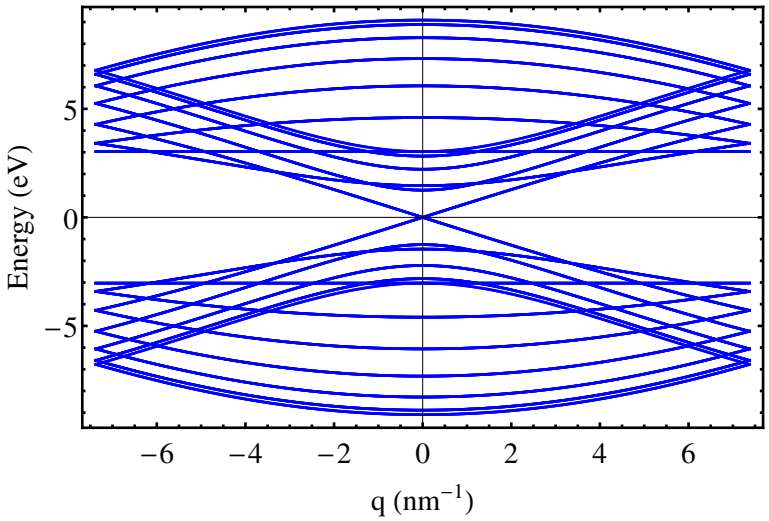

Figure 1.7: Calculated energy dispersion of a (12,0) metallic zigzag SWNT in the Brillouin zone from $-\pi/T$ to π/T.

Properties	gcd($n-m$,3)	d_R	Degeneracy
Semiconductor	1	d	0
Metal-1	3	d	4 at $k=0$
Metal-2	3	$3d$	2 at $k=\pm 2\pi/3T$

Table 1.2: Classifications of (n,m) SWNTs [1]. Here, d is the gcd(n,m).

SWNT has very strong quantum confinement and weak dielectric screening. Therefore, Coulomb effects are stronger in 1D SWNTs than in other materials. When an electron is promoted from the valence band to the conduction band, it leaves a hole in the valence band. This electron and hole are strongly coupled in the 1D structure via a Coulombic coupling. The correlated electron and hole pair become bound and act as a new quasi-particle known as an exciton. Excitons will be discussed further in Section 1.2.

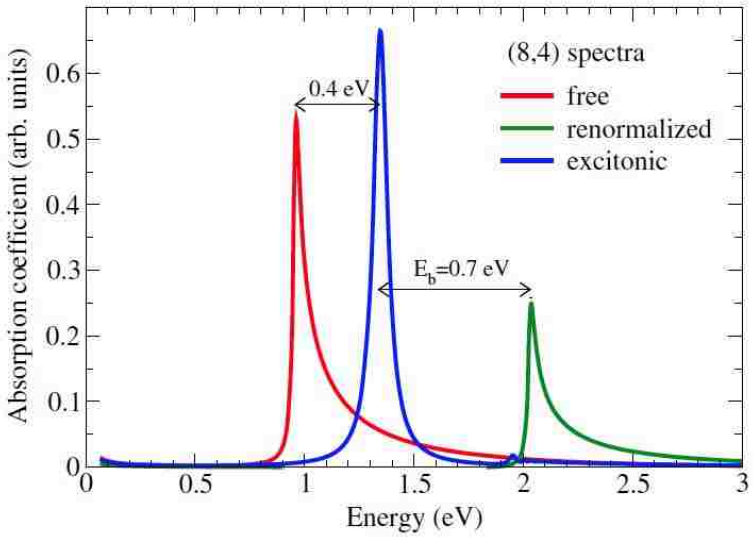

Figure 1.8: Absorption spectra of an (8,4) SWNT showing the first excitonic transition. The red line shows the free electron absorption ignoring Coulomb effects. The green line shows the band gap renormalization due to the electron-electron coupling (blue shift). The blue line shows the formation of an exciton by including electron-hole attraction (red shift and reshaped into a Lotentzian lineshape) [10].

1.2 Excitons

Excitonic effects dominate the optical spectra of SWNTs. The single particle picture of SWNTs is not sufficient to describe the experimentally observed absorption and PL. Figure 1.8 shows an example of how the Coulomb effects greatly affect the optical structure. The red line shows the absorption calculated without Coulomb effects. The absorption line resembles the Van Hove singularities of the 1D DOS. Including the electron-electron interaction renormalizes the band gap resulting in a blue shift of the absorption line and is shown by the green line. Including the electron-hole attractive Coulomb interaction red shifts the energy resulting in the excitonic absorption. Figure 1.9 shows a schematic diagram of the lowest excitonic band (red line) which is below the electron-hole continuum (black dashed line).

The exciton energy is red shifted from the electron-hole continuum as seen in

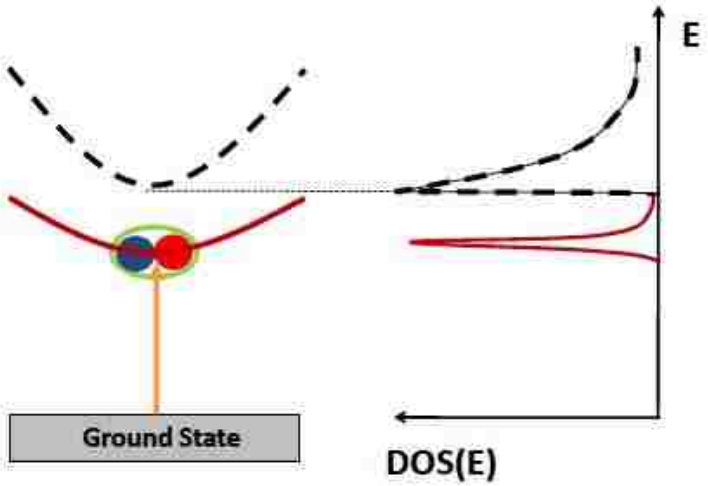

Figure 1.9: Schematic representation of the energy diagram (left) and DOS (right). The red line shows the lowest excitonic energy band (with correlated electron-hole pair) and the black dashed curve shows the electron-hole continuum [11].

Figures 1.8 and 1.9. The difference in energy between the exciton and the electron-hole continuum is called the binding energy, E_b. Because of the strong Coulomb interaction in the 1D structure, the binding energies of excitons in SWNTs are much larger than the binding energies in other semiconducting materials. The binding energy for a SWNT with a 1 nm diameter is approximately 0.5 - 1 eV [10, 35]. The binding energy is related to the size of the excitons. Exciton diameters have been calculated to be between 1 - 3 nm [36, 37].

In semiconducting SWNTs, there are multiple optically active singlet exciton energy levels to excite. The S_1 level, which is the lowest singlet level, is in the IR frequency range and the S_2 level is in the visible range for different chirality SWNTs. There are also higher levels such as the S_3 and S_4 levels which require UV excitation. Recently, the S_3 and S_4 levels of SWNTs were used in a study of DNA ionization, since DNA is excitable by UV light. The study was performed using two color spectroscopy of ssDNA functionalized SWNTs showing fast autoionization rates between the DNA and SWNT [38].

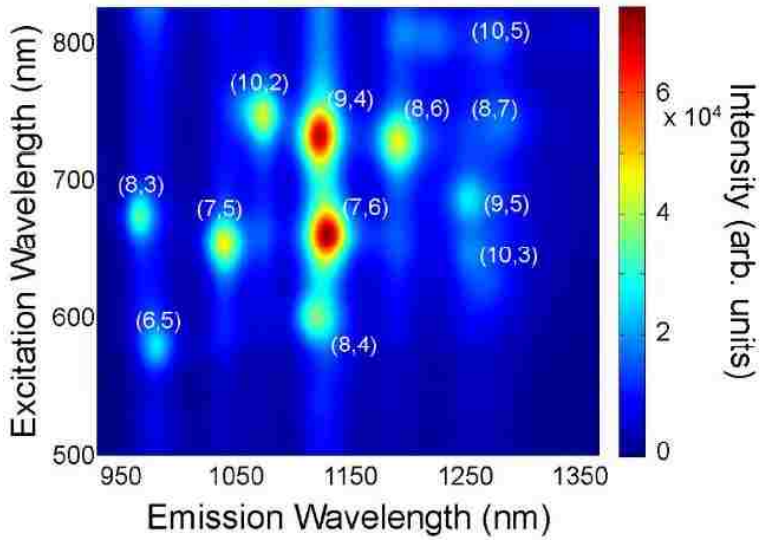

Figure 1.10: PLE map of a SWNT sample. Each chirality NT has a particular absorption and emission wavelength. Generating a PLE map will help determine which chirality SWNTs are in your sample [12].

When exciting a SWNT, we use visible light to promote the exciton from the ground state to the S_2 level. From there, the exciton undergoes fast non-radiative relaxation down to the S_1 level. There, it can either decay radiatively back to the ground state giving off a NIR photon, or decay non-radiatively back to the ground state depending on the experimental circumstances.

Exciton absoption and PL are most easily characterized by PL/PLE (photoluminescence/photoluminescence excitation) maps. Figure 1.10 shows an example of a PL/PLE map. The excitation wavelength is plotted on the y-axis and the emission wavelength is plotted on the x-axis. Each chirality SWNT has its own specific absorption and emission wavelength. By making a PL/PLE map, you can determine which chiralities of SWNTs are in your sample.

The theory of SWNT excitons will be discussed in more detail in Chapter 2.

1.3 Surface Plasmons

In nanophotonics and plasmonics, electromagnetic fields can be confined to dimensions on the order of or smaller than the wavelength [39]. Such an effect can follow from the interaction of electromagnetic radiation and free conduction electrons in metals or small nanostructures. This interaction leads to the creation of surface modes that generate an enhanced optical near field. One particular application of these confined electromagnetic fields is allowing better optical resolution of nano scale systems that visible wavelengths of light can not resolve. To begin to understand the basics of this field, we start with a simple description of metals.

We start with the classical Drude-Sommerfeld theory of a free electron gas:

$$m_e \frac{\partial^2 \mathbf{r}}{\partial t^2} + m_e \Gamma \frac{\partial \mathbf{r}}{\partial t} = e\mathbf{E}_0 e^{-i\omega t} \tag{1.18}$$

where e and m_e are the charge and effective mass of the free conduction electron, $\mathbf{E}_0$ and ω are the amplitude and frequency of the applied field, and Γ is a damping term proportional to v_F/l where v_F is the Fermi velocity and l is the mean free path between scattering events [13]. The displacement, $\mathbf{r}$, can be obtained from solving Equation 1.18. From there, we can define the polarization density $\mathbf{P}(\omega) = \epsilon_0 \chi_e(\omega)\mathbf{E}(\omega)$ with electric susceptibility, $\chi_e(\omega)$. The susceptibility can then be related to the dielectric function through $\varepsilon(\omega) = 1 + \chi_e(\omega)$. Solving Equation 1.18 with the ansatz $\mathbf{r}(t) = \mathbf{r}e^{-i\omega t}$, we arrive at the dielectric function

$$\varepsilon_{Drude}(\omega) = 1 - \frac{\omega_p^2}{\omega^2 + i\Gamma\omega} = 1 - \frac{\omega_p^2}{\omega^2 + \Gamma^2} + i\frac{\Gamma\omega_p^2}{\omega(\omega^2 + \Gamma^2)} \tag{1.19}$$

where $\omega_p = \sqrt{ne^2/(m_e\epsilon_0)}$ is the plasma frequency.

This definition works well for metals in the infrared region. However, in the visible range, we need to consider interband transitions. This is because photons at this higher energy can promote a valence electron into the conduction band. Therefore, we need to include the response of the bound electrons in the quasi-electrostatic and quasi-classical approximations by adding a restoring force:

$$m\frac{\partial^2 \mathbf{r}}{\partial t^2} + m\gamma\frac{\partial \mathbf{r}}{\partial t} + \alpha\mathbf{r} = e\mathbf{E}_0 e^{-i\omega t} \tag{1.20}$$

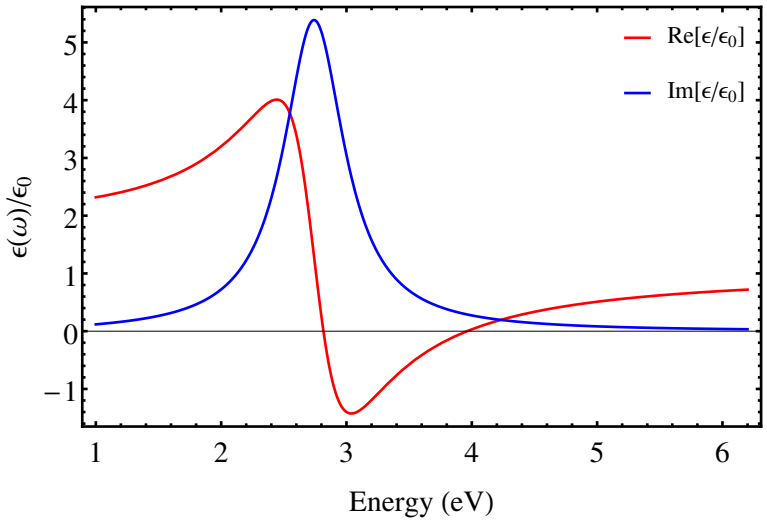

Figure 1.11: Contribution of bound electrons to the dielectric function of gold. The parameters used here are $\tilde{\omega}_p = 45 \times 10^{14}$ s^{-1}, $\gamma = 9 \times 10^{14}$ s^{-1}, and $\omega_0 = 2\pi c/\lambda$ with $\lambda = 450$ nm from [13].

where m is now the effective mass of the bound electron, γ is the damping constant (including radiative decay of the bound electron), and α is the effective "spring constant" of the potential that keeps the electron in place. Using the same ansatz, we can obtain the dielectric function

$$\varepsilon_{interband}(\omega) = 1 + \frac{\tilde{\omega}_p^2}{(\omega_0^2 - \omega^2) - i\gamma\omega} = 1 + \frac{\tilde{\omega}_p^2(\omega_0^2 - \omega^2)}{(\omega_0^2 - \omega^2)^2 + \gamma^2\omega^2} + i\frac{\gamma\tilde{\omega}_p^2\omega}{(\omega_0^2 - \omega^2)^2 + \gamma^2\omega^2} \tag{1.21}$$

where now $\omega_0 = \sqrt{\alpha/m}$ and $\tilde{\omega}_p = \sqrt{\tilde{n}e^2/(m\epsilon_0)}$ where $\tilde{n}$ is the density of bound electrons. Figure 1.11 shows an example of the bound electron contribution to the dielectric function of gold. Resonant behavior is seen in the imaginary part while dispersion behavior is seen in the real part. To more accurately model the behavior of metals over a larger frequency range, the interband contribution can be added to the Drude-Sommerfeld model.

Now, we seek to derive the surface plasmon-polariton dispersion. We begin with a classical model of two semi-infinite nonmagnetic media with local dielectric functions ϵ_1 and ϵ_2 separated by a planar interface at $z = 0$ [14]. Maxwell's equations

can be written for this system as (Gaussian units)

$$\nabla \times \mathbf{H}_i = \epsilon_i \frac{1}{c}\frac{\partial}{\partial t}\mathbf{E}_i \tag{1.22}$$

$$\nabla \times \mathbf{E}_i = -\frac{1}{c}\frac{\partial}{\partial t}\mathbf{H}_i \tag{1.23}$$

$$\nabla \cdot (\epsilon_i \mathbf{E}_i) = 0 \tag{1.24}$$

$$\nabla \cdot \mathbf{H}_i = 0 \tag{1.25}$$

where the index i represents the different media: $i = 1$ for $z < 0$ and $i = 2$ for $z > 0$. There are two classifications of solutions of Maxwell's equations: s-polarized and p-polarized electromagnetic modes where $\mathbf{E}$ and $\mathbf{H}$ are parallel to the interface, respectively. In order for waves to be formed that propagate along the surface, there must be a component of the electric field normal to the surface. Therefore, we seek p-polarized solutions where the magnetic field is parallel to the surface. If we choose the x-axis as the propagation direction, we can write the fields as

$$\mathbf{E}_i = (E_{ix}, 0, E_{iz})\, e^{-\kappa_i |z|} e^{i(q_i x - \omega t)} \tag{1.26}$$

and

$$\mathbf{H}_i = (0, H_{iy}, 0)\, e^{-\kappa_i |z|} e^{i(q_i x - \omega t)} \tag{1.27}$$

where q_i represents the magnitude of the wave vector that is parallel to the surface. Plugging these fields into Maxwell's equations gives

$$i\kappa_1 H_{1y} = \frac{\omega}{c}\epsilon_1 E_{1x} \tag{1.28}$$

$$i\kappa_2 H_{2y} = -\frac{\omega}{c}\epsilon_2 E_{2x} \tag{1.29}$$

and

$$\kappa_i = \sqrt{q_i^2 - \epsilon_i \frac{\omega^2}{c^2}} \tag{1.30}$$

Boundary conditions state that the component of the electric and magnetic fields parallel to the surface must be continuous. Applying this boundary condition, we get

$$\frac{\kappa_1}{\epsilon_1} H_{1y} + \frac{\kappa_2}{\epsilon_2} H_{2y} = 0 \tag{1.31}$$

$$H_{1y} - H_{2y} = 0 \tag{1.32}$$

which has a solution only if the determinant is zero. This gives

$$\frac{\epsilon_1}{\kappa_1} + \frac{\epsilon_2}{\kappa_2} = 0 \tag{1.33}$$

which is the surface plasmon condition. This equation can be rewritten in terms of q from Equation (1.30) as

$$q(\omega) = \frac{\omega}{c}\sqrt{\frac{\epsilon_1\epsilon_2}{\epsilon_1 + \epsilon_2}} \tag{1.34}$$

For the case of a Drude semi-infinite metal in vacuum, $\epsilon_2 = 1$ and the expression for the dielectric function ϵ_1 was given in Equation (1.19). Plugging this into Equation (1.34) gives

$$q(\omega) = \frac{\omega}{c}\sqrt{\frac{\omega^2 - \omega_p^2}{2\omega^2 - \omega_p^2}} \tag{1.35}$$

This dispersion can be seen in Figure 1.12. The upper dispersion line (solid) represents dispersion of light in the solid while the lower dispersion line (solid) is the surface plasmon polariton mode.

SWNTs can support surface plasmons. However, it is not only metallic SWNTs that exhibit surface plasmon resonances, but doped semiconducting SWNTs exhibit them as well. Figure 1.13 shows attenuation spectra ($-\log_{10} T$) for enriched samples of semiconducting and metallic SWNTs [15]. Their data shows a broad peak across the THz frequency range. One explanation for this THz peak was that it was caused by the van Hove singularity coming from a curvature induced band gap. On a flat sheet of graphene, the π-orbitals are orthogonal to the in-plane σ-orbitals. Because they are orthogonal, there are no overlaps between them and we can treat the π-orbitals by themselves in the TB approximation, as we did earlier in our derivation of the TB method for graphene. However, when the sheet of graphene is rolled into a SWNT, curvature effects become significant - especially for smaller diameter SWNTs. The curvature of the SWNT leads to a hybridization of the π- and σ-bonds and can alter the band structure of the SWNT. For the case of metallic SWNTs, as shown in Figure 1.5 for a metallic armchair SWNT and Figure 1.7 for a metallic zigzag SWNT, without curvature effects, there is no band gap because there exists a degeneracy between the conduction and valence bands. Including curvature effects

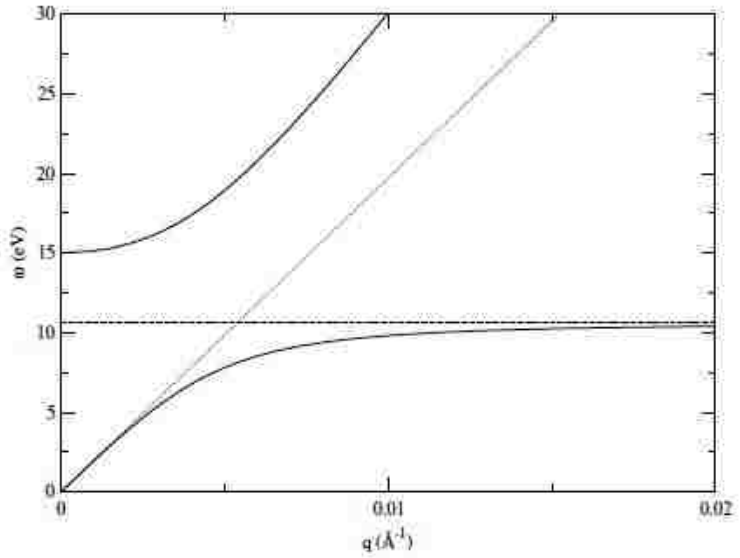

Figure 1.12: Plasmon dispersion (solid lines) with $\omega_p = 15$ eV. Dashed lines indicate the light line and the non-retarded surface plasmon frequency. The upper solid line is the dispersion of light in the solid while the lower dispersion line is the surface plasmon polariton mode [14].

can lead to a curvature induced band gap ranging from 1-100 meV in non-armchair SWNTs [40, 41].

The results of [15] conclude that the THz peaks are not caused by the curvature induced band gap [42, 43, 44, 45, 40, 46, 41], but instead by plasmon resonances, quantized due to the finite length of the SWNT [47, 48, 49, 50, 51]. The reason for seeing only a broad THz peak and not individual resonances is due to the variations of SWNT lengths in experimental samples. Since plasmon resonances form standing waves on the surface, they must obey the condition

$$\mathrm{Re}(k_p) = \frac{n\pi}{L} \tag{1.36}$$

where k_p is the plasmon wave vector, L is the length of the SWNT, and n is an integer. Plasmon resonances in SWNTs are heavily determined by the finite length of the SWNT [52, 51]. Therefore, even two SWNTs of the same chirality can have different plasmon resonances if their lengths are not equal. So even highly enriched

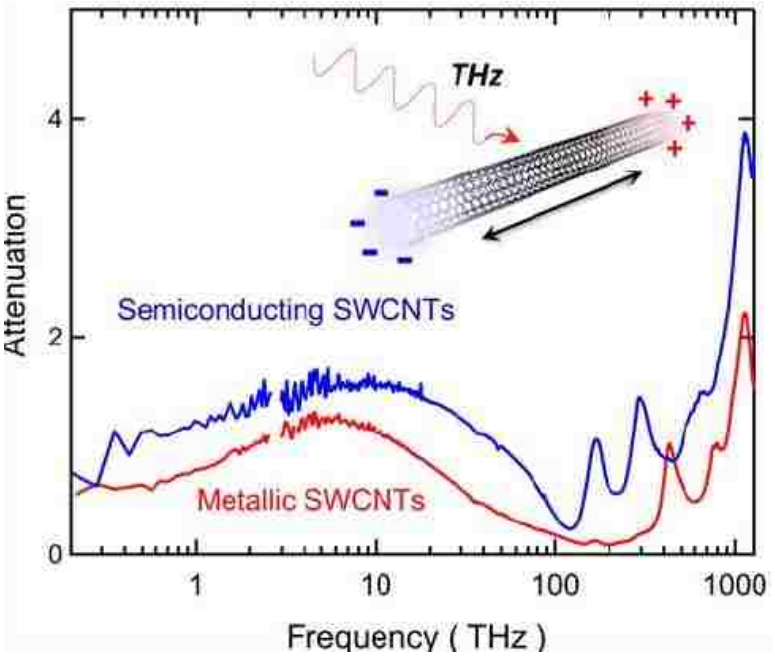

Figure 1.13: Attenuation spectra of both metallic and semiconducting SWNTs from THz to UV. A broad THz peak is observed in both samples indicating plasmon resonances [15].

samples like those in [15] will exhibit a broad THz peak rather than distinguishable resonances due to the length differences in the SWNTs.

1.3.1 Energy Transfer

Surface plasmon resonances can influence energy transfer rates to and from the SWNT in both the Förster resonance energy transfer (FRET) mechanism [53] as well as in the Dexter mechanism [54]. The FRET mechanism is a resonant dipole-dipole interaction between two objects. The rate of energy transfer in the FRET mechanism from a donor A to an acceptor B is given by [55]

$$W_{AB} = \frac{9\kappa^2 c^4}{8\pi\tau_A R^6} \int F_A(\omega)\sigma_B(\omega)\frac{d\omega}{\omega^4 n^4(\omega)} \tag{1.37}$$

where κ is an orientational factor describing the alignment of the dipole moments between A and B, τ_A is the radiative lifetime of the donor A, R is the distance

between donor and acceptor, $F_A(\omega)$ is the emission spectrum of the donor, $\sigma_B(\omega)$ is the absorption spectrum of the acceptor, and $n(\omega)$ is the refractive index of the medium. The integral over the spectral shapes calculates the amount of spectral overlap between the two systems. In order for FRET to occur, there must be a significant spectral overlap between the donor and acceptor, and the donor and acceptor must be in close proximity to each other given by the $1/R^6$ dependence on the distance between them. The $1/R^6$ dependence comes from the fluctuation interaction of two point dipoles. The fields of the dipoles drop off as $1/R^3$ and the interaction goes as the square of the fields giving the well known $1/R^6$ distance dependence.

The Dexter mechanism goes beyond the limitations of the Förster model. While the FRET mechanism is only valid for dipole-dipole (D-D) interactions, Dexter theory incorporates quadrupole (Q) interactions such as D-Q, Q-D, and Q-Q transitions. Whereas FRET is used to calculate the energy transfer between optically allowed states (transitions that have a nonzero dipole moment), Dexter theory can be used to calculate the energy transfer between states that may not be optically active (no transition dipole moment but they may have nonzero quadrupole moments).

Molecules near solid state particles with plasmon resonances were theoretically calculated to have accelerated rates of energy transfer if the molecule's transition frequency was in resonance with the plasmon frequency [56, 57, 58]. It was calculated that in the presence of a metallic nanoparticle with a plasmon resonance, the FRET transfer rate obtains an additional amplitude factor, $A(\omega)$, in the spectral overlap integral which gives the enhancement of the energy transfer rates [56]. This has also been measured experimentally with fluorophore molecules embedded in a silica shell around a core nanoparticle of gold or silver [59]. Also, the effect of nanoparticle concentration on the rate of energy transfer has been experimentally measured [60]. They were able to measure enhancement of energy transfer between quantum dots when mediated by gold nanoparticles. However, at higher concentrations of nanoparticles, they observed quenching of emission despite faster energy transfer rates due to a competition between the energy transfer and gold nanoparticle quenching effects [61].

1.4 Rare Earth Ions

Rare Earth Ions (REIs) are members of the lanthanide series on the periodic table. They are primarily trivalent, meaning they have a maximum +3 charge (Ln^{3+}). REIs have excellent photoluminescent properties [62, 63] and many useful applications including lighting and LEDs [62, 64, 65, 66, 67], solar cells [68, 69, 70, 71], temperature sensors [72], optical sensors [73], medical diagnostics and biological imaging [74, 75]. Terbium (Tb) and Europium (Eu) have also been used to perform confocal imaging of proteins [62, 76, 77]. Recently, REIs have been shown to form complexes with DNA functionalized SWNTs in solution [6]. Energy transfer between the systems was measured by observation of a shortening of the decay time of the REI. This provides evidence that SWNT/REI complexes have potential applications in the area of biosensing.

1.4.1 Judd-Ofelt Theory

In 1962, Brian Judd [78] and George Ofelt [79] independently published papers on the intensities of optical transitions in rare earth ions. At the time, neither knew of the other's work and the two papers were published in different journals within weeks of each other. Today, we refer to the theory of optical transitions in rare earth ions as Judd-Ofelt theory. The introduction of their theory was a breakthrough for rare earth spectroscopy in 1962 and continues to be a centerpiece of the work done in that field today.

To understand the basics of Judd-Ofelt theory, we begin with the free ion Hamiltonian [80],

$$H_F = -\frac{\hbar^2}{2m}\sum_{i=1}^{N}\nabla_i^2 - \sum_{i=1}^{N}\frac{Ze^2}{r_i} + \sum_{i<j}^{N}\frac{Ze^2}{r_{ij}} + \sum_{i=1}^{N}\xi(r_i)(\mathbf{s}_i\cdot\mathbf{l}_i) \tag{1.38}$$

The first term is the sum of the kinetic energies of the electrons of a $4f$ ion, the second term is the attractive Coulomb potential of all the electrons in the field of the nucleus, the third term is the repulsive Coulomb interaction between pairs of

electrons, and the final term is the spin-orbit interaction. In the central field approximation, each electron is considered to be moving independently in the field of the nucleus and a spherically averaged potential of all the other electrons. The Coulomb interaction produces different SL terms with different energies, but is independent of the total angular momentum J. The spin-orbit interaction allows for coupling between states of different SL and therefore depends on J. This means that the Coulomb interaction removes the degeneracy in S and L, and the spin-orbit interaction removes the degeneracy in J. The degeneracy in m_J remains and can only be lifted by a crystal field.

In the free ion, there is spherical symmetry and each level is then reduced to 2J+1 degeneracy. When the ion is placed into a crystal environment, the spherical symmetry is destroyed and each level splits due to the crystal field. The perturbed free ion Hamiltonian for an ion in a crystal or solution is

$$H = H_F + V_{CF} \tag{1.39}$$

where V_{CF} is the perturbation Hamiltonian produced by the crystal environment surrounding the ion. The eigenfunctions of the free ion Hamiltonian possess spherical symmetry and can be expressed in terms of spherical harmonics. Therefore V can be expanded in terms of spherical harmonics,

$$V_{CF} = \sum_{kq} A_{kq} \sum_i r_i^k Y_{kq}^*(\theta_i, \phi_i) \tag{1.40}$$

where the summation over i involves all electrons of the ion of interest. The A_{kq} are structural parameters in the static crystal field expansion. They depend on the crystal host and can be calculated in a point charge lattice sum using crystallographic data and charges of the host lattice. The point charge model assumes that the charges of the host lattice are all point charges. The A_{kq} are given by,

$$A_{kq} = -q_e \sum_i \frac{Z_i Y_{kq}(\theta_i, \phi_i)}{R_i^{k+1}} \tag{1.41}$$

where q_e is the electronic charge and Z_i is the size of the charge at position R_i corresponding to the surrounding atoms comprising the crystal.

The Judd-Ofelt theory is based on the static, free-ion, and single configuration approximations. In the static model, the central ion is affected by the surrounding host ions via a static electric field - the crystal field. In the free-ion model, the host environment provides the static crystal field and it is treated as a perturbation on the free-ion Hamiltonian. In the single configuration model, the interaction of electrons between configurations is neglected. The Judd-Ofelt theory describes the intensities of lanthanide transitions in solids and solutions. The utility of the theory is that it provides a theoretical expression for the linestrength, given by

$$S_{ED}(J;J') = \sum_{\lambda=2,4,6} \Omega_\lambda \left| \left\langle f^2[SL]J \left|\left| \mathbf{U}^{(\lambda)} \right|\right| f^n[S'L']J' \right\rangle \right|^2 \tag{1.42}$$

where the Ω_λ are the Judd-Ofelt parameters. The terms in the brackets are doubly reduced matrix elements for intermediate coupling. The intermediate coupling regime refers to the situation when the mutual Coulomb repulsion interaction between $4f$ electrons is of the same order of magnitude as the spin-orbit coupling. This is incorporated by expanding the wave functions of the $4f$ states in a linear combination of Russel-Saunders, or LS coupled states. The coupling coefficients are found by diagonalizing the combined electrostatic, spin-orbit, and configuration interaction energy matrices to obtain the full intermediate coupled wave functions $|f^n[SL]J\rangle$.

The matrix elements $\left| \left\langle f^2[SL]J \left|\left| \mathbf{U}^{(\lambda)} \right|\right| f^n[S'L']J' \right\rangle \right|^2$ are integrals of the dipole operator between the upper and lower wave functions of the transition, where integration takes place over the volume of the atom. The $\mathbf{U}^{(\lambda)}$ in Equation (1.42) are the irreducible tensor forms of the dipole operator. During the transition, the atom can be considered an electric dipole oscillating at some frequency whose amplitude is proportional to the value of this matrix element. It is the interaction of this dipole moment with the electric field of the electromagnetic wave that induces the transition.

In free ions, the electric dipole (ED) transitions within the $4f$ shell are forbidden. This is due to the fact that the total parity for an electron system is $\mathcal{P} = (-1)^{l_1+l_2+\ldots+l_n}$, where l is the angular quantum number. Regardless of the number of electrons, all states in the $4f$ shell always have a definite parity (either

+1 for an odd number of electrons or -1 for an even number). Since the dipole operator is odd under reflection, the ED transitions between $4f$ states are forbidden. However, these ED transitions can be forced if opposite parity states from higher lying configurations outside the $4f$ shell are mixed into the upper state. This is possible when the ion is placed in a noncentrosymmetric perturbing field such as in a crystal lattice or in solution. This can not happen in a central field because the Hamiltonian is invariant under coordinate inversion and the states will retain definite parity. The odd order parts of the crystal field, expanded in a series of spherical harmonics, perturb the system and produce mixed parity states in which dipole transitions are allowed. This is the starting point of the Judd-Ofelt theory.

From the theory, we can derive an expression for the oscillator strength

$$f = \frac{8\pi^2 mc}{3h\bar{\lambda}(2J+1)} n \left(\frac{n^2+2}{3n}\right)^2 \sum_{\lambda=2,4,6} \Omega_\lambda \left| \left\langle \varphi_a \left| \left| \mathbf{U}^{(\lambda)} \right| \right| \varphi_b \right\rangle \right|^2 \tag{1.43}$$

where m is the mass of the electron, c is the speed of light, h is the Planck constant, J is the total angular momentum quantum number, and n is the refractive index of the medium. The $(2J+1)$ term is a degeneracy factor and the term with the index of refraction, n, is part of the Onsager-Lorentz correction factor for the refractive index. The summation over λ is known as the linestrength, which was presented earlier in Equation (1.42).

Now, the transition probabilities $A(J;J')$ of all excited states can be calculated from

$$A(J;J') = \frac{64\pi^4 e^2}{3h(2J+1)\bar{\lambda}^3} \left[n \left(\frac{n^2+2}{3}\right)^2 S_{ED} + n^2 S_{MD} \right] \tag{1.44}$$

where n is the refractive index of the solid/solution, S_{ED} and S_{MD} are the electric and magnetic dipole linestrengths, and J' is the total angular momentum of the upper excited state. The ED linestrength is calculated from Equation (1.42). Table 1.3 show the selection rules that the electric dipole, magnetic dipole, and electric quadrupole transitions must satisfy.

Once the transition probabilities are known, we can then calculate the radiative

	S	L	J (no $0 \rightarrow 0$)	Parity
ED	$\Delta S = 0$	$\Delta L \leq 6$	$\Delta J \leq 6$	Opposite
			$\Delta J = 2, 4, 6$ (J or $J' = 0$)	
MD	$\Delta S = 0$	$\Delta L = 0$	$\Delta J = 0, \pm 1$	Same
EQ	$\Delta S = 0$	$\Delta L = 0, \pm 1, \pm 2$	$\Delta J = 0, \pm 1, \pm 2$	Same

Table 1.3: Selection rules for JO theory.

lifetime, τ_r, and the branching ratio, β

$$\frac{1}{\tau_r} = \sum_J A(J; J') \tag{1.45}$$

$$\beta_{JJ'} = \frac{A(J; J')}{\sum_J A(J; J')} \tag{1.46}$$

It is possible to calculate the Judd-Ofelt parameters, Ω_λ, ab-initio, but it requires accurate values of radial integrals and crystal field parameters which are not known to a high level of precision. Usually, the Judd-Ofelt parameters are treated as a set of phenomenological parameters to be determined from fitting experimental absorption measurements [2, 5, 81].

Carnall performed these ab-initio calculations of the energy levels of trivalent lanthanides [2]. He used an approximate model which included the effective interactions that reproduced the observed structure,

$$E = \sum_{k=0}^{6} F^k(nf, nf) f_k + \xi_{4f} A_{SO} + E_{CI} + E_{CF} \tag{1.47}$$

where the sum over k is for even values, f_k and A_{SO} represent the angular parts of the electrostatic and spin-orbit interactions respectively, the F^k are Slater integrals: $F^2 = 225F_2$, $F^4 = 1089F_4$, $F^6 = 184041/25F_6$ representing the purely electrostatic interaction between the $4f$ electrons, and ξ_{4f} is the spin-orbit coupling constant. E_{CI} represents the two-body and three-body effective operators to account for the

effects of configuration mixing, and E_{CF} is the crystal (or ligand) field interaction term.

The term E_{CI} in Equation (1.47) has included the effects of configuration interaction as expressed in the Trees correction $\alpha L(L+1)$, and the parameterized Casimir operators $\beta G(G_2)$ and $\gamma G(G_7)$. The additional terms represent those effects of configuration interaction that can be accounted for by two-body effective operators that do not transform as the f_k in Equation (1.47). For configurations of three or more equivalent f-electrons, the three particle operators of Judd [82], $T^i t_i$ $(i = 2, 3, 4, 6, 7, 8)$ where T^i are the parameters and t_i are the operators, have been included to account for the perturbing influence of those configurations that differ from f^N in the quantum numbers of a single electron. The effects represented by E_{CI} are not small and may shift the energies of individual terms by several hundred wavenumbers. The parameters used in Carnall's calculations are shown in Table 1.4. Table 1.5 shows the calculated radiative lifetimes of Eu and Tb. Table 1.6 shows how the intensities, energies, and lifetimes change when Tb and Eu are in H_2O compared to D_2O. Table 1.7 show calculated and experimentally measured energy level assignments for Tb in water.

	F^2	F^4	F^6	ξ_{4f}	α	β	γ
Eu^{3+}	83162	61245	41526	1326.0	25.336	-580.25	1155.7
Tb^{3+}	90358	66213	44262	1709.5	20.131	-370.21	1255.9

Table 1.4: Energy level parameter values calculated for the R^{3+} aquo ions in cm^{-1} [2].

Excited State	Eu $^5D_0$	Tb $^5D_4$
Energy of Excited State (cm^{-1})	17277	20500
$\tau_R(\psi J)$ (msec)	2.4	2.3

Table 1.5: Calculated radiative lifetimes of excited states of R^{3+} (aquo) [2].

	I_D/I_H [a]	ΔE [b] (cm^{-1})	τ_{H_2O} [c] (msec)	τ_{D_2O} [c] (msec)
Tb^{3+}	7.8 ± 0.8	14700	0.39 (0.48)[d]	3.3 (4.0)[d]
Eu^{3+}	18.0 ± 1.8	12300	0.10 (0.12)[d]	1.9 (4.0)[d]

Table 1.6: Fluorescence Intensities and Lifetimes of Lanthanide excited states in H_2O and D_2O [2].
[a]Solutions were 0.1M $R(NO_3)_3$ in H_2O or D_2O, and the intensity of fluorescence in D_2O was normalized to unity in H_2O in each case.
[b]ΔE is the difference in energy between the excited (resonance) level and the next lower energy level.
[c]The results are from [3] except as indicated.
[d]From [4]

S'L'J'	E_{expt} (cm^{-1})	E_{calc} (cm^{-1})	ΔE (cm^{-1})
$^7F_6$	85	74	11
$^7F_5$	2100	2112	-12
$^7F_4$	3356	3370	-14
$^7F_3$	4400	4344	56
$^7F_2$	5038	5028	10
$^7F_1$	5440	5481	-41
$^7F_0$	5700	5703	-3
$^5D_4$	20500	20545	-45
$^5D_3$	–	26336	–

Table 1.7: Energy level assignments for Tb^{3+} (aquo) [5].

Chapter 2

Excitons in SWNTs

In the previous chapter, we discussed the single-particle excitation of SWNTs. Then, we introduced excitons and how they dominate the optical spectra as well as some basic properties of SWNT excitons. In this chapter, we will go into more detail about what research has been conducted on SWNT excitons both experimentally and theoretically. Then, we derive for ourselves the Bethe-Salpeter equation for SWNT excitons.

2.1 Experimental Work

Schöppler, et al. used fluorescence tagging along with atomic force microscopy (AFM) measurements to measure the molar extinction coefficient of SWNTs which is directly related to the oscillator strength per carbon atom [37]. Malapanis, et al. used SWNTs as p-n diodes and performed photoconductivity measurements to extract the optical cross section and oscillator strengths of the E_{11} and E_{22} transitions of SWNTs [83]. Streit, et al. were able to directly count the number of SWNTs in a known sample volume using short-wave IR fluorescence microscopy [7]. They were able to very accurately measure the absorption cross sections per carbon atom for multiple chiralities of SWNTs. Wang, et al. were able to experimentally show the existence of excitons in metallic SWNTs [84]. They showed that the exciton binding energies of metallic SWNTs of approximately 50 meV exceeds

that of semiconducting SWNT excitons and agrees with ab initio theoretical predictions. Liu, et al. used a polarization based homodyne technique with broadband super-continuum excitation to measure absorption cross sections for over 50 different chirality SWNTs [85]. Dyatlova, et al. used PL/PLE spectroscopy to measure transition energies of SWNTs in solution as well as in vertical forests of SWNTs [86]. The purpose was to observe energy shifts of the transitions due to the different dielectric screening of the two environments. Lefebvre, et al. measured the photoluminescence of SWNTs suspended in air between pillars and encapsulated into solvent micelles [87]. They measured a 28 meV blueshift of emission peaks for the suspended SWNTs as compared to the encapsulated ones. They also measured a 16 meV blueshift of the absorption peaks at the second set of van Hove singularities. Liu, et al. performed a systematic study to establish a structure property 'atlas' of over 200 SWNT structures [88]. They used simultaneous electron diffraction measurements of the chiral indices and Rayleigh scattering measurements of the optical resonances. Fantini, et al. studied the Raman spectra of 46 different SWNTs in solid bundles or in aqueous solution [89]. They found the resonant window for SWNTs in bundles are broadened and red-shifted as compared to the SWNTs in solution. Also, the E_{22} energies were either red-shifted for S1 types ($(2n+m)\text{mod}3 = 1$) or blue-shifted for S2 types ($(2n+m)\text{mod}3 = 2$). Cambré, et al. studied the influence of water filling of SWNTs on their PL properties [90]. They measured a red-shift of PL when the SWNTs are filled with water molecules due to the change in the dielectric environment on the excitons. Recently in 2016, Mann and Hertel used femtosecond time-resolved pump-probe spectroscopy to determine the electron-hole correlation length, or exciton size, for (6,5) SWNTs [91]. They measured an exciton size of 13 ± 1 nm for vacuum suspended SWNTs which is roughly six times larger than previous measurements on the exciton size of (6,5) SWNTs [36, 37].

2.2 Theoretical Considerations

The theoretical treatment of excitons in SWNTs that is most relevant to our approach was that of Dresselhaus [1, 92, 93]. In this solid-state approach, the exciton wave function is expressed as a linear combination of single particle wave functions at many wave vectors k_c and k_v of the conduction and valence bands, respectively. The linear combination is needed because the exciton wave function is localized in real space by the Coulomb interaction, so the wave vector of the electron or the hole is no longer a good quantum number. The mixing of these wave vectors by the Coulomb interaction is calculated from the Bethe-Salpeter equation. Also in this method, the singular 1D Coulomb kernel is regularized by the phenomenological Ohno potential, which will be discussed in more detail later.

The methods of Reich and Knorr use the carbon nanotube Bloch equations to determine the excitonic absorption coefficient [10, 94, 95]. They derive the Bloch equation for the microscopic polarizability from the Heisenberg equation of motion where they can then calculate the absorption coefficient. They also use the regularized Ohno potential instead of the singular Coulomb kernel.

A different approach from that of Dresselhaus and Reich is that of Ando [96, 97, 98]. He uses the $\mathbf{k} \cdot \mathbf{p}$ method to derive the excitonic optical spectra. The $\mathbf{k} \cdot \mathbf{p}$ method is another solid state approximation method used to calculate the band structure of materials where the Hamiltonian can be separated into a perturbative term proportional to $\mathbf{k} \cdot \mathbf{p}$.

Goupalov derived analytical expressions for the optical matrix elements of interband transitions of SWNTs [99]. He also showed how to separate the Coulomb interaction into its short range and long range parts [100, 101]. He used the Fourier transform of the Coulomb potential, which gives Bessel functions, to show that only a finite number of terms contributes to the infinite sum. Therefore, the full Coulomb kernel can be used instead of using the regularized Ohno potential.

Miyauchi, et al. calculated the change in optical transition energy due to the change in the dielectric constant of the surrounding medium [102]. They solved the Bethe-Salpeter equation with the screened Ohno potential. Nugraha, et al.

also studied the dielectric screening effect on exciton energy levels and were able to present an analytical fit to their data [103]. Ando also studied the environmental screening effects using the $\mathbf{k}\cdot\mathbf{p}$ method [104]. He also studied the effects of screening on cross polarized excitons where the incident light is polarized perpendicularly to the tube axis [105]. He calculated that the intensity of the brightened dark exciton normalized by the bright exciton is strongly enhanced by the environmental screening.

Excitonic effects in metallic SWNTs were studied by Deslippe, et al. where they calculated excitonic bound states with binding energies of around 50 meV [106]. Kinder, et al. calculated that SWNTs have a uniform peak optical conductivity of 8 e^2/h independent of radius, chiral angle, or whether the SWNT is metallic or semiconducting [107].

2.3 Bethe-Salpeter Equation

Here, we derive the Bethe-Salpeter equation for SWNT excitons to obtain energy dispersions as well as exciton wave functions for any chirality SWNT.

2.3.1 Electron Hamiltonian

We begin by using the Hamiltonian of an electron subsystem in a solid which is defined as:

$$\hat{H} = \int \hat{\Psi}^\dagger(\mathbf{r}) H_0(\mathbf{r}) \hat{\Psi}(\mathbf{r}) d^3\mathbf{r} + \frac{1}{2}\int \hat{\Psi}^\dagger(\mathbf{r})\hat{\Psi}^\dagger(\mathbf{r}')V(\mathbf{r}-\mathbf{r}')\hat{\Psi}(\mathbf{r}')\hat{\Psi}(\mathbf{r}) d^3\mathbf{r} d^3\mathbf{r}' \quad (2.1)$$

where

$$\hat{H}_0(\mathbf{r}) = -\frac{\hbar^2\nabla^2}{2m} + U(\mathbf{r}) \quad (2.2)$$

is the Hamiltonian of an electron moving in the periodic potential of the crystalline lattice. Single electron energies and wavefunctions are defined by:

$$\hat{H}_0(\mathbf{r})\Phi_{\mathbf{k}j\sigma}(\mathbf{r}) = \varepsilon_j(\mathbf{k})\Phi_{\mathbf{k}j\sigma}(\mathbf{r}) \quad (2.3)$$

where $j = c, v$ and σ denotes the spin index. Wave functions include both spin and coordinate parts and can be separated as

$$\Phi_{\mathbf{k}j\sigma}(\mathbf{r}) = \phi_{\mathbf{k}j}(\mathbf{r})\chi_\sigma(s) \tag{2.4}$$

where the spin function $\chi_\sigma(s) = \delta_{\sigma s}$.

We can expand the the electron operators $\hat{\Psi}(\mathbf{r})$ and $\hat{\Psi}^\dagger(\mathbf{r})$ using the single electron wave functions (2.4) as a basis:

$$\hat{\Psi}(\mathbf{r}) = \sum_{\mathbf{k},j,\sigma} c_{\mathbf{k},j,\sigma}\Phi_{\mathbf{k}j\sigma}(\mathbf{r}), \quad \hat{\Psi}^\dagger(\mathbf{r}) = \sum_{\mathbf{k},j,\sigma} c^\dagger_{\mathbf{k},j,\sigma}\Phi^*_{\mathbf{k}j\sigma}(\mathbf{r}). \tag{2.5}$$

By substituting the electron operator expansions into the electron Hamiltonian in Equation (2.1) and rearranging terms for proper operator ordering, we obtain,

$$\begin{aligned} \hat{H} &= \sum_{\mathbf{k},j,\sigma} \varepsilon_j(\mathbf{k}) c^\dagger_{\mathbf{k},j,\sigma} c_{\mathbf{k},j,\sigma} \\ &+ \frac{1}{2} \sum_{\{\mathbf{k}j\}\sigma_1\sigma_2} c^\dagger_{\mathbf{k}_1,j_1,\sigma_1} c^\dagger_{\mathbf{k}_2,j_2,\sigma_2} c_{\mathbf{k}_3,j_3,\sigma_2} c_{\mathbf{k}_4,j_4,\sigma_1} \langle \mathbf{k}_1 j_1; \mathbf{k}_2 j_2 \left| V \right| \mathbf{k}_3 j_3; \mathbf{k}_4 j_4 \rangle \end{aligned} \tag{2.6}$$

where

$$\langle \mathbf{k}_1 j_1; \mathbf{k}_2 j_2 \left| V \right| \mathbf{k}_3 j_3; \mathbf{k}_4 j_4 \rangle = \int \phi^*_{\mathbf{k}_1 j_1}(\mathbf{r}) \phi^*_{\mathbf{k}_2 j_2}(\mathbf{r}') V(|\mathbf{r} - \mathbf{r}'|) \phi_{\mathbf{k}_3 j_3}(\mathbf{r}') \phi_{\mathbf{k}_4 j_4}(\mathbf{r}) d^3\mathbf{r} d^3\mathbf{r}'. \tag{2.7}$$

is the matrix element of the potential. This term will be expanded in more detail in the coming sections.

2.3.2 Redefining the Hamiltonian in terms of electrons and holes

Let us define the electron operators in the conduction band as

$$a_{\mathbf{k}\sigma} = c_{\mathbf{k}c\sigma} \qquad a^\dagger_{\mathbf{k}\sigma} = c^\dagger_{\mathbf{k}c\sigma}. \tag{2.8}$$

Instead of operators for electrons in the valence band, we introduce hole operators as follows:

$$d_{\mathbf{k}(-\sigma)} = c^\dagger_{\mathbf{k}v\sigma} \qquad d^\dagger_{\mathbf{k}(-\sigma)} = c_{\mathbf{k}v\sigma}. \tag{2.9}$$

Here, we have taken into account that the destruction of an electron with spin σ creates a hole with spin $-\sigma$.

Anti-commutation relations for these Fermionic operators can be summarized as follows:

$$\begin{aligned} \{a_\alpha, a_\beta\} = \{a^\dagger_\alpha, a^\dagger_\beta\} &= \{d_\alpha, d_\beta\} = \{d^\dagger_\alpha, d^\dagger_\beta\} = 0 \\ \{a_\alpha, a^\dagger_\beta\} &= \{d_\alpha, d^\dagger_\beta\} = \delta_{\alpha\beta} \\ \{a^\dagger_\alpha, d_\beta\} &= \{a_\alpha, d^\dagger_\beta\} = 0 \\ \{a_\alpha, d_\beta\} &= \{a^\dagger_\alpha, d^\dagger_\beta\} = \delta_{\alpha\beta} \end{aligned}$$

Kinetic Energy term of the Hamiltonian Here, we examine the first term of Equation (2.6) and express it in terms of the electron and hole operators

$$\hat{H}^{KE} = \sum_{\mathbf{k},j,\sigma} \varepsilon_j(\mathbf{k}) c^\dagger_{\mathbf{k},j,\sigma} c_{\mathbf{k},j,\sigma} = \sum_{\mathbf{k},\sigma} \varepsilon_C(\mathbf{k}) a^\dagger_{\mathbf{k},\sigma} a_{\mathbf{k},\sigma} - \sum_{\mathbf{k},\sigma} \varepsilon_V(\mathbf{k}) d^\dagger_{\mathbf{k},\sigma} d_{\mathbf{k},\sigma} + \sum_{\mathbf{k},\sigma} \varepsilon_V(\mathbf{k}) \tag{2.10}$$

The first term is the kinetic energy of the electron in the conduction band, the second term is the kinetic energy of the hole in the valence band, and the last term in the expression is the energy of the filled valence band.

Electron-Electron Interaction Now we turn our attention to the second term of the Hamiltonian in Equation (2.6). Taking into consideration that we have only one electron in the conduction band and one hole in the valence band, the only non-zero contributions to the interaction term

$$\hat{H}^{int} = \frac{1}{2} \sum_{\{\mathbf{k}j\}\sigma_1\sigma_2} c^\dagger_{\mathbf{k}_1,j_1,\sigma_1} c^\dagger_{\mathbf{k}_2,j_2,\sigma_2} c_{\mathbf{k}_3,j_3,\sigma_2} c_{\mathbf{k}_4,j_4,\sigma_1} \langle \mathbf{k}_1 j_1; \mathbf{k}_2 j_2 | V | \mathbf{k}_3 j_3; \mathbf{k}_4 j_4 \rangle ,$$

are the following combinations:

1. $j_1 = j_4 = C; j_2 = j_3 = V$
2. $j_1 = j_4 = V; j_2 = j_3 = C$
3. $j_1 = j_3 = C; j_2 = j_4 = V$

4. $j_1 = j_3 = V; j_2 = j_4 = C$

5. $j_1 = j_2 = j_3 = j_4 = V$.

We neglect the case where $j_1 = j_2 = j_3 = j_4 = C$ because that corresponds to the term $a^\dagger_{\mathbf{k}_1,\sigma_1} a^\dagger_{\mathbf{k}_2,\sigma_2} a_{\mathbf{k}_3,\sigma_2} a_{\mathbf{k}_4,\sigma_1}$ where there are two destruction operators standing to the right. When this term acts on the state containing one conduction electron, we get zero.

Now, let us rewrite the interaction terms by substituting the electron and hole operators and rearrange terms for proper ordering.

Electron-Electron Interaction 1: $j_1 = j_4 = C; j_2 = j_3 = V$

$$\begin{aligned}
\hat{H}^{(1)} &= \frac{1}{2} \sum_{\{\mathbf{k}\sigma\}} a^\dagger_{\mathbf{k}_1,\sigma_1} d_{\mathbf{k}_2,(-\sigma_2)} d^\dagger_{\mathbf{k}_3,(-\sigma_2)} a_{\mathbf{k}_4,\sigma_1} \langle \mathbf{k}_1 C; \mathbf{k}_2 V \,|V|\, \mathbf{k}_3 V; \mathbf{k}_4 C \rangle \\
&= \sum_{\mathbf{k}_1,\mathbf{k}_2,\mathbf{k}_4,\sigma_1} a^\dagger_{\mathbf{k}_1,\sigma_1} a_{\mathbf{k}_4,\sigma_1} \langle \mathbf{k}_1 C; \mathbf{k}_2 V \,|V|\, \mathbf{k}_2 V; \mathbf{k}_4 C \rangle \\
&\quad - \frac{1}{2} \sum_{\{\mathbf{k}\sigma\}} a^\dagger_{\mathbf{k}_1,\sigma_1} d^\dagger_{\mathbf{k}_3,(-\sigma_2)} d_{\mathbf{k}_2,(-\sigma_2)} a_{\mathbf{k}_4,\sigma_1} \langle \mathbf{k}_1 C; \mathbf{k}_2 V \,|V|\, \mathbf{k}_3 V; \mathbf{k}_4 C \rangle \quad (2.11)
\end{aligned}$$

Electron-Electron Interaction 2: $j_1 = j_4 = V; j_2 = j_3 = C$

$$\begin{aligned}
\hat{H}^{(2)} &= \frac{1}{2} \sum_{\{\mathbf{k}\sigma\}} d_{\mathbf{k}_1,(-\sigma_1)} a^\dagger_{\mathbf{k}_2,\sigma_2} a_{\mathbf{k}_3,\sigma_2} d^\dagger_{\mathbf{k}_4,(-\sigma_1)} \langle \mathbf{k}_1 V; \mathbf{k}_2 C \,|V|\, \mathbf{k}_3 C; \mathbf{k}_4 V \rangle \\
&= \sum_{\mathbf{k}_1,\mathbf{k}_2,\mathbf{k}_3,\sigma_2} a^\dagger_{\mathbf{k}_2,\sigma_2} a_{\mathbf{k}_3,\sigma_2} \langle \mathbf{k}_1 C; \mathbf{k}_2 V \,|V|\, \mathbf{k}_2 V; \mathbf{k}_1 C \rangle \\
&\quad - \frac{1}{2} \sum_{\{\mathbf{k}\sigma\}} a^\dagger_{\mathbf{k}_2,\sigma_2} d^\dagger_{\mathbf{k}_4,(-\sigma_1)} d_{\mathbf{k}_1,(-\sigma_1)} a_{\mathbf{k}_3,\sigma_2} \langle \mathbf{k}_1 V; \mathbf{k}_2 C \,|V|\, \mathbf{k}_3 C; \mathbf{k}_4 V \rangle \\
&= \hat{H}^{(1)} \quad (2.12)
\end{aligned}$$

Electron-Electron Interaction 3: $j_1 = j_3 = C; j_2 = j_4 = V$

$$\begin{aligned}
\hat{H}^{(3)} &= \frac{1}{2}\sum_{\{\mathbf{k}\sigma\}} a^\dagger_{\mathbf{k}_1,\sigma_1} d_{\mathbf{k}_2,(-\sigma_2)} a_{\mathbf{k}_3,\sigma_2} d^\dagger_{\mathbf{k}_4,(-\sigma_1)} \langle \mathbf{k}_1 C; \mathbf{k}_2 V \,|V|\, \mathbf{k}_3 C; \mathbf{k}_4 V\rangle \\
&= \frac{1}{2}\sum_{\mathbf{k}_1,\mathbf{k}_2,\mathbf{k}_3,\sigma_1} a^\dagger_{\mathbf{k}_1,\sigma_1} a_{\mathbf{k}_3,\sigma_1} \langle \mathbf{k}_1 C; \mathbf{k}_2 V \,|V|\, \mathbf{k}_3 C; \mathbf{k}_2 V\rangle \\
&\quad -\frac{1}{2}\sum_{\{\mathbf{k}\sigma\}} a^\dagger_{\mathbf{k}_1,\sigma_1} d^\dagger_{\mathbf{k}_4,(-\sigma_1)} d_{\mathbf{k}_2,(-\sigma_2)} a_{\mathbf{k}_3,\sigma_2} \langle \mathbf{k}_1 C; \mathbf{k}_2 V \,|V|\, \mathbf{k}_3 C; \mathbf{k}_4 V\rangle \quad (2.13)
\end{aligned}$$

Electron-Electron Interaction 4: $j_1 = j_3 = V; j_2 = j_4 = C$

$$\begin{aligned}
\hat{H}^{(4)} &= \frac{1}{2}\sum_{\{\mathbf{k}\sigma\}} d_{\mathbf{k}_1,(-\sigma_1)} a^\dagger_{\mathbf{k}_2,\sigma_2} d^\dagger_{\mathbf{k}_3,(-\sigma_2)} a_{\mathbf{k}_4,\sigma_1} \langle \mathbf{k}_1 V; \mathbf{k}_2 C \,|V|\, \mathbf{k}_3 V; \mathbf{k}_4 C\rangle \\
&= \frac{1}{2}\sum_{\mathbf{k}_1,\mathbf{k}_2,\mathbf{k}_4,\sigma_1} a^\dagger_{\mathbf{k}_2,\sigma_1} a_{\mathbf{k}_4,\sigma_1} \langle \mathbf{k}_1 V; \mathbf{k}_2 C \,|V|\, \mathbf{k}_1 V; \mathbf{k}_4 C\rangle \\
&\quad -\frac{1}{2}\sum_{\{\mathbf{k}\sigma\}} a^\dagger_{\mathbf{k}_2,\sigma_2} d^\dagger_{\mathbf{k}_3,(-\sigma_2)} d_{\mathbf{k}_1,(-\sigma_1)} a_{\mathbf{k}_4,\sigma_1} \langle \mathbf{k}_1 V; \mathbf{k}_2 C \,|V|\, \mathbf{k}_3 V; \mathbf{k}_4 C\rangle \\
&= \hat{H}^{(3)} \quad (2.14)
\end{aligned}$$

Electron-Electron Interaction 5: $j_1 = j_2 = j_3 = j_4 = V$

$$\begin{aligned}
\hat{H}^{(5)} &= \frac{1}{2}\sum_{\{\mathbf{k}\sigma\}} d_{\mathbf{k}_1,(-\sigma_1)} d_{\mathbf{k}_2,(-\sigma_2)} d^\dagger_{\mathbf{k}_3,(-\sigma_2)} d^\dagger_{\mathbf{k}_4,(-\sigma_1)} \langle \mathbf{k}_1 V; \mathbf{k}_2 V \,|V|\, \mathbf{k}_3 V; \mathbf{k}_4 V\rangle \\
&= -2\sum_{\mathbf{k}_1,\mathbf{k}_2,\mathbf{k}_3,\sigma_1} d^\dagger_{\mathbf{k}_3,(-\sigma_1)} d_{\mathbf{k}_1,(-\sigma_1)} \langle \mathbf{k}_1 V; \mathbf{k}_2 V \,|V|\, \mathbf{k}_2 V; \mathbf{k}_3 V\rangle \\
&\quad + \sum_{\mathbf{k}_1,\mathbf{k}_2,\mathbf{k}_3,\sigma_1} d^\dagger_{\mathbf{k}_3,(-\sigma_1)} d_{\mathbf{k}_1,(-\sigma_1)} \langle \mathbf{k}_1 V; \mathbf{k}_2 V \,|V|\, \mathbf{k}_3 V; \mathbf{k}_2 V\rangle \quad (2.15)
\end{aligned}$$

Here, we neglected constant terms and terms containing two destruction operators to the right.

Total Hamiltonian: Combining the kinetic energy and interaction terms gives us the final Hamiltonian of Equation (2.6) written in terms of the electron and hole

operators:

$$
\begin{aligned}
\hat{H} &= \sum_{\mathbf{k},\sigma} \varepsilon_C(\mathbf{k}) a^\dagger_{\mathbf{k},\sigma} a_{\mathbf{k},\sigma} - \sum_{\mathbf{k},\sigma} \varepsilon_V(\mathbf{k}) d^\dagger_{\mathbf{k},\sigma} d_{\mathbf{k},\sigma} + \sum_{\mathbf{k},\sigma} \varepsilon_V(\mathbf{k}) \\
&+ \sum_{\mathbf{k}_1,\mathbf{k}_2,\mathbf{k}_3,\sigma_1} a^\dagger_{\mathbf{k}_3\sigma_1} a_{\mathbf{k}_1\sigma_1} \left[2 \left\langle \mathbf{k}_1 C; \mathbf{k}_2 V \left| V \right| \mathbf{k}_2 V; \mathbf{k}_3 C \right\rangle - \left\langle \mathbf{k}_1 C; \mathbf{k}_2 V \left| V \right| \mathbf{k}_3 C; \mathbf{k}_2 V \right\rangle\right] \\
&- \sum_{\mathbf{k}_1,\mathbf{k}_2,\mathbf{k}_3,\sigma_1} d^\dagger_{\mathbf{k}_3(-\sigma_1)} d_{\mathbf{k}_1(-\sigma_1)} \\
&\quad \times \left[2 \left\langle \mathbf{k}_1 V; \mathbf{k}_2 V \left| V \right| \mathbf{k}_2 V; \mathbf{k}_3 V \right\rangle - \left\langle \mathbf{k}_1 V; \mathbf{k}_2 V \left| V \right| \mathbf{k}_3 V; \mathbf{k}_2 V \right\rangle\right] \\
&+ \sum_{\{\mathbf{k},\sigma\}} a^\dagger_{\mathbf{k}_1,\sigma_1} d^\dagger_{\mathbf{k}_4(-\sigma_1)} d_{\mathbf{k}_2,(-\sigma_2)} a_{\mathbf{k}_3,\sigma_2} \left\langle \mathbf{k}_1 C; \mathbf{k}_2 V \left| V \right| \mathbf{k}_3 C; \mathbf{k}_4 V \right\rangle \\
&- \sum_{\{\mathbf{k},\sigma\}} a^\dagger_{\mathbf{k}_1,\sigma_1} d^\dagger_{\mathbf{k}_3(-\sigma_2)} d_{\mathbf{k}_2,(-\sigma_2)} a_{\mathbf{k}_4,\sigma_1} \left\langle \mathbf{k}_1 C; \mathbf{k}_2 V \left| V \right| \mathbf{k}_3 V; \mathbf{k}_4 C \right\rangle
\end{aligned} \tag{2.16}
$$

2.3.3 Singlet and Triplet Wavefunctions

By taking the total spin $\sigma = \sigma_1 + \sigma_2$, we can separate the singlet wave function operator (total spin = 0)

$$
\Psi_s = \sum_{\mathbf{k}_e,\mathbf{k}_h} C_{\mathbf{k}_e,\mathbf{k}_h} \left(a^\dagger_{\mathbf{k}_e\uparrow} d^\dagger_{\mathbf{k}_h\downarrow} + a^\dagger_{\mathbf{k}_e\downarrow} d^\dagger_{\mathbf{k}_h\uparrow} \right) \tag{2.17}
$$

and the three triplet wavefunction operators (total spin =$\pm$1)

$$
\Psi_T = \begin{cases} \displaystyle\sum_{\mathbf{k}_e,\mathbf{k}_h} A_{\mathbf{k}_e,\mathbf{k}_h} a^\dagger_{\mathbf{k}_e\uparrow} d^\dagger_{\mathbf{k}_h\uparrow} \\ \displaystyle\sum_{\mathbf{k}_e,\mathbf{k}_h} B_{\mathbf{k}_e,\mathbf{k}_h} \left(a^\dagger_{\mathbf{k}_e\uparrow} d^\dagger_{\mathbf{k}_h\downarrow} - a^\dagger_{\mathbf{k}_e\downarrow} d^\dagger_{\mathbf{k}_h\uparrow} \right) \\ \displaystyle\sum_{\mathbf{k}_e,\mathbf{k}_h} D_{\mathbf{k}_e,\mathbf{k}_h} a^\dagger_{\mathbf{k}_e\downarrow} d^\dagger_{\mathbf{k}_h\downarrow} \end{cases} \tag{2.18}
$$

In order to obtain the Bethe-Salpeter equation, we need to act the total Hamiltonian in Equation (2.16) on the exciton wavefunction. First, the total Hamiltonian

(2.16) will be rewritten in a more condensed manner.

$$\begin{aligned}\hat{H} &= \sum_{\mathbf{k},\sigma} E_C(\mathbf{k}) a^\dagger_{\mathbf{k},\sigma} a_{\mathbf{k},\sigma} - \sum_{\mathbf{k},\sigma} E_V(\mathbf{k}) d^\dagger_{\mathbf{k},\sigma} d_{\mathbf{k},\sigma} \\ &+ \sum_{\{\mathbf{k},\sigma\}} a^\dagger_{\mathbf{k}_1,\sigma_1} d^\dagger_{\mathbf{k}_4(-\sigma_1)} d_{\mathbf{k}_2,(-\sigma_2)} a_{\mathbf{k}_3,\sigma_2} \langle \mathbf{k}_1 C; \mathbf{k}_2 V \,|V|\, \mathbf{k}_3 C; \mathbf{k}_4 V \rangle \\ &- \sum_{\{\mathbf{k},\sigma\}} a^\dagger_{\mathbf{k}_1,\sigma_1} d^\dagger_{\mathbf{k}_3(-\sigma_2)} d_{\mathbf{k}_2,(-\sigma_2)} a_{\mathbf{k}_4,\sigma_1} \langle \mathbf{k}_1 C; \mathbf{k}_2 V \,|V|\, \mathbf{k}_3 V; \mathbf{k}_4 C \rangle \end{aligned} \tag{2.19}$$

where we have combined terms with $a^\dagger a$ and $d^\dagger d$, and

$$E_C(\mathbf{k}) = \varepsilon_C(\mathbf{k}) + \sum_{\mathbf{k}_1,\mathbf{k}_2,\mathbf{k}_3,\sigma_1} [2 \langle \mathbf{k}_1 C; \mathbf{k}_2 V \,|V|\, \mathbf{k}_2 V; \mathbf{k}_3 C \rangle - \langle \mathbf{k}_1 C; \mathbf{k}_2 V \,|V|\, \mathbf{k}_3 C; \mathbf{k}_2 V \rangle] \tag{2.20}$$

$$E_V(\mathbf{k}) = -\varepsilon_V(\mathbf{k}) - \sum_{\mathbf{k}_1,\mathbf{k}_2,\mathbf{k}_3,\sigma_1} [2 \langle \mathbf{k}_1 V; \mathbf{k}_2 V \,|V|\, \mathbf{k}_2 V; \mathbf{k}_3 V \rangle - \langle \mathbf{k}_1 V; \mathbf{k}_2 V \,|V|\, \mathbf{k}_3 V; \mathbf{k}_2 V \rangle] \tag{2.21}$$

are the self-energies of the electron and the hole. The electron self-energy is the interaction of an electron in the conduction band with the full valence band. The hole self-energy is the interaction of the hole with the valence band. The self-energy terms renormalize the the single particle energies $\varepsilon_C(\mathbf{k})$ and $\varepsilon_V(\mathbf{k})$.

2.3.4 Singlet Bethe-Salpeter Equation

Acting the Hamiltonian in Equation (2.19) onto the singlet wave function in Equation (2.17), we obtain the singlet Bethe-Salpeter Equation:

$$\begin{aligned}&(E_C(\mathbf{k}_e) + E_V(\mathbf{k}_h)) C_{\mathbf{k}_e,\mathbf{k}_h} + \sum_{\mathbf{k},\mathbf{k}'} C_{\mathbf{k}'_e,\mathbf{k}'_h} [2 \langle \mathbf{k}_e, \mathbf{k}'_h \,|V|\, \mathbf{k}'_e, \mathbf{k}_h \rangle - \langle \mathbf{k}_e, \mathbf{k}'_h \,|V|\, \mathbf{k}_h, \mathbf{k}'_e \rangle] \\ &= \Omega C_{\mathbf{k}_e,\mathbf{k}_h} \end{aligned} \tag{2.22}$$

where $E_C(\mathbf{k}_e)$ is the electron energy term, $E_V(\mathbf{k}_h)$ is the hole energy term, and we have broken up the coulomb integral into two parts: the exchange term (first term in square brackets) and the direct term (second expression in square brackets). The direct term describes the scattering of an electron by a hole. The exchange

interaction describes the interaction of an electron in the conduction band with a hole in the valence band.

To show how we got to Equation (2.22), here were the steps taken. The electron energy term was calculated by

$$\begin{aligned}
&\sum_{\mathbf{k}\sigma} E_C(\mathbf{k}) a^\dagger_{\mathbf{k}\sigma} a_{\mathbf{k}\sigma} \sum_{\mathbf{k}_e,\mathbf{k}_h} C_{\mathbf{k}_e,\mathbf{k}_h} \left(a^\dagger_{\mathbf{k}_e\uparrow} d^\dagger_{\mathbf{k}_h\downarrow} + a^\dagger_{\mathbf{k}_e\downarrow} d^\dagger_{\mathbf{k}_h\uparrow} \right) \\
&= \sum_{\mathbf{k}_e,\mathbf{k}_h} C_{\mathbf{k}_e,\mathbf{k}_h} \sum_{\mathbf{k}\sigma} E_C(\mathbf{k}) a^\dagger_{\mathbf{k}\sigma} \delta_{\mathbf{k}_e,\mathbf{k}} \left(\delta_{\sigma\uparrow} d^\dagger_{\mathbf{k}_h\downarrow} + \delta_{\sigma\downarrow} d^\dagger_{\mathbf{k}_h\uparrow} \right) \\
&= \sum_{\mathbf{k}_e,\mathbf{k}_h} C_{\mathbf{k}_e,\mathbf{k}_h} E_C(\mathbf{k}_e) \left(a^\dagger_{\mathbf{k}_e\uparrow} d^\dagger_{\mathbf{k}_h\downarrow} + a^\dagger_{\mathbf{k}_e\downarrow} d^\dagger_{\mathbf{k}_h\uparrow} \right).
\end{aligned}$$

The hole energy term was calculated by

$$\begin{aligned}
&\sum_{\mathbf{k}\sigma} E_V(\mathbf{k}) d^\dagger_{\mathbf{k}(-\sigma)} d_{\mathbf{k}(-\sigma)} \sum_{\mathbf{k}_e,\mathbf{k}_h} C_{\mathbf{k}_e,\mathbf{k}_h} \left(a^\dagger_{\mathbf{k}_e\uparrow} d^\dagger_{\mathbf{k}_h\downarrow} + a^\dagger_{\mathbf{k}_e\downarrow} d^\dagger_{\mathbf{k}_h\uparrow} \right) \\
&= \sum_{\mathbf{k}_e,\mathbf{k}_h} C_{\mathbf{k}_e,\mathbf{k}_h} \sum_{\mathbf{k}\sigma} E_V(\mathbf{k}) d^\dagger_{\mathbf{k}(-\sigma)} \delta_{\mathbf{k}_h,\mathbf{k}} \left(-\delta_{(-\sigma)\downarrow} a^\dagger_{\mathbf{k}_e\uparrow} - \delta_{(-\sigma)\uparrow} a^\dagger_{\mathbf{k}_e\downarrow} \right) \\
&= \sum_{\mathbf{k}_e,\mathbf{k}_h} C_{\mathbf{k}_e,\mathbf{k}_h} E_V(\mathbf{k}_h) \left(a^\dagger_{\mathbf{k}_e\uparrow} d^\dagger_{\mathbf{k}_h\downarrow} + a^\dagger_{\mathbf{k}_e\downarrow} d^\dagger_{\mathbf{k}_h\uparrow} \right).
\end{aligned}$$

The direct interaction was calculated by

$$\begin{aligned}
&\sum_{\{\mathbf{k},\sigma\}} a^\dagger_{\mathbf{k}_1,\sigma_1} d^\dagger_{\mathbf{k}_3(-\sigma_2)} d_{\mathbf{k}_2,(-\sigma_2)} a_{\mathbf{k}_4,\sigma_1} \langle \mathbf{k}_1 C; \mathbf{k}_2 V \,|V|\, \mathbf{k}_3 V; \mathbf{k}_4 C \rangle \\
&\quad \times \sum_{\mathbf{k}_e,\mathbf{k}_h} C_{\mathbf{k}_e,\mathbf{k}_h} \left(a^\dagger_{\mathbf{k}_e\uparrow} d^\dagger_{\mathbf{k}_h\downarrow} + a^\dagger_{\mathbf{k}_e\downarrow} d^\dagger_{\mathbf{k}_h\uparrow} \right) \\
&= \sum_{\mathbf{k}_e,\mathbf{k}_h} C_{\mathbf{k}_e,\mathbf{k}_h} \sum_{\{\mathbf{k},\sigma\}} \delta_{\mathbf{k}_4,\mathbf{k}_e} \delta_{\mathbf{k}_2,\mathbf{k}_h} a^\dagger_{\mathbf{k}_1,\sigma_1} d^\dagger_{\mathbf{k}_3(-\sigma_2)} \left(\delta_{\sigma_1,\uparrow} \delta_{-\sigma_2,\downarrow} + \delta_{\sigma_1,\downarrow} \delta_{-\sigma_2,\uparrow} \right) \\
&\quad \times \langle \mathbf{k}_1 C; \mathbf{k}_2 V \,|V|\, \mathbf{k}_3 V; \mathbf{k}_4 C \rangle \\
&= \sum_{\mathbf{k}_e,\mathbf{k}_h} C_{\mathbf{k}_e,\mathbf{k}_h} \sum_{\mathbf{k}_1,\mathbf{k}_3} \left(a^\dagger_{\mathbf{k}_1\uparrow} d^\dagger_{\mathbf{k}_3\downarrow} + a^\dagger_{\mathbf{k}_1\downarrow} d^\dagger_{\mathbf{k}_3\uparrow} \right) \langle \mathbf{k}_1 C; \mathbf{k}_h V \,|V|\, \mathbf{k}_3 V; \mathbf{k}_e C \rangle \\
&= \sum_{\mathbf{k}'_e,\mathbf{k}'_h} C_{\mathbf{k}'_e,\mathbf{k}'_h} \left(a^\dagger_{\mathbf{k}_e\uparrow} d^\dagger_{\mathbf{k}_h\downarrow} + a^\dagger_{\mathbf{k}_e\downarrow} d^\dagger_{\mathbf{k}_h\uparrow} \right) \langle \mathbf{k}_e; \mathbf{k}'_h \,|V|\, \mathbf{k}_h; \mathbf{k}'_e \rangle .
\end{aligned}$$

The exchange interaction was calculated by

$$
\begin{aligned}
&\sum_{\{\mathbf{k},\sigma\}} a^{\dagger}_{\mathbf{k}_1,\sigma_1} d^{\dagger}_{\mathbf{k}_4(-\sigma_1)} d_{\mathbf{k}_2,(-\sigma_2)} a_{\mathbf{k}_3,\sigma_2} \left\langle \mathbf{k}_1 C; \mathbf{k}_2 V \left| V \right| \mathbf{k}_3 C; \mathbf{k}_4 V \right\rangle \\
&\quad \times \sum_{\mathbf{k}_e,\mathbf{k}_h} C_{\mathbf{k}_e,\mathbf{k}_h} \left(a^{\dagger}_{\mathbf{k}_e\uparrow} d^{\dagger}_{\mathbf{k}_h\downarrow} + a^{\dagger}_{\mathbf{k}_e\downarrow} d^{\dagger}_{\mathbf{k}_h\uparrow} \right) \\
&= \sum_{\mathbf{k}_e,\mathbf{k}_h} C_{\mathbf{k}_e,\mathbf{k}_h} \sum_{\{\mathbf{k},\sigma\}} \delta_{\mathbf{k}_3,\mathbf{k}_e} \delta_{\mathbf{k}_2,\mathbf{k}_h} a^{\dagger}_{\mathbf{k}_1,\sigma_1} d^{\dagger}_{\mathbf{k}_4(-\sigma_1)} \left(\delta_{\sigma_2,\uparrow} \delta_{-\sigma_2,\downarrow} + \delta_{\sigma_2,\downarrow} \delta_{-\sigma_2,\uparrow} \right) \\
&\quad \times \left\langle \mathbf{k}_1 C; \mathbf{k}_2 V \left| V \right| \mathbf{k}_3 C; \mathbf{k}_4 V \right\rangle \\
&= 2 \sum_{\mathbf{k}_e,\mathbf{k}_h} C_{\mathbf{k}_e,\mathbf{k}_h} \sum_{\mathbf{k}_1,\mathbf{k}_4,\sigma_1} a^{\dagger}_{\mathbf{k}_1,\sigma_1} d^{\dagger}_{\mathbf{k}_4(-\sigma_1)} \left\langle \mathbf{k}_1 C; \mathbf{k}_h V \left| V \right| \mathbf{k}_e C; \mathbf{k}_4 V \right\rangle \\
&= 2 \sum_{\mathbf{k}_e,\mathbf{k}_h} C_{\mathbf{k}_e,\mathbf{k}_h} \sum_{\mathbf{k}_1,\mathbf{k}_4} \left(a^{\dagger}_{\mathbf{k}_1\uparrow} d^{\dagger}_{\mathbf{k}_4\downarrow} + a^{\dagger}_{\mathbf{k}_1\downarrow} d^{\dagger}_{\mathbf{k}_4\uparrow} \right) \left\langle \mathbf{k}_1 C; \mathbf{k}_h V \left| V \right| \mathbf{k}_e C; \mathbf{k}_4 V \right\rangle \\
&= 2 \sum_{\mathbf{k}'_e,\mathbf{k}'_h} C_{\mathbf{k}'_e,\mathbf{k}'_h} \left(a^{\dagger}_{\mathbf{k}_e\uparrow} d^{\dagger}_{\mathbf{k}_h\downarrow} + a^{\dagger}_{\mathbf{k}_e\downarrow} d^{\dagger}_{\mathbf{k}_h\uparrow} \right) \left\langle \mathbf{k}_e; \mathbf{k}'_h \left| V \right| \mathbf{k}'_e; \mathbf{k}_h \right\rangle .
\end{aligned}
$$

2.3.5 Matrix Elements of Bethe-Salpeter Equation

Here we use a simplified exciton wave function where we suppress the spin indices and express the total singlet wave function as a linear combination of single particle tight-binding wave functions

$$\Psi(\mathbf{r}_e, \mathbf{r}_h) = \sum_{\mu_e,\mu_h,q_e,q_h} C(\mu_e, \mu_h; q_e, q_h) \psi_{\mu_e,q_e}(\mathbf{r}_e) \psi^{*}_{\mu_h,q_h}(\mathbf{r}_h) \tag{2.23}$$

where $C(\mu_e, \mu_h; q_e, q_h)$ are the wave function amplitudes to be determined. This wave function comes from defining the exciton creation operator

$$B^{\dagger} = \sum_{\mu_e,\mu_h,q_e,q_h} C(\mu_e, \mu_h; q_e, q_h) a^{\dagger}_{\mu_e,q_e} d^{\dagger}_{\mu_h,q_h} \tag{2.24}$$

The wave function can then be derived from

$$\Psi(\mathbf{r}_e, \mathbf{r}_h) = \left\langle \mathbf{r}_e, \mathbf{r}_h \left| B^{\dagger} \right| 0 \right\rangle \tag{2.25}$$

where $|0\rangle$ is the excitonic ground state, i.e. the state where no excitons are present.

Direct Coulomb

Using the wave function of Equation (2.23), we obtain an expression for the direct Coulomb interaction term defined earlier,

$$\langle \mathbf{k}_e, \mathbf{k}'_h \,|V|\, \mathbf{k}_h, \mathbf{k}'_e \rangle = \int d\mathbf{r}_1 d\mathbf{r}_2 \psi^*_{\mathbf{k}_e}(\mathbf{r}_1)\psi^*_{\mathbf{k}'_h}(\mathbf{r}_2)\frac{e^2}{|\mathbf{r}_1-\mathbf{r}_2|}\psi_{\mathbf{k}_h}(\mathbf{r}_2)\psi_{\mathbf{k}'_e}(\mathbf{r}_1) \tag{2.26}$$

where

$$\psi_{\mathbf{k}}(\mathbf{r}) = \frac{1}{\sqrt{\mathcal{N}}}\sum_{j=A,B} C_j(\mathbf{k}) \sum_{\mathbf{R}_j} e^{i\mathbf{k}\cdot\mathbf{R}_j}\phi(\mathbf{r}-\mathbf{R}_j). \tag{2.27}$$

is the tight-binding Bloch function. Plugging this in yields:

$$\begin{aligned}
&\langle \mathbf{k}_e, \mathbf{k}'_h \,|V|\, \mathbf{k}_h, \mathbf{k}'_e \rangle = \sum_{j_1,\mathbf{R}_{j_1}}\sum_{j_2,\mathbf{R}_{j_2}}\sum_{j_3,\mathbf{R}_{j_3}}\sum_{j_4,\mathbf{R}_{j_4}} C^*_{j_1}(\mathbf{k}_e)C^*_{j_2}(\mathbf{k}'_h)C_{j_3}(\mathbf{k}_h)C_{j_4}(\mathbf{k}'_e)\\
&\times e^{i\left(-\mathbf{k}_e\cdot\mathbf{R}_{j_1}-\mathbf{k}'_h\cdot\mathbf{R}_{j_2}+\mathbf{k}_h\cdot\mathbf{R}_{j_3}+\mathbf{k}'_e\cdot\mathbf{R}_{j_4}\right)}\\
&\times \int d\mathbf{r}_1 d\mathbf{r}_2 \phi^*(\mathbf{r}_1-\mathbf{R}_{j_1})\phi^*(\mathbf{r}_2-\mathbf{R}_{j_2})\frac{e^2}{|\mathbf{r}_1-\mathbf{r}_2|}\phi(\mathbf{r}_2-\mathbf{R}_{j_3})\phi(\mathbf{r}_1-\mathbf{R}_{j_4})\\
&\approx \frac{1}{\mathcal{N}^2}\sum_{j_1,\mathbf{R}_{j_1}}\sum_{j_2,\mathbf{R}_{j_2}} C^*_{j_1}(\mathbf{k}_e)C^*_{j_2}(\mathbf{k}'_h)C_{j_2}(\mathbf{k}_h)C_{j_1}(\mathbf{k}'_e)\\
&\times e^{i\left((\mathbf{k}'_e-\mathbf{k}_e)\mathbf{R}_{j_1}+(\mathbf{k}_h-\mathbf{k}'_h)\mathbf{R}_{j_2}\right)}\int d\mathbf{r}_1 d\mathbf{r}_2 \left|\phi(\mathbf{r}_1-\mathbf{R}_{j_1})\right|^2\frac{e^2}{|\mathbf{r}_1-\mathbf{r}_2|}\left|\phi(\mathbf{r}_2-\mathbf{R}_{j_2})\right|^2\\
&\approx \frac{1}{\mathcal{N}^2}\sum_{j_1,\mathbf{R}_{j_1}}\sum_{j_2,\mathbf{R}_{j_2}} C^*_{j_1}(\mathbf{k}_e)C^*_{j_2}(\mathbf{k}'_h)C_{j_2}(\mathbf{k}_h)C_{j_1}(\mathbf{k}'_e)\\
&\times e^{i\left((\mathbf{k}'_e-\mathbf{k}_e)(\mathbf{R}_{j_1}-\mathbf{R}_{j_2})+(\mathbf{k}'_e-\mathbf{k}_e+\mathbf{k}_h-\mathbf{k}'_h)\mathbf{R}_{j_2}\right)}\\
&\times \int d\mathbf{r}_1 d\mathbf{r}_2 \left|\phi(\mathbf{r}_1-\mathbf{R}_{j_1})\right|^2\frac{e^2}{|\mathbf{r}_1-\mathbf{r}_2|}\left|\phi(\mathbf{r}_2-\mathbf{R}_{j_2})\right|^2\\
&\approx \frac{\delta_{\mathbf{k}'_e-\mathbf{k}_e,\mathbf{k}'_h-\mathbf{k}_h}}{\mathcal{N}}\sum_{j_1}\sum_{j_2} C^*_{j_1}(\mathbf{k}_e)C^*_{j_2}(\mathbf{k}'_h)C_{j_2}(\mathbf{k}_h)C_{j_1}(\mathbf{k}'_e)\sum_{\mathbf{R}_{j_1}} e^{i(\mathbf{k}'_e-\mathbf{k}_e)(\mathbf{R}_{j_1}-\mathbf{r}_{j_2})}\\
&\times \int d\mathbf{r}_1 d\mathbf{r}_2 \left|\phi(\mathbf{r}_1-\mathbf{R}_{j_1})\right|^2\frac{e^2}{|\mathbf{r}_1-\mathbf{r}_2|}\left|\phi(\mathbf{r}_2-\mathbf{R}_{j_2})\right|^2\\
&\approx \frac{\delta_{\mathbf{k}'_e-\mathbf{k}_e,\mathbf{k}'_h-\mathbf{k}_h}}{\mathcal{N}}\sum_{j_1}\sum_{j_2} C^*_{j_1}(\mathbf{k}_e)C^*_{j_2}(\mathbf{k}'_h)C_{j_2}(\mathbf{k}_h)C_{j_1}(\mathbf{k}'_e)\\
&\times \sum_{\mathbf{R}_{j_1}} e^{i(\mathbf{k}'_e-\mathbf{k}_e)(\mathbf{R}_{j_1}-\mathbf{r}_{j_2})}v\left(|\mathbf{R}_{j_1}-\mathbf{r}_{j_2}|\right),
\end{aligned} \tag{2.28}$$

where

$$v\left(|\mathbf{R}_{j_1}-\mathbf{r}_{j_2}|\right)=\frac{U}{\sqrt{(U/e^2)\,|\mathbf{R}_{j_1}-\mathbf{r}_{j_2}|+1}}. \tag{2.29}$$

is the regularized Ohno potential [92, 108]. The reason for replacing the Coulomb potential with the Ohno potential is to avoid the numerical difficulties associated with the logarithmic divergence of the Coulomb potential. Instead of being infinite at $\mathbf{r}_1-\mathbf{r}_2=0$, the Ohno potential approaches a finite value of $U=11.3$ eV which is the energy cost of putting two electrons at the same position for π orbitals. Here, $\mathbf{r}_{j_2}$ are the coordinates of one A atom and one B atom on the carbon nanotube surface, and

$$|\mathbf{R}_{j_1}-\mathbf{r}_{j_2}|=\sqrt{(Z_{j_1}-z_{j_2})^2+d^2\sin^2((\Phi_{j_1}-\varphi_{j_2})/2)} \tag{2.30}$$

The expression for the direct Coulomb interaction in Equation (2.28) can be further simplified. It now takes the form,

$$\begin{aligned}&\langle\mu_e,q_e;\mu_h',q_h'\,|V|\,\mu_h,q_h;\mu_e',q_e'\rangle=\frac{\delta_{q_e'-q_e,q_h'-q_h}\delta_{\mu_e'-\mu_e,\mu_h'-\mu_h}}{\mathcal{N}}\\&\times\sum_{j_1}\sum_{j_2}C^*_{j_1}(\mu_e,q_e)C^*_{j_2}(\mu_h',q_h')C_{j_2}(\mu_h,q_h)C_{j_1}(\mu_e',q_e')\\&\times u_{j_1,j_2}(q_e-q_e',\mu_e-\mu_e'),\end{aligned} \tag{2.31}$$

where the following function is defined:

$$u_{j_1,j_2}(q,m)=\sum_{\mathbf{R}_{j_1}}e^{-iq(Z_{j_1}-z_{j_2})}e^{-im(\Phi_{j_1}-\varphi_{j_2})}v\left(|\mathbf{R}_{j_1}-\mathbf{r}_{j_2}|\right)=u^*_{j_1,j_2}(-q,-m) \tag{2.32}$$

Exchange Coulomb

Likewise, using the wave function of Equation (2.23), we obtain an expression for the exchange Coulomb interaction term defined earlier. The exchange Coulomb matrix

element is given by

$$\begin{aligned}
&\langle \mathbf{k}_e, \mathbf{k}'_h \,|V|\, \mathbf{k}'_e, \mathbf{k}_h \rangle = \int d\mathbf{r}_1 d\mathbf{r}_2 \psi^*_{\mathbf{k}_e}(\mathbf{r}_1)\psi^*_{\mathbf{k}'_h}(\mathbf{r}_2)\frac{e^2}{|\mathbf{r}_1-\mathbf{r}_2|}\psi_{\mathbf{k}'_e}(\mathbf{r}_2)\psi_{\mathbf{k}_h}(\mathbf{r}_1) \\
= \;& \frac{1}{\mathcal{N}^2}\sum_{j_1,\mathbf{R}_{j_1}}\sum_{j_2,\mathbf{R}_{j_2}}\sum_{j_3,\mathbf{R}_{j_3}}\sum_{j_4,\mathbf{R}_{j_4}} C^*_{j_1}(\mathbf{k}_e)C^*_{j_2}(\mathbf{k}'_h)C_{j_3}(\mathbf{k}'_e)C_{j_4}(\mathbf{k}_h) \\
&\times e^{i\left(-\mathbf{k}_e\cdot\mathbf{R}_{j_1}-\mathbf{k}'_h\cdot\mathbf{R}_{j_2}+\mathbf{k}'_e\cdot\mathbf{R}_{j_3}+\mathbf{k}_h\cdot\mathbf{R}_{j_4}\right)} \\
&\times \int d\mathbf{r}_1 d\mathbf{r}_2 \phi^*(\mathbf{r}_1-\mathbf{R}_{j_1})\phi^*(\mathbf{r}_2-\mathbf{R}_{j_2})\frac{e^2}{|\mathbf{r}_1-\mathbf{r}_2|}\phi(\mathbf{r}_2-\mathbf{R}_{j_3})\phi(\mathbf{r}_1-\mathbf{R}_{j_4}) \\
&\approx \frac{1}{\mathcal{N}^2}\sum_{j_1,\mathbf{R}_{j_1}}\sum_{j_2,\mathbf{R}_{j_2}} C^*_{j_1}(\mathbf{k}_e)C^*_{j_2}(\mathbf{k}'_h)C_{j_2}(\mathbf{k}'_e)C_{j_1}(\mathbf{k}_h)e^{i\left((\mathbf{k}_h-\mathbf{k}_e)\mathbf{R}_{j_1}+(\mathbf{k}'_e-\mathbf{k}'_h)\mathbf{R}_{j_2}\right)} \\
&\times \int d\mathbf{r}_1 d\mathbf{r}_2 \left|\phi(\mathbf{r}_1-\mathbf{R}_{j_1})\right|^2 \frac{e^2}{|\mathbf{r}_1-\mathbf{r}_2|}\left|\phi(\mathbf{r}_2-\mathbf{R}_{j_2})\right|^2 \\
&\approx \frac{1}{\mathcal{N}^2}\sum_{j_1,\mathbf{R}_{j_1}}\sum_{j_2,\mathbf{R}_{j_2}} C^*_{j_1}(\mathbf{k}_e)C^*_{j_2}(\mathbf{k}'_h)C_{j_2}(\mathbf{k}'_e)C_{j_1}(\mathbf{k}_h) \\
&\times e^{i\left((\mathbf{k}_h-\mathbf{k}_e)(\mathbf{R}_{j_1}-\mathbf{R}_{j_2})+(\mathbf{k}'_e-\mathbf{k}'_h-\mathbf{k}_e+\mathbf{k}_h)\mathbf{R}_{j_2}\right)} v\left(|\mathbf{R}_{j_1}-\mathbf{R}_{j_2}|\right) \\
&\approx \frac{\delta_{\mathbf{k}'_e-\mathbf{k}_e,\mathbf{k}'_h-\mathbf{k}_h}}{\mathcal{N}}\sum_{j_1,j_2} C^*_{j_1}(\mathbf{k}_e)C^*_{j_2}(\mathbf{k}'_h)C_{j_2}(\mathbf{k}'_e)C_{j_1}(\mathbf{k}_h) \\
&\times \sum_{\mathbf{R}_{j_1}} e^{i(\mathbf{k}_h-\mathbf{k}_e)(\mathbf{R}_{j_1}-\mathbf{r}_{j_2})} v\left(|\mathbf{R}_{j_1}-\mathbf{r}_{j_2}|\right) \qquad (2.33)
\end{aligned}$$

Again, the expression for the exchange Coulomb interaction can be simplified similarly to the direct term. This gives,

$$\begin{aligned}
&\langle \mu_e, q_e; \mu'_h, q'_h \,|V|\, \mu'_e, q'_e; \mu_h, q_h \rangle = \frac{\delta_{q'_e-q_e,q'_h-q_h}\delta_{\mu'_e-\mu_e,\mu'_h-\mu_h}}{\mathcal{N}} \\
&\times \sum_{j_1}\sum_{j_2} C^*_{j_1}(\mu_e,q_e)C^*_{j_2}(\mu'_h,q'_h)C_{j_2}(\mu'_e,q'_e)C_{j_1}(\mu_h,q_h)u_{j_1,j_2}(q_e-q_h,\mu_e-\mu_h)
\end{aligned} \qquad (2.34)$$

Dielectric Function

We consider the dielectric screening effect in the random phase approximation (RPA). We can express the screened Coulomb interaction as

$$w(q) = \frac{v(q)}{\kappa\varepsilon(q)} \qquad (2.35)$$

where $v(q)$ is the unscreened Coulomb interaction, κ is a static dielectric constant for the core states, σ bonds, and the surrounding environment, and $\varepsilon(q)$ is the dielectric function that describes screening from the π electrons. The reason for this choice is as follows. The Coulomb interaction in a medium with static dielectric constant κ is given as $v(q)/\kappa$. When we further consider the screening effect from the electrons, the interaction $v(q)/\kappa$ is further reduced under the RPA and is scaled by a dielectric function $1/\varepsilon(q)$, so we get $v(q)/\kappa\varepsilon(q)$. For this work, we include the screening effects from the core states, σ bonds, and the surrounding environment in the dielectric constant κ. Good agreement with experimental values is achieved when using $\kappa = 2$ [92]. The dielectric function, $\varepsilon(q)$, in the static limit ($\omega \to 0$) describing the effects of the polarization of the π bands and can be expressed as

$$\varepsilon(\mathbf{q}) = 1 + v(\mathbf{q})\Pi(\mathbf{q}) \tag{2.36}$$

where

$$v(\mathbf{q}) = \frac{1}{4\mathcal{N}} \sum_{j_1,j_2} u_{j_1,j_2}(\mathbf{q}), \tag{2.37}$$

$$\Pi(\mathbf{q}) = -2 \sum_{\mathbf{k},a,a'} \frac{f_{\mathbf{k}+\mathbf{q},a'} - f_{\mathbf{k},a}}{\varepsilon_{\mathbf{k}+\mathbf{q},a'} - \varepsilon_{\mathbf{k},a}} \left| \int \Psi^*_{\mathbf{k},a}(\mathbf{r}) e^{-i\mathbf{q}\cdot\mathbf{r}} \Psi_{\mathbf{k}+\mathbf{q},a'}(\mathbf{r}) d\mathbf{r} \right|^2 \tag{2.38}$$

and $a, a' = c, v$. From here on, we assume that $f_{\mathbf{k},c} = 0$ and $f_{\mathbf{k},v} = 1$ meaning that the conduction band is empty and the valence band is full. The polatization, Π, can then be rewritten as,

$$\begin{aligned} \Pi(\mathbf{q}) &= 2 \sum_{\mathbf{k}} \frac{1}{\varepsilon_{\mathbf{k}+\mathbf{q},c} + \varepsilon_{\mathbf{k},c}} \left(\left| \int \Psi^*_{\mathbf{k},c}(\mathbf{r}) e^{-i\mathbf{q}\cdot\mathbf{r}} \Psi_{\mathbf{k}+\mathbf{q},v}(\mathbf{r}) d\mathbf{r} \right|^2 \right. \\ &\quad \left. + \left| \int \Psi^*_{\mathbf{k},v}(\mathbf{r}) e^{-i\mathbf{q}\cdot\mathbf{r}} \Psi_{\mathbf{k}+\mathbf{q},c}(\mathbf{r}) d\mathbf{r} \right|^2 \right) \end{aligned} \tag{2.39}$$

where

$$\begin{aligned}
&\int \Psi^*_{\mathbf{k},c}(\mathbf{r}) e^{-i\mathbf{q}\cdot\mathbf{r}} \Psi_{\mathbf{k}+\mathbf{q},v}(\mathbf{r}) d\mathbf{r} = \\
&\frac{1}{\mathcal{N}} \sum_{j_1,\mathbf{R}_{j_1}} \sum_{j_2,\mathbf{R}_{j_2}} C^*_{j_1,c}(\mathbf{k}) C_{j_2,v}(\mathbf{k}+\mathbf{q}) e^{-i\mathbf{k}\cdot\mathbf{R}_{j_1}} e^{-i(\mathbf{k}+\mathbf{q})\cdot\mathbf{R}_{j_2}} \\
&\times \int \phi^*(\mathbf{r}-\mathbf{R}_{j_1}) e^{-i\mathbf{q}\cdot\mathbf{r}} \phi(\mathbf{r}-\mathbf{R}_{j_2}) d\mathbf{r} \\
&\approx \sum_{j_1,\mathbf{R}_{j_1}} \sum_{j_2} C^*_{j_1,c}(\mathbf{k}) C_{j_2,v}(\mathbf{k}+\mathbf{q}) e^{-i\mathbf{k}\cdot\mathbf{R}_{j_1}} e^{-i(\mathbf{k}+\mathbf{q})\cdot\mathbf{r}_{j_2}} \\
&\times \int \phi^*(\mathbf{r}-\mathbf{R}_{j_1}) e^{-i\mathbf{q}\cdot\mathbf{r}} \phi(\mathbf{r}-\mathbf{r}_{j_2}) d\mathbf{r} \\
&\approx \sum_{j} C^*_{j,c}(\mathbf{k}) C_{j,v}(\mathbf{k}+\mathbf{q}) \qquad (2.40)
\end{aligned}$$

Therefore,

$$\begin{aligned}
\Pi(\mathbf{q}) &= 2\sum_{\mathbf{k}} \frac{1}{\varepsilon_{\mathbf{k}+\mathbf{q},c} - \varepsilon_{\mathbf{k},c}} \left(\left| \sum_j C^*_{j,c}(\mathbf{k}) C_{j,v}(\mathbf{k}+\mathbf{q}) \right|^2 \right. \\
&\quad \left. + \left| \sum_j C^*_{j,v}(\mathbf{k}) C_{j,c}(\mathbf{k}+\mathbf{q}) \right|^2 \right) \\
&= \frac{1}{2}\sum_{\mathbf{k}} \frac{1}{\varepsilon_{\mathbf{k}+\mathbf{q},c} + \varepsilon_{\mathbf{k},c}} \left(\left|1 - e^{i(\varphi(\mathbf{k}+\mathbf{q}) - \varphi(\mathbf{k}))}\right|^2 + \left|1 - e^{i(\varphi(\mathbf{k}+\mathbf{q}) - \varphi(\mathbf{k}))}\right|^2 \right) \\
&= \sum_{\mathbf{k}} \frac{1}{\varepsilon_{\mathbf{k}+\mathbf{q},c} + \varepsilon_{\mathbf{k},c}} \left|1 - e^{i(\varphi(\mathbf{k}+\mathbf{q}) - \varphi(\mathbf{k}))}\right|^2 \\
&= 4\sum_{\mathbf{k}} \frac{1}{\varepsilon_{\mathbf{k}+\mathbf{q},c} + \varepsilon_{\mathbf{k},c}} \sin^2\left(\frac{\varphi(\mathbf{k}+\mathbf{q}) - \varphi(\mathbf{k})}{2} \right) \qquad (2.41)
\end{aligned}$$

For our calculations, we will be using the following form for the dielectric function:

$$\varepsilon(q,m) = 1 + u(q,m)\Pi(q,m), \qquad (2.42)$$

where

$$u(q,m) = \sum_{j_1,j_2} u_{j_1,j_2}(q,m), \tag{2.43}$$

$$\Pi(q,m) = \frac{1}{\mathcal{N}} \sum_{k,\mu} \frac{1}{\varepsilon_c(k+q,m+\mu)+\varepsilon_c(k,\mu)} \sin^2\left(\frac{\varphi(k+q,m+\mu)-\varphi(k,\mu)}{2}\right) \tag{2.44}$$

Electron Self-Energy

Now, let us revisit the self-energy terms and express them in terms of the single particle tight binding wave functions in Equation (2.23). We start with the electron self-energy,

$$\begin{aligned}
\Sigma_e(\mathbf{k}_e) &= \sum_{\mathbf{k}'_h} \langle \mathbf{k}_e \mathbf{k}'_h \left| V \right| \mathbf{k}_e, \mathbf{k}'_h \rangle \\
&= \sum_{\mathbf{k}'_h} \int d\mathbf{r}_1 d\mathbf{r}_2 \psi^*_{\mathbf{k}_e}(\mathbf{r}_1) \psi^*_{\mathbf{k}'_h}(\mathbf{r}_2) \frac{e^2}{|\mathbf{r}_1-\mathbf{r}_2|} \psi_{\mathbf{k}_e}(\mathbf{r}_2) \psi_{\mathbf{k}'_h}(\mathbf{r}_1) \\
&= \frac{1}{\mathcal{N}} \sum_{j_1,j_2} C^*_{j_1}(\mathbf{k}_e) C^*_{j_2}(\mathbf{k}'_h) C_{j_2}(\mathbf{k}_e) C_{j_1}(\mathbf{k}'_h) \\
&\quad \times \sum_{\mathbf{R}_{j_1}} e^{i(\mathbf{k}'_h-\mathbf{k}_e)(\mathbf{R}_{j_1}-\mathbf{r}_{j_2})} v\left(|\mathbf{R}_{j_1}-\mathbf{r}_{j_2}|\right)
\end{aligned} \tag{2.45}$$

Like the direct and exchange terms, the electron self-energy can be rewritten as

$$\Sigma_e(\mu_e,q_e) = \sum_{\mu'_h,q'_h} \sum_{j_1,j_2} C^*_{j_1}(\mu_e,q_e) C^*_{j_2}(\mu'_h,q'_h) C_{j_2}(\mu_e,q_e) C_{j_1}(\mu'_h,q'_h) u_{j_1,j_2}(q_e-q'_h,\mu_e-\mu'_h) \tag{2.46}$$

Performing the sum over j_1 and j_2 gives four terms:

$$\Sigma_{e,AA}(\mu_e, q_e) = \frac{1}{4\mathcal{N}} \sum_{\mu'_h, q'_h} u_{AA}(q_e - q'_h, \mu_e - \mu'_h)$$

$$\Sigma_{e,BB}(\mu_e, q_e) = \frac{1}{4\mathcal{N}} \sum_{\mu'_h, q'_h} u_{BB}(q_e - q'_h, \mu_e - \mu'_h)$$

$$\Sigma_{e,AB}(\mu_e, q_e) = -\frac{1}{4\mathcal{N}} \sum_{\mu'_h, q'_h} e^{i\left(\varphi(\mu'_h, q'_h) - \varphi(\mu_e, q_e)\right)} u_{AB}(q_e - q'_h, \mu_e - \mu'_h)$$

$$\Sigma_{e,BA}(\mu_e, q_e) = -\frac{1}{4\mathcal{N}} \sum_{\mu'_h, q'_h} e^{i\left(\varphi(\mu_e, q_e) - \varphi(\mu'_h, q'_h)\right)} u_{BA}(q_e - q'_h, \mu_e - \mu'_h)$$

Hole Self-Energy

As we did for the electron self-energy, we express the hole self-energy in terms of the single particle tight binding wave functions in Equation (2.23)

$$\begin{aligned}
\Sigma_h(\mathbf{k}_h) &= \sum_{\mathbf{k}'_h} \langle \mathbf{k}_h \mathbf{k}'_h \left| V \right| \mathbf{k}_h, \mathbf{k}'_h \rangle \\
&= \sum_{\mathbf{k}'_h} \int d\mathbf{r}_1 d\mathbf{r}_2 \psi^*_{\mathbf{k}_h}(\mathbf{r}_1) \psi^*_{\mathbf{k}'_h}(\mathbf{r}_2) \frac{e^2}{|\mathbf{r}_1 - \mathbf{r}_2|} \psi_{\mathbf{k}_h}(\mathbf{r}_2) \psi_{\mathbf{k}'_h}(\mathbf{r}_1) \\
&= \frac{1}{\mathcal{N}} \sum_{j_1, j_2} C^*_{j_1}(\mathbf{k}_h) C^*_{j_2}(\mathbf{k}'_h) C_{j_2}(\mathbf{k}_h) C_{j_1}(\mathbf{k}'_h) \\
&\quad \times \sum_{\mathbf{R}_{j_1}} e^{i(\mathbf{k}'_h - \mathbf{k}_h)(\mathbf{R}_{j_1} - \mathbf{r}_{j_2})} \upsilon\left(|\mathbf{R}_{j_1} - \mathbf{r}_{j_2}|\right)
\end{aligned} \tag{2.47}$$

This can be rewritten as

$$\begin{aligned}
\Sigma_h(\mu_h, q_h) &= \sum_{\mu'_h, q'_h} \sum_{j_1, j_2} C^*_{j_1}(\mu_h, q_h) C^*_{j_2}(\mu'_h, q'_h) C_{j_2}(\mu_h, q_h) C_{j_1}(\mu'_h, q'_h) \\
&\quad \times u_{j_1, j_2}(q_h - q'_h, \mu_h - \mu'_h)
\end{aligned} \tag{2.48}$$

Performing the sum over j_1 and j_2 again gives four terms:

$$\Sigma_{h,AA}(\mu_h, q_h) = \frac{1}{4\mathcal{N}} \sum_{\mu'_h, q'_h} u_{AA}(q_h - q'_h, \mu_h - \mu'_h)$$

$$\Sigma_{h,BB}(\mu_h, q_h) = \frac{1}{4\mathcal{N}} \sum_{\mu'_h, q'_h} u_{BB}(q_h - q'_h, \mu_h - \mu'_h)$$

$$\Sigma_{h,AB}(\mu_h, q_h) = \frac{1}{4\mathcal{N}} \sum_{\mu'_h, q'_h} e^{i\left(\varphi(\mu'_h, q'_h) - \varphi(\mu_h, q_h)\right)} u_{AB}(q_h - q'_h, \mu_h - \mu'_h)$$

$$\Sigma_{h,BA}(\mu_h, q_h) = \frac{1}{4\mathcal{N}} \sum_{\mu'_h, q'_h} e^{i\left(\varphi(\mu_h, q_h) - \varphi(\mu'_h, q'_h)\right)} u_{BA}(q_h - q'_h, \mu_h - \mu'_h)$$

2.3.6 Bright and Dark Excitons

Previously, we separated the singlet and triplet wave functions and derived the Bethe-Salpeter equation for the singlet exciton which is responsible for the optical absorption of SWNTs. However, even the singlet exciton has optically allowed and disallowed states. We distinguish these states as bright (optically active) and dark (optically disallowed) states. The stipulation of being optically allowed comes from parity. If the states have a dipole moment, they are optically allowed. Hence, a photon can excite an exciton to that state. If the state does not have a dipole moment, a photon can not promote an exciton to that level. Calculations of the dipole moments of the bright and dark excitons will be derived later in Section 2.3.8. To distinguish the bright and dark states, we make a change of variables: $q_e = q + Q/2$ and $q_h = q - Q/2$. For the bright (optically active) exciton:

$$\left[\Sigma_c(\mu, q + Q/2) + \Sigma_v(\mu, q - Q/2)\right] A^Q_{\mu,B}(q) + \sum_{q'} A^Q_{\mu,B}(q') \left[4V_x(\mu, q, Q; \mu, q')\right.$$
$$\left. -(V_d(\mu, q, Q; \mu, q') + V_d(\mu, q, Q; -\mu, -q'))\right] = \mathcal{E}_B(Q) A^Q_{\mu,B}(q) \tag{2.49}$$

and for the dark (optically inactive) exciton:

$$\begin{aligned}
&\left[\Sigma_c(\mu, q + Q/2) + \Sigma_v(\mu, q - Q/2)\right] A^Q_{\mu,D}(q) \\
&+ \sum_{q'} A^Q_{\mu,D}(q') \left[-(V_d(\mu, q, Q; \mu, q') + V_d(\mu, q, Q; -\mu, -q'))\right] \\
&= \mathcal{E}_D(Q) A^Q_{\mu,D}(q)
\end{aligned} \tag{2.50}$$

where the exciton wave function for the bright and dark excitons is given by

$$\Phi_{\alpha,Q}(\mathbf{r}_e,\mathbf{r}_h)=\sum_q A^Q_{\mu,\alpha}(q)\left(\Psi_{\mu,q+Q/2,e}(\mathbf{r}_e)\Psi^*_{\mu,q-Q/2,h}(\mathbf{r}_h)\right.$$
$$\left.+(-1)^\alpha\Psi_{-\mu,-q+Q/2,e}(\mathbf{r}_e)\Psi^*_{-\mu,-q-Q/2,h}(\mathbf{r}_h)\right) \tag{2.51}$$

where $\alpha=0,1$ for bright/dark.

Direct Coulomb, $\mu_e=\mu_h=\mu'_e=\mu'_h$

Here, we rewrite the expressions for the direct Coulomb interaction with our change of variables,

$$V_d(\mu,q,Q;\mu,q')=\langle\mu,q_e;\mu,q'_h\,|V|\,\mu,q_h;\mu,q'_e\rangle$$
$$=\frac{1}{\mathcal{N}}\sum_{j_1}\sum_{j_2}C^*_{j_1,e}(\mu,q+Q/2)C^*_{j_2,h}(\mu,q-Q/2)C_{j_2,h}(\mu,q-Q/2)$$
$$\times C_{j_1,e}(\mu,q+Q/2)u_{j_1,j_2}(q-q,0).$$

and,

$$V_{AA}(\mu,q,Q;\mu,q')=\frac{1}{4\mathcal{N}}e^{i(\varphi(\mu,q'+Q/2)+\varphi(\mu,q-Q/2)-\varphi(\mu,q'-Q/2)-\varphi(\mu,q+Q/2))}$$
$$\times u_{AA}(q-q',0),$$
$$V_{BB}(\mu,q,Q;\mu,q')=\frac{1}{4\mathcal{N}}u_{BB}(q-q',0),$$
$$V_{AB}(\mu,q,Q;\mu,q')=\frac{1}{4\mathcal{N}}e^{i(\varphi(\mu,q'+Q/2)-\varphi(\mu,q+Q/2))}u_{AB}(q-q',0),$$
$$V_{BA}(\mu,q,Q;\mu,q')=\frac{1}{4\mathcal{N}}e^{i(\varphi(\mu,q-Q/2)-\varphi(\mu,q'-Q/2))}u_{BA}(q-q',0).$$

Direct Interband Coulomb, $\mu_e=\mu_h=\mu,\mu'_e=\mu'_h=-\mu$

$$V_d(\mu,q,Q;-\mu,-q') = \frac{1}{\mathcal{N}}\sum_{j_1}\sum_{j_2}C^*_{j_1,e}(\mu,q+Q/2)C^*_{j_2,h}(-\mu,-q'-Q/2)$$
$$\times C_{j_2,h}(\mu,q-Q/2)C_{j_1,e}(-\mu,-q'+Q/2)u_{j_1,j_2}(q+q',2\mu).$$

$$V_{AA}(\mu,q,Q;-\mu,-q') = \frac{1}{4\mathcal{N}} e^{i(\varphi(\mu,-q'+Q/2)+\varphi(\mu,q-Q/2)-\varphi(\mu,-q'-Q/2)-\varphi(\mu,q+Q/2))}$$
$$\times u_{AA}(q+q',2\mu),$$
$$V_{BB}(\mu,q,Q;-\mu,-q') = \frac{1}{4\mathcal{N}} u_{BB}(q+q',2\mu),$$
$$V_{AB}(\mu,q,Q;-\mu,-q') = \frac{1}{4\mathcal{N}} e^{i(\varphi(\mu,-q'+Q/2)-\varphi(\mu,q+Q/2))} u_{AB}(q+q',2\mu),$$
$$V_{BA}(\mu,q,Q;-\mu,-q') = \frac{1}{4\mathcal{N}} e^{i(\varphi(\mu,q-Q/2)-\varphi(\mu,-q'-Q/2))} u_{BA}(q+q',2\mu).$$

Exchange Coulomb, $\mu_e = \mu_h = \mu'_e = \mu'_h$

$$V_x(\mu,q,Q;\mu,q') = \langle \mu,q_e;\mu,q'_h\,|V|\,\mu,q'_e;\mu,q_h\rangle$$
$$= \frac{1}{\mathcal{N}} \sum_{j_1}\sum_{j_2} C^*_{j_1,e}(\mu,q+Q/2) C^*_{j_2,h}(\mu,q'-Q/2) C_{j_2,e}(\mu,q'+Q/2)$$
$$\times C_{j_1,h}(\mu,q-Q/2) u_{j_1,j_2}(Q,0).$$

$$V_{AA}(\mu,q,Q;\mu,q') = \frac{1}{4\mathcal{N}} e^{i(\varphi(\mu,q'+Q/2)+\varphi(\mu,q-Q/2)-\varphi(\mu,q'-Q/2)-\varphi(\mu,q+Q/2))} u_{AA}(Q,0),$$
$$V_{BB}(\mu,q,Q;\mu,q') = \frac{1}{4\mathcal{N}} u_{BB}(Q,0),$$
$$V_{AB}(\mu,q,Q;\mu,q') = -\frac{1}{4\mathcal{N}} e^{i(\varphi(\mu,q-Q/2)-\varphi(\mu,q+Q/2))} u_{AB}(Q,0),$$
$$V_{BA}(\mu,q,Q;\mu,q') = -\frac{1}{4\mathcal{N}} e^{i(\varphi(\mu,q'+Q/2)-\varphi(\mu,q'-Q/2))} u_{BA}(Q,0).$$

2.3.7 Exciton Wave Function

We expand the bright and dark exciton wave function in terms of the single particle wave functions.

$$\Phi^{(n)}_{\alpha,Q}(\mathbf{r}_e,\mathbf{r}_h) = \sum_q A^{(n)}_{\alpha,Q}(q) \left(\Psi_{\mu,q+Q/2,e}(\mathbf{r}_e)\Psi^*_{\mu,q-Q/2,h}(\mathbf{r}_h)\right.$$
$$\left. +(-1)^\alpha \Psi_{-\mu,-q+Q/2,e}(\mathbf{r}_e)\Psi^*_{-\mu,-q-Q/2,h}(\mathbf{r}_h)\right) \tag{2.52}$$

$$
\begin{aligned}
&= \frac{1}{\mathcal{N}} \sum_{jj'} \sum_{\mathbf{R}_j, \mathbf{R}_{j'}} e^{iQ(z_j + z_{j'})/2} \sum_q A^n_{\alpha,Q}(q) \\
&\quad \times \left[C_{j,e}(\mu, q + Q/2) C^*_{j',v}(\mu, q - Q/2) e^{iq(z_j - z_{j'})} e^{i\mu(\varphi_j - \varphi_{j'})} \right. \\
&+ \quad \left. (-1)^\alpha C_{j,e}(-\mu, -q + Q/2) C^*_{j',v}(-\mu, -q - Q/2) e^{-iq(z_j - z_{j'})} e^{-i\mu(\varphi_j - \varphi_{j'})} \right] \\
&\quad \times \phi(\mathbf{r}_e - \mathbf{R}_j) \phi^*(\mathbf{r}_h - \mathbf{R}_{j'}) \\
&= \frac{1}{\mathcal{N}} \sum_{jj'} \sum_{\mathbf{R}_j, \mathbf{R}_{j'}} e^{iQ(z_j + z_{j'})/2} \sum_q A^n_{\alpha,Q}(q) \\
&\quad \times \left[C_{j,e}(\mu, q + Q/2) C^*_{j',v}(\mu, q - Q/2) e^{iq(z_j - z_{j'})} e^{i\mu(\varphi_j - \varphi_{j'})} \right. \\
&\quad \left. + (-1)^\alpha C^*_{j,e}(\mu, q - Q/2) C_{j',v}(\mu, q + Q/2) e^{-iq(z_j - z_{j'})} e^{-i\mu(\varphi_j - \varphi_{j'})} \right] \\
&\quad \times \phi(\mathbf{r}_e - \mathbf{R}_j) \phi^*(\mathbf{r}_h - \mathbf{R}_{j'})
\end{aligned}
\tag{2.53}
$$

where $\alpha = 0, 1$ for bright/dark. The relation $C_{j,s}(\mu, q) = C^*_{j,s}(-\mu, -q)$ has been applied to simplify the expression in the second part. In the case where $Q = 0$ we see that

$$
\begin{aligned}
\Phi^{(n)}_{\alpha,0}(\mathbf{r}_e, \mathbf{r}_h) &= \sum_q A^{(n)}_{\alpha,0}(q) \left(\Psi_{\mu,q,e}(\mathbf{r}_e) \Psi^*_{\mu,q,h}(\mathbf{r}_h) + (-1)^\alpha \Psi_{-\mu,-q,e}(\mathbf{r}_e) \Psi^*_{-\mu,-q,h}(\mathbf{r}_h) \right) \\
&= \frac{1}{\mathcal{N}} \sum_{jj'} \sum_{\mathbf{R}_j, \mathbf{R}_{j'}} \sum_q A^n_{\alpha,0}(q) \left[C_{j,e}(\mu, q) C^*_{j',v}(\mu, q) e^{iq(z_j - z_{j'})} e^{i\mu(\varphi_j - \varphi_{j'})} \right. \\
&+ \left. (-1)^\alpha C^*_{j,e}(\mu, q) C_{j',v}(\mu, q) e^{-iq(z_j - z_{j'})} e^{-i\mu(\varphi_j - \varphi_{j'})} \right] \phi(\mathbf{r}_e - \mathbf{R}_j) \phi^*(\mathbf{r}_h - \mathbf{R}_{j'})
\end{aligned}
\tag{2.54}
$$

This can be further simplified by separating the bright and dark wave functions and exploiting the fact that the two terms in the brackets are complex conjugates of one another which leaves:

$$
\begin{aligned}
\Phi^{(n)}_{B,0}(\mathbf{r}_e, \mathbf{r}_h) &= \frac{2}{\mathcal{N}} \sum_{jj'} \sum_{\mathbf{R}_j, \mathbf{R}_{j'}} \sum_q A^n_{B,0}(q) \mathrm{Re} \left[C_{j,e}(\mu, q) C^*_{j',v}(\mu, q) e^{iq(z_j - z_{j'})} e^{i\mu(\varphi_j - \varphi_{j'})} \right] \\
&\quad \times \phi(\mathbf{r}_e - \mathbf{R}_j) \phi^*(\mathbf{r}_h - \mathbf{R}_{j'})
\end{aligned}
\tag{2.55}
$$

and

$$\Phi^{(n)}_{D,0}(\mathbf{r}_e,\mathbf{r}_h) = \frac{2i}{\mathcal{N}}\sum_{jj'}\sum_{\mathbf{R}_j,\mathbf{R}_{j'}}\sum_{q} A^n_{D,0}(q)\mathrm{Im}\left[C_{j,e}(\mu,q)C^*_{j',v}(\mu,q)e^{iq(z_j-z_{j'})}e^{i\mu(\varphi_j-\varphi_{j'})}\right] \times\phi(\mathbf{r}_e-\mathbf{R}_j)\phi^*(\mathbf{r}_h-\mathbf{R}_{j'}) \quad (2.56)$$

2.3.8 Exciton Dipole Matrix Elements

Here, we derive the dipole moments for the bright and dark excitons. The dipole moment operator in second quantization can be written as

$$\hat{\mathbf{p}} = \sum_{\mu',q',\mu'',q''} a^\dagger_{\mu',q'}d^\dagger_{\mu'',q''}\left\langle c,\mu',q'\left|\mathbf{p}\right|v,\mu'',q''\right\rangle. \quad (2.57)$$

The exciton wave function in Equation (2.52) can be written in terms of electron and hole creation/annhilation operators:

$$\Phi^n_{\alpha,Q} = \sum_q A^n_{\alpha,Q}(q)\left[a^\dagger_{\mu,q+Q/2}d^\dagger_{\mu,q-Q/2} + (-1)^\alpha a^\dagger_{-\mu,-q+Q/2}d^\dagger_{-\mu,-q-Q/2}\right]. \quad (2.58)$$

where $\alpha = 0, 1$ for the bright (B) and dark (D) excitons. We can evaluate the transition dipole matrix element of an excitonic state with the ground state (state with zero excitons):

$$\begin{aligned}\left\langle\Phi^n_{\alpha,Q}\left|\hat{\mathbf{p}}\right|0\right\rangle &= \sum_q A^n_{\alpha,Q}(q)\sum_{\mu',q',\mu'',q''}\left[\left\langle 0\left|d_{\mu,q-Q/2}a_{\mu,q+Q/2}a^\dagger_{\mu',q'}d^\dagger_{\mu'',q''}\right|0\right\rangle\right.\\ &\times\left\langle c,\mu',q'\left|\mathbf{p}\right|v,\mu'',q''\right\rangle\\ &+(-1)^\alpha\left\langle 0\left|d_{-\mu,-q-Q/2}a_{-\mu,-q+Q/2}a^\dagger_{\mu',q'}d^\dagger_{\mu'',q''}\right|0\right\rangle\\ &\left.\times\left\langle c,\mu',q'\left|\mathbf{p}\right|v,\mu'',q''\right\rangle\right].\end{aligned}$$

Using the anti-commutation rules derived earlier for the electron and hole operators, the operators can be rearranged into normal ordering to obtain the result

$$\begin{aligned}\left\langle\Phi^n_{\alpha,Q}\left|\hat{\mathbf{p}}\right|0\right\rangle &= \sum_q A^n_{\alpha,Q}(q)\left[\left\langle c,\mu,q+Q/2\left|\mathbf{p}\right|v,\mu,q-Q/2\right\rangle\right.\\ &\left.+(-1)^\alpha\left\langle c,-\mu,-q+Q/2\left|\mathbf{p}\right|v,-\mu,-q-Q/2\right\rangle\right] \quad (2.59)\end{aligned}$$

We can define:

$$\begin{aligned}
\mathbf{p}_1(Q) &= \langle c,\mu,q+Q/2\,|\mathbf{p}|\,v,\mu,q-Q/2\rangle = \int d\mathbf{r}\ \Psi^*_{c,\mu,q+Q/2}(\mathbf{r})\ \mathbf{r}\ \Psi_{v,\mu,q-Q/2}(\mathbf{r}) \\
&= \frac{1}{N}\sum_{j,\mathbf{R}_j} C^*_{c,j}(\mu,q+Q/2)C_{v,j}(\mu,q-Q/2)\ e^{iQz_j}\mathbf{R}_j \\
\\
\mathbf{p}_2(Q) &= \langle c,-\mu,-q+Q/2\,|\mathbf{p}|\,v,-\mu,-q-Q/2\rangle \\
&= \int d\mathbf{r}\ \Psi^*_{c,-\mu,-q+Q/2}(\mathbf{r})\ \mathbf{r}\ \Psi_{v,-\mu,-q-Q/2}(\mathbf{r}) \\
&= \frac{1}{N}\sum_{j,\mathbf{R}_j} C^*_{c,j}(-\mu,-q+Q/2)C_{v,j}(-\mu,-q-Q/2)\ e^{iQz_j}\mathbf{R}_j
\end{aligned}$$

where the definitions for the single particle wavefunctions were used. We can take the relations for the TB coefficients into account:

$$C_{B,v}(\mu,q) = C_{B,c}(\mu,q) = \frac{1}{\sqrt{2}} \tag{2.60}$$

$$C_{A,v}(\mu,q) = -C_{A,c}(\mu,q) = \frac{e^{i\phi(\mu,q)}}{\sqrt{2}} \tag{2.61}$$

$$\phi(\mu,q) = -\phi(-\mu,-q) \tag{2.62}$$

to find that

$$\mathbf{p}_1(Q) = \mathbf{p}_2(Q) = \frac{1}{2N}\left[-\sum_{\mathbf{R}_A} e^{i[\phi(\mu,q-Q/2)-\phi(\mu,q+Q/2)]}e^{-iQz_A}\mathbf{R}_A + \sum_{\mathbf{R}_B} e^{-iQz_B}\mathbf{R}_B\right]. \tag{2.63}$$

Plugging this back into the expression for the transition dipole matrix element gives the final results:

$$\begin{aligned}
\left\langle \Phi^n_{B,Q}\,|\hat{\mathbf{p}}|\,0\right\rangle &= \frac{1}{N}\sum_q A^n_{B,Q}(q) \\
&\quad \times\left[-\sum_{\mathbf{R}_A} e^{i[\phi(\mu,q-Q/2)-\phi(\mu,q+Q/2)]}e^{-iQz_A}\mathbf{R}_A + \sum_{\mathbf{R}_B} e^{-iQz_B}\mathbf{R}_B\right] \\
\left\langle \Phi^n_{D,Q}\,|\hat{\mathbf{p}}|\,0\right\rangle &= 0.
\end{aligned} \tag{2.64}$$

We can now see that the bright exciton has a dipole moment which allows it to be optically active. However, the dark exciton has no dipole moment so it can not be accessed by single photon excitation.

2.3.9 Bound Exciton

Up to this point, we have considered a free exciton on the SWNT surface. However, when SWNTs are placed in a complex environment such as in solution with water molecules and ions, the potential felt by the exciton changes due to the change in the dielectric environment. Because of this change in potential, excitons can become trapped, or bound, to the site where the perturbation exists. Such a perturbation could be caused, for example, by trivalent rare earth ions. In this section, we include the potential of an ion placed in the vicinity of the SWNT and derive expressions to calculate the bound states that form due to the charged impurity [109].

We start with the exciton wave function

$$\begin{aligned}\Phi^{(n)}_{\alpha,Q}(\mathbf{r}_e,\mathbf{r}_h) &= \sum_q A^{(n)}_{\alpha,Q}(q)\left(\Psi_{\mu,q+Q/2,e}(\mathbf{r}_e)\Psi^*_{\mu,q-Q/2,h}(\mathbf{r}_h)\right. \\ &\left.+(-1)^{\alpha}\Psi_{-\mu,-q+Q/2,e}(\mathbf{r}_e)\Psi^*_{-\mu,-q-Q/2,h}(\mathbf{r}_h)\right), \end{aligned} \tag{2.65}$$

where $\alpha = 0, 1$ for bright and dark states, respectively.

Let us consider an impurity with total charge Ze. The Schrödinger equation for the exciton in the presence of the impurity is

$$\left(H_{BS} + H_{int}\right)\Psi^{(\xi)}(\mathbf{r}_e,\mathbf{r}_h) = E^{(\xi)}\Psi^{(\xi)}(\mathbf{r}_e,\mathbf{r}_h), \tag{2.66}$$

where the interaction Hamiltonian is given by

$$H_{int}(\mathbf{r}_e,\mathbf{r}_h) = H_h(\mathbf{r}_h) + H_e(\mathbf{r}_e) = \frac{Ze^2}{|\mathbf{r}_h - \mathbf{r}_p|} - \frac{Ze^2}{|\mathbf{r}_e - \mathbf{r}_p|}. \tag{2.67}$$

where the first term is the repulsive hole-impurity Coulomb term and the second term is the attractive electron-impurity Coulomb term (the impurity charge, Z, is positive). We look for a solution which is a linear combination of exciton wave functions:

$$\Psi^{(\xi)}(\mathbf{r}_e,\mathbf{r}_h) = \sum_{n',\alpha',Q'} U^{(\xi)}_{n',\alpha',Q'}\Phi^{(n')}_{\alpha',Q'}(\mathbf{r}_e,\mathbf{r}_h). \tag{2.68}$$

where U is the new amplitude of the scattered wave function. Plugging this wave function into the Schrödinger equation in Equation (2.66) gives us the scattering

equation:

$$\Omega_{\alpha}^{(n)}(Q)U_{n,\alpha,Q}^{(\xi)} + \sum_{n',\alpha',Q'} S_{\alpha,\alpha'}^{n,n'}(Q,Q')U_{n',\alpha',Q'}^{(\xi)} = E^{(\xi)}U_{n,\alpha,Q}^{(\xi)} \tag{2.69}$$

where Ω_α are the eigenvalues of the Bethe-Salpeter equation, $E^{(\xi)}$ are the new scattered eigenvalues, and the scattering matrix is defined by

$$\begin{aligned} S_{\alpha,\alpha'}^{n,n'}(Q,Q') &= \int d\mathbf{r}_e d\mathbf{r}_h \Phi_{\alpha,Q}^{(n)*}(\mathbf{r}_e,\mathbf{r}_h) H_{int}(\mathbf{r}_e,\mathbf{r}_h) \Phi_{\alpha',Q'}^{(n')}(\mathbf{r}_e,\mathbf{r}_h) \\ &= \sum_{q,q'} A_{\alpha,Q}^{(n)*}(q) A_{\alpha',Q'}^{(n')}(q') \\ &\quad \times \Big(G_{KK} + (-1)^{\alpha'} G_{KK'} + (-1)^{\alpha} G_{K'K} + (-1)^{\alpha+\alpha'} G_{K'K'} \Big) \end{aligned} \tag{2.70}$$

where we break the interaction into four components:

$$\begin{aligned} G_{KK} &= \int d\mathbf{r}_e d\mathbf{r}_h \Psi_{\mu,q+Q/2,e}^{*}(\mathbf{r}_e) \Psi_{\mu,q-Q/2,h}(\mathbf{r}_h) \\ &\quad \times H_{int}(\mathbf{r}_e,\mathbf{r}_h) \Psi_{\mu,q'+Q'/2,e}(\mathbf{r}_e) \Psi_{\mu,q'-Q'/2,h}^{*}(\mathbf{r}_h) \\ G_{KK'} &= \int d\mathbf{r}_e d\mathbf{r}_h \Psi_{\mu,q+Q/2,e}^{*}(\mathbf{r}_e) \Psi_{\mu,q-Q/2,h}(\mathbf{r}_h) \\ &\quad \times H_{int}(\mathbf{r}_e,\mathbf{r}_h) \Psi_{-\mu,-q'+Q'/2,e}(\mathbf{r}_e) \Psi_{-\mu,-q'-Q'/2,h}^{*}(\mathbf{r}_h) \\ G_{K'K} &= \int d\mathbf{r}_e d\mathbf{r}_h \Psi_{-\mu,-q+Q/2,e}^{*}(\mathbf{r}_e) \Psi_{-\mu,-q-Q/2,h}(\mathbf{r}_h) \\ &\quad \times H_{int}(\mathbf{r}_e,\mathbf{r}_h) \Psi_{\mu,q'+Q'/2,e}(\mathbf{r}_e) \Psi_{\mu,q'-Q'/2,h}^{*}(\mathbf{r}_h) \\ G_{K'K'} &= \int d\mathbf{r}_e d\mathbf{r}_h \Psi_{-\mu,-q+Q/2,e}^{*}(\mathbf{r}_e) \Psi_{-\mu,-q-Q/2,h}(\mathbf{r}_h) \\ &\quad \times H_{int}(\mathbf{r}_e,\mathbf{r}_h) \Psi_{-\mu,-q'+Q'/2,e}(\mathbf{r}_e) \Psi_{-\mu,-q'-Q'/2,h}^{*}(\mathbf{r}_h) \end{aligned} \tag{2.71}$$

Calculation of G

Here, we evaluate the scattering matrix components in terms of the exciton wave functions:

$$\begin{aligned} G_{KK} &= \int d\mathbf{r}_e d\mathbf{r}_h \Psi^*_{\mu,q+Q/2,e}(\mathbf{r}_e)\Psi_{\mu,q-Q/2,h}(\mathbf{r}_h) \\ &\quad \times H_{int}(\mathbf{r}_e,\mathbf{r}_h)\Psi_{\mu,q'+Q'/2,e}(\mathbf{r}_e)\Psi^*_{\mu,q'-Q'/2,h}(\mathbf{r}_h) \\ &= \delta_{q-q',(Q-Q')/2}\int d\mathbf{r}_e \Psi^*_{\mu,q+Q/2,e}(\mathbf{r}_e)H_e(\mathbf{r}_e)\Psi_{\mu,q'+Q'/2,e}(\mathbf{r}_e) \\ &\quad +\delta_{q-q',(Q-Q')/2}\int d\mathbf{r}_h \Psi_{\mu,q-Q/2,h}(\mathbf{r}_h)H_h(\mathbf{r}_h)\Psi^*_{\mu,q'-Q'/2,h}(\mathbf{r}_h) \end{aligned} \tag{2.72}$$

$$\begin{aligned} G_{K'K'} &= \int d\mathbf{r}_e d\mathbf{r}_h \Psi^*_{-\mu,-q+Q/2,e}(\mathbf{r}_e)\Psi_{-\mu,-q-Q/2,h}(\mathbf{r}_h) \\ &\quad \times H_{int}(\mathbf{r}_e,\mathbf{r}_h)\Psi_{-\mu,-q'+Q'/2,e}(\mathbf{r}_e)\Psi^*_{-\mu,-q'-Q'/2,h}(\mathbf{r}_h) \\ &= \delta_{q-q',(Q'-Q)/2}\int d\mathbf{r}_e \Psi^*_{-\mu,-q+Q/2,e}(\mathbf{r}_e)H_e(\mathbf{r}_e)\Psi_{-\mu,-q'+Q'/2,e}(\mathbf{r}_e) \\ &\quad +\delta_{q-q',(Q-Q')/2}\int d\mathbf{r}_h \Psi_{-\mu,-q-Q/2,h}(\mathbf{r}_h)H_h(\mathbf{r}_h)\Psi^*_{-\mu,-q'-Q'/2,h}(\mathbf{r}_h) \end{aligned} \tag{2.73}$$

Recall, the single electron tight-binding wave function is defined as

$$\Psi_{\mu,q,s}(\mathbf{r}) = \frac{1}{\sqrt{\mathcal{N}}}\sum_{j=A,B} C_{j,s}(\mu,q)\sum_{\mathbf{R}_j} e^{i\mu\varphi_j}e^{iqz_j}\phi(\mathbf{r}-\mathbf{R}_j) \tag{2.74}$$

Now, we can express the scattering matrix components in terms of the single-particle

TB wave function. This gives

$$
\begin{aligned}
G_{KK} &= \frac{\delta_{q-q',(Q-Q')/2}}{\mathcal{N}} \sum_{j,j'} C^*_{j,e}(\mu, q+Q/2) C_{j',e}(\mu, q'+Q'/2) \\
&\quad \times \sum_{\mathbf{R}_j, \mathbf{R}_{j'}} e^{i\mu(\varphi_{j'}-\varphi_j)} e^{i((q'+Q'/2)z_{j'}-(q+Q/2)z_j)} \\
&\quad \times \int d\mathbf{r}_e \phi^*(\mathbf{r}_e - \mathbf{R}_j) H_e(\mathbf{r}_e) \phi(\mathbf{r}_e - \mathbf{R}_{j'}) \\
&\quad + \frac{\delta_{q-q',(Q'-Q)/2}}{\mathcal{N}} \sum_{j,j'} C_{j,h}(\mu, q-Q/2) C^*_{j',h}(\mu, q'-Q'/2) \\
&\quad \times \sum_{\mathbf{R}_j, \mathbf{R}_{j'}} e^{i\mu(\varphi_j-\varphi_{j'})} e^{i((q-Q/2)z_j-(q'-Q'/2)z_{j'})} \\
&\quad \times \int d\mathbf{r}_h \phi(\mathbf{r}_h - \mathbf{R}_j) H_h(\mathbf{r}_h) \phi^*(\mathbf{r}_h - \mathbf{R}_{j'}) \\
&\approx \frac{\delta_{q-q',(Q-Q')/2}}{\mathcal{N}} \sum_j C^*_{j,e}(\mu, q+Q/2) C_{j,e}(\mu, q'+Q'/2) \sum_{\mathbf{R}_j} e^{i(Q-Q')z_j} H_e(\mathbf{R}_j) \\
&\quad + \frac{\delta_{q-q',(Q'-Q)/2}}{\mathcal{N}} \sum_j C^*_{j,h}(\mu, q'-Q'/2) C_{j,e}(\mu, q-Q/2) \sum_{\mathbf{R}_j} e^{i(Q'-Q)z_j} H_h(\mathbf{R}_j) \\
&= \frac{Ze^2}{\mathcal{N}} [\delta_{q-q',(Q'-Q)/2} \\
&\times \big(C^*_{A,h}(\mu, q'-Q'/2) C_{A,h}(\mu, q-Q/2) \Phi_A(Q'-Q) \\
&\quad + C^*_{B,h}(\mu, q'-Q'/2) C_{B,h}(\mu, q-Q/2) \Phi_B(Q'-Q) \big) \\
&- \delta_{q-q',(Q-Q')/2} \\
&\times \big(C^*_{A,e}(\mu, q+Q/2) C_{A,e}(\mu, q'+Q'/2) \Phi_A(Q-Q') \\
&\quad + C^*_{B,e}(\mu, q+Q/2) C_{B,e}(\mu, q'+Q'/2) \Phi_B(Q-Q') \big)] \qquad (2.75)
\end{aligned}
$$

$$
(2.76)
$$

where

$$
\Phi_j(Q) = \sum_{\mathbf{R}_j} \frac{e^{iQz_j}}{|\mathbf{R}_j - \mathbf{r}_p|} \qquad (2.77)
$$

In a similar calculation, $G_{K'K'}$ is

$$\begin{aligned} G_{K'K'} &= \frac{Ze^2}{\mathcal{N}}[\delta_{q-q',(Q-Q')/2} \\ &\times(C^*_{A,h}(-\mu,-q'-Q'/2)C_{A,h}(-\mu,-q-Q/2)\Phi_A(Q'-Q) \\ &+C^*_{B,h}(-\mu,-q'-Q'/2)C_{B,h}(-\mu,-q-Q/2)\Phi_B(Q'-Q)) \\ &-\delta_{q-q',(Q'-Q)/2} \\ &\times(C^*_{A,e}(-\mu,-q+Q/2)C_{A,e}(-\mu,-q'+Q'/2)\Phi_A(Q'-Q) \\ &+C^*_{B,e}(-\mu,-q+Q/2)C_{B,e}(-\mu,-q'+Q'/2)\Phi_B(Q'-Q))] \end{aligned} \tag{2.78}$$

$C_{A,B}$ Coefficients

From the tight-binding hamiltonian of graphene, the coefficients are given by

$$C_B(\mu_c,q_c)=\frac{1}{\sqrt{2}},\quad C_A(\mu_c,q_c)=\frac{-e^{i\varphi(\mu_c,q_c)}}{\sqrt{2}}, \tag{2.79}$$

$$C_B(\mu_v,q_v)=\frac{1}{\sqrt{2}},\quad C_A(\mu_v,q_v)=\frac{e^{i\varphi(\mu_v,q_v)}}{\sqrt{2}}. \tag{2.80}$$

Substituting these into Equations (2.76) and (2.78) gives,

$$\begin{aligned} G_{KK} &= \frac{Ze^2}{2\mathcal{N}}[\delta_{q-q',(Q'-Q)/2}\left(e^{i(\varphi(\mu,q-Q/2)-\varphi(\mu,q'-Q'/2))}\Phi_A(Q'-Q)+\Phi_B(Q'-Q)\right) \\ &- \delta_{q-q',(Q-Q')/2}\left(e^{i(\varphi(\mu,q'+Q'/2)-\varphi(\mu,q+Q/2))}\Phi_A(Q'-Q)+\Phi_B(Q'-Q)\right)] \end{aligned} \tag{2.81}$$

$$\begin{aligned} G_{K'K'} &= \frac{Ze^2}{2\mathcal{N}} \\ &\times [\delta_{q-q',(Q-Q')/2}\left(e^{i(\varphi(-\mu,-q-Q/2)-\varphi(-\mu,-q'-Q'/2))}\Phi_A(Q'-Q)+\Phi_B(Q'-Q)\right) \\ &- \delta_{q-q',(Q'-Q)/2}\left(e^{i(\varphi(-\mu,-q'+Q'/2)-\varphi(-\mu,-q+Q/2))}\Phi_A(Q'-Q)+\Phi_B(Q'-Q)\right)] \end{aligned} \tag{2.82}$$

Zigzag CNTs

For zigzag $(n, 0)$ nanotubes, the scattering matrix components can be further simplified. We note that $\varphi(\mu, q) = \varphi(-\mu, q)$ and $\varphi(\mu, -q) = -\varphi(\mu, q)$ for zigzag SWNTs. Therefore, we can simplify the scattering matrix components as

$$\begin{aligned} G_{K'K'} &= \frac{Ze^2}{2\mathcal{N}}[\delta_{q-q',(Q-Q')/2}\left(e^{i(\varphi(\mu,q'+Q'/2)-\varphi(\mu,q+Q/2))}\Phi_A(Q'-Q)+\Phi_B(Q'-Q)\right) \\ &- \delta_{q-q',(Q'-Q)/2}\left(e^{i(\varphi(\mu,q-Q/2)-\varphi(\mu,q'-Q'/2))}\Phi_A(Q'-Q)+\Phi_B(Q'-Q)\right)] \\ &= -G_{KK}. \end{aligned} \tag{2.83}$$

Chapter 3

SWNT Plasmonic Antenna

There have been a few theoretical treatments of SWNT antennas thus far. Nakanishi and Ando calculated the optical response of finite length carbon nanotubes [51]. They calculated the induced current distribution in a self-consistent manner and showed that the main resonance, caused by the excitation of the fundamental plasmon mode, had a length dependent resonance wave vector of π/L, where L is the length of the SWNT antenna. Burke et al. treated the metallic SWNT antenna as a flared out transmission line [110]. The main drawback to their method is that interband excitations are not included in their model. Therefore, they are restricted to the low-frequency regime below the interband transitions. The method developed by Hanson [111] numerically solves the Hallén integral equation. However, like the other model, interband transitions are not included so we are again restricted to the low frequency regime. Also, the thin wire kernel was used in the calculation to avoid singularities [112]. The solution of the Hallén equation with the thin wire kernel is not well defined as it generates non-physical oscillations near the edges of the SWNT [113, 114]. The work by Slepyan et al. included interband transitions of the SWNT derived from quantum transport theory [115, 116]. Using that, they were able to solve the integro-differential equation for the current distribution from both the Hallén equation as well as derive an approximate analytical expression when using the Leontovich-Levin equation. Their model uses the full, singular kernel and provides results for both semiconducting and metallic SWNTs. In the work done by

Joh et al., they used a quantum mechanical description of the exciton conductivity from the Bethe-Salpeter equation and showed experimentally that the intensity of the scattered fields was determined by the exciton dynamics when excited in the optical range [117]. Furthermore, radiative coupling between two excitonic wires was observed.

3.1 Transmission Line Model

To begin our model, we consider a line of charge with charge density $\lambda = \lambda_0 + \delta\lambda$ where λ_0 is the static charge density on the CNT and $\delta\lambda$ is the change in the charge density due to an external perturbation given by $\delta\lambda = es(z,t)$ where e is the electron charge and $s(z,t)$ is a displacement. We can define a dipole moment induced by the perturbation as $\mathcal{P} = e\lambda_0 s$. From that, we can arrive at an expression for the current density:

$$j = \frac{d\mathcal{P}}{dt} = e\lambda_0 \frac{ds}{dt} = e\lambda_0 v = \frac{e\lambda_0}{m} p \tag{3.1}$$

where p here is the 1D momentum of the particle.

3.1.1 Equation of Motion for Charged Particle

We start by writing the classical equation of motion for a charged particle:

$$\frac{dp}{dt} = F - \frac{p}{\tau_p} \tag{3.2}$$

where τ_p is a relaxation time of the momentum due to dissipative, non-conserving forces and F is the force on the particle given by

$$F = F_Q + F_{elec} = F_Q + F_{xt} + F_{ind} \tag{3.3}$$

F_Q is a quantum component of the force which is related to the electrochemical potential. The electric force is broken up into two components: a classical external force $F_{xt} = eE_{xt}$ and F_{ind} which is caused by fluctuations in the charge density.

3.1.2 Quantum Capacitance

The quantum component of the force is related to the electrochemical potential ξ:

$$F_Q = -\nabla\xi \tag{3.4}$$

The excess charge density is related to the 1D density of states by:

$$e\delta\lambda = e\int_0^{\xi} g(E)dE = \frac{4e}{\hbar\pi v_F}\frac{e}{e}\xi = \frac{4e^2}{\hbar\pi v_F}\xi/e = C_Q\xi/e \tag{3.5}$$

where we define the quantum capacitance

$$C_Q = \frac{4e^2}{\hbar\pi v_F} = \frac{4c}{\pi v_F}\alpha = \hbar g_0 c\alpha = \frac{4G_0}{v_F} \tag{3.6}$$

with the Fermi velocity $v_F \approx 10^8$ cm/s, $g_0 = 4/(\pi\hbar v_F)$ is the constant density of states for a metallic CNT, $\alpha = 1/137$ is the fine structure constant, and $G_0 = 2e^2/h$ is the quantum of conductance. Therefore, Equation (3.4) can be rewritten as:

$$F_Q = -e^2 C_Q^{-1}\nabla\delta\lambda \tag{3.7}$$

3.1.3 Geometric Capacitance

The induced force is given as

$$F_{ind} = -e\nabla\phi_{ind} \tag{3.8}$$

where the induced potential is given by the Poisson integral

$$\phi_{ind}(z) = \int_0^{L} e\delta\lambda(z')\mathcal{G}(z-z')dz' \tag{3.9}$$

The fluctuation of the charge density along the length of the tube $e\delta\lambda(z')$ is integrated with the 1D Coulomb kernel $\mathcal{G}(z-z') = \int d\theta/\sqrt{(z-z')^2 + 2R^2(1-\cos\theta)}$ where R is the radius of the CNT. We can integrate out the θ dependence because we assume any angular dependence of the charge density is negligible. In other words,

we are neglecting the perpendicular polarization of the CNT. The Fourier components of the 1D Coulomb kernel are given by the Bessel functions $I_0(kR)K_0(kR)$ with R being the cutoff parameter.

If we assume a slow dependence of $\delta\lambda(z')$, we can use a Taylor expansion:

$$\delta\lambda(z') = \delta\lambda(z) + \cancelto{0}{\frac{\partial\delta\lambda}{\partial z}}(z' - z) \tag{3.10}$$

Using this expansion, the charge density can be moved outside the integral and the result becomes

$$\phi_{ind}(z) = C_g^{-1} e\delta\lambda(z) \tag{3.11}$$

The leading term in the geometric capacitance C_g^{-1} is logarithmic due to the logarithmic divergence of the 1D coulomb kernel. A series expansion of the Bessel functions shows the logarithmic dependence

$$I_0(x)K_0(x) = \text{const} + \log(x) + O(x^2) \tag{3.12}$$

Since R is the cutoff parameter, a series expansion gives $C_g^{-1} \propto \log\frac{\lambda}{R}$ where λ is a characteristic screening length. Since the dependence of this parameter is weak due to the logarithm, we can replace it with the SWNT length L and we get

$$C_g^{-1} = \frac{1}{4\pi\epsilon_0} 2\log\frac{L}{R} \tag{3.13}$$

Plugging the result of Equation (3.11) into Equation (3.8) gives:

$$F_{ind} = -eC_g^{-1}\nabla\delta\lambda \tag{3.14}$$

3.1.4 TL Conductivity

Now, we take the results from Equations (3.7) and (3.14) and plug them back into the equation of motion, Equation (3.2), to get:

$$\frac{dp}{dt} = eE_{xt} - eC_g^{-1}\nabla\delta\lambda - eC_Q^{-1}\nabla\delta\lambda - \frac{p}{\tau_p} \tag{3.15}$$

Recall the relation between j and p given in Equation (3.1). Plugging this in gives:

$$\frac{m}{e\lambda_0}\frac{dj}{dt} = E_{xt} - \left(C_g^{-1} + C_Q^{-1}\right) e\nabla\delta\lambda - \frac{m}{e^2\lambda_0\tau_p}j \tag{3.16}$$

We can eliminate $\delta\lambda$ by using the Continuity Equation:

$$\nabla \cdot j + e\frac{d}{dt}\delta\lambda = 0 \tag{3.17}$$

and by taking the time derivative of Equation (3.16). Doing this gives us a telegrapher's equation:

$$\frac{m}{e\lambda_0}\frac{d^2j}{dt^2} = \frac{dE_{xt}}{dt} - \left(C_g^{-1} + C_Q^{-1}\right)\nabla^2 j - \frac{m}{e^2\lambda_0\tau_p}\frac{dj}{dt} \tag{3.18}$$

We perform a time Fourier transform and seek solutions of the form $j \sim e^{-i\omega t}$:

$$\frac{-i\omega m}{e^2\lambda_0}j = E_{xt} + \frac{1}{-i\omega(C_g^{-1} + C_Q^{-1})^{-1}}\nabla^2 j - \frac{m}{e^2\lambda_0\tau_p}j \tag{3.19}$$

The last term in the right hand side is due to Joule losses in the transmission line: the classical Drude conductivity of a 1D wire is given by $G_d = e^2\lambda_0\tau_p/m$. Therefore that last term is a resistance per unit length, $\mathcal{R}$. The second term on the right is due to the displacement current associated with the capacitance per unit length of the transmission line: $\mathcal{C} = 1/(C_g^{-1}+C_Q^{-1})$. The term on the left hand side is the classical kinetic inductance per unit length of the 1D wire: $\mathcal{L} = m/(e^2\lambda_0)$. Rewriting gives,

$$-i\omega\mathcal{L}j = E_{xt} + \frac{1}{-i\omega\mathcal{C}}\nabla^2 j - \mathcal{R}j \tag{3.20}$$

We can rearrange terms and arrive at an expression equivalent to Ohm's Law

$$j = \frac{i\omega\mathcal{L}^{-1}}{\omega^2 + i\omega\mathcal{R}\mathcal{L}^{-1} + \mathcal{L}^{-1}\mathcal{C}^{-1}\nabla^2}E_{xt} \tag{3.21}$$

or, in terms of the original variables,

$$j = \frac{i\omega\frac{e^2\lambda_0}{m}}{\omega^2 + i\frac{\omega}{\tau_p} - \frac{e^2\lambda_0}{m}(C_g^{-1} + C_Q^{-1})(-\nabla^2)}E_{xt} \tag{3.22}$$

$\mathcal{C}_g$	8.15 aF/μm
$\mathcal{C}_q$	77.5 aF/μm
$\mathcal{L}_k$	16 nH/μm
$\mathcal{R}$	16 kΩ/μm*

Table 3.1: Table of TL parameters and their values. (* Resistance value calculated with τ=1000 fs corresponding to a mean free path of 1 μm.)

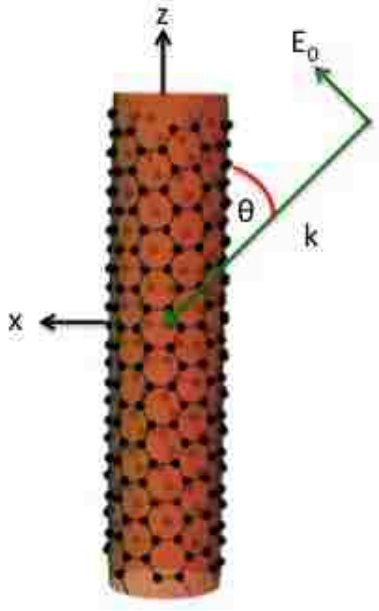

Figure 3.1: Geometry of the problem. A SWNT aligned along the z-axis with the coordinate origin at the center. The external field is a plane wave with magnitude E_0 and wave vector k incident at an angle θ with the z-axis.

3.1.5 Solution of the TL Differential Equation with Plane Wave Excitation

The geometry can be seen in Figure 3.1. Rearranging Equation (3.21), the differential equation we look to solve is

$$\left(\omega^2 + i\omega\mathcal{R}\mathcal{L}^{-1} + \mathcal{L}^{-1}\mathcal{C}^{-1}\partial_z^2\right) j(z) = i\omega\mathcal{L}^{-1}E_0 \sin\theta e^{ikz\cos\theta} \tag{3.23}$$

which is the solution of the TL equation for the current distribution with an external plane wave excitation (inhomogeneous term). For simplicity, let $k_p^2 = \mathcal{LC}(\omega^2 + i\omega\mathcal{RL}^{-1})$ and $B = i\omega\mathcal{C}E_0 \sin\theta$ so the inhomogeneous differential equation can be rewritten as

$$j''(z) + k_p^2 j(z) = Be^{ikz\cos\theta} \tag{3.24}$$

To solve this equation, we first begin by obtaining the general solution by solving the homogeneous equation

$$j''(z) + k_p^2 j(z) = 0 \tag{3.25}$$

This equation has a solution

$$j_g(z) = C_1 \cos(k_p z) + C_2 \sin(k_p z) \tag{3.26}$$

To find the particular solution, we first use a trial solution in the form of the right hand side of the differential equation. We start with

$$j_p(z) = De^{ikz\cos\theta} \tag{3.27}$$

where D is a constant to be determined by plugging this solution back into the differential equation. Doing this gives

$$-Dk^2\cos^2\theta e^{ikz\cos\theta} + k_p^2 De^{ikz\cos\theta} = Be^{ikz\cos\theta}$$

$$-Dk^2 + k_p^2 D = B$$

$$D = \frac{B}{k_p^2 - k^2\cos^2\theta} \tag{3.28}$$

So the particular solution is now

$$j_p(z) = \frac{B}{k_p^2 - k^2\cos^2\theta} e^{ikz\cos\theta} \tag{3.29}$$

The full solution is a sum of the general and particular solutions:

$$j(z) = j_g(z) + j_p(z) = C_1\cos(k_p z) + C_2\sin(k_p z) + \frac{B}{k_p^2 - k^2\cos^2\theta} e^{ikz\cos\theta} \tag{3.30}$$

This solution is now subject to the boundary conditions that $j(\pm L/2) = 0$. Applying these, we can solve for the constants C_1 and C_2

$$C_1 = \frac{-B\cos(kL\cos(\theta)/2)\sec(k_pL/2)}{k_p^2 - k^2\cos^2(\theta)} \tag{3.31}$$

$$C_2 = \frac{-B\sin(kL\cos(\theta)/2)\csc(k_pL/2)}{k_p^2 - k^2\cos^2(\theta)} \tag{3.32}$$

Note that the term $k\cos\theta$ appears in the expressions for the coefficients. This is just the component of the incoming electric field wave vector k parallel to the axis of the tube - the z axis. Therefore, to simplify the expressions, we can let $k_\parallel = k\cos\theta$. The coefficients can be rewritten as

$$C_1 = \frac{-B\cos(k_\parallel L/2)\sec(k_pL/2)}{k_p^2 - k_\parallel^2} \tag{3.33}$$

$$C_2 = \frac{-B\sin(k_\parallel L/2)\csc(k_pL/2)}{k_p^2 - k_\parallel^2} \tag{3.34}$$

Plugging these coefficients back into the expression for j in Equation (3.30) and simplifying gives the full solution for the current distribution:

$$\begin{aligned} j(z) = {} & \frac{B\csc(k_pL/2)\sec(k_pL/2)\left(-e^{ik_\parallel L/2}\sin(k_pL) + e^{ik_\parallel(L+z)}\sin(k_p(L-2z)/2)\right)}{2(k_\parallel^2 - k_p^2)} \\ & + \frac{B\csc(k_pL/2)\sec(k_pL/2)e^{ik_\parallel z}\sin(k_p(L+2z)/2)}{2(k_\parallel^2 - k_p^2)} \end{aligned} \tag{3.35}$$

λ_{mfp}	τ_p	$\mathcal{R}$
10 nm	10^{-14} s	1600 kΩ/μm
100 nm	10^{-13} s	160 kΩ/μm
1 μm	10^{-12} s	16 kΩ/μm
3 μm	3×10^{-12} s	5.33 kΩ/μm

Table 3.2: Table of NT resistances with their corresponding scattering times and mean free path lengths.

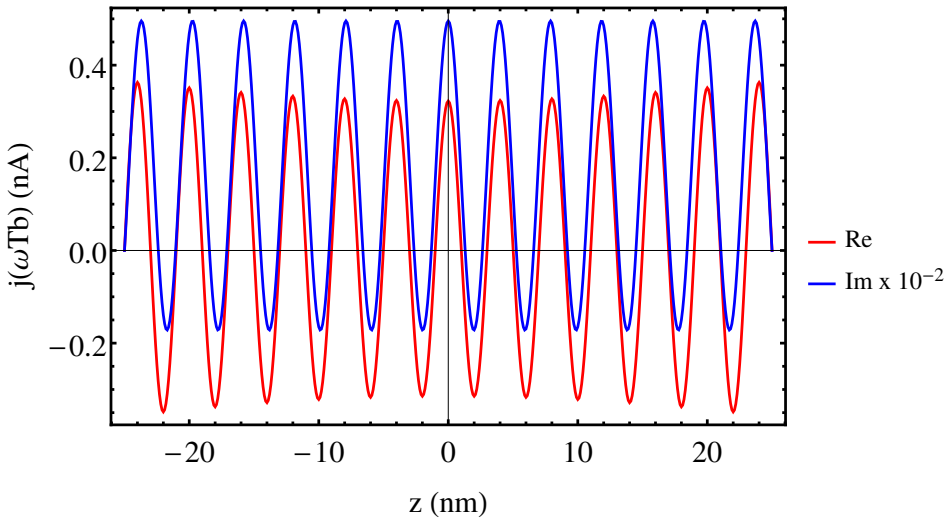

Figure 3.2: Calculated TL current of the SWNT at the Tb resonance at 2.54 eV for a 50 nm long SWNT. TL parameters used are from Table 3.1.

3.1.6 Special Case: $\theta = \pi/2$

If $\theta = \pi/2$, the expression in Equation (3.35) for the full current distribution can be simplified:

$$j(\omega, z) = \frac{i\omega\mathcal{C}E_0\left(\cos(k_p z)\sec(k_p L/2) - 1\right)}{k_p^2} \tag{3.36}$$

and the coefficients C_1 and C_2 can be simplified to

$$C_1 = \frac{-i\omega\mathcal{C}E_0\sec(k_p L/2)}{k_p^2} \tag{3.37}$$

$$C_2 = 0 \tag{3.38}$$

In this case, the conductivity of the NT can be written

$$\sigma(\omega, z) = \frac{i\omega\mathcal{C}\left(\cos(k_p z)\sec(k_p L/2) - 1\right)}{k_p^2} \tag{3.39}$$

and the current distribution is just

$$j(\omega, z) = \sigma(\omega, z)E_0 \tag{3.40}$$

In Figure 3.2, we show the calculated current from the TL model for a 50 nm long SWNT at the Terbium resonance of 2.54 eV. The real (red) and imaginary (blue) components are shown. The current distribution goes to zero at the ends of the SWNT as governed by the boundary conditions we implemented in the model.

3.2 Dielectric Function

We can define a phenomenological unitless dielectric function of the NT as

$$\epsilon(\omega) = 1 + \frac{1}{\epsilon_0} \frac{\alpha(\omega)}{2\pi R_{cn} L d} \tag{3.41}$$

where $\alpha(\omega) = i\sigma(\omega)/(\epsilon_0\omega)$. Since the polarizability, α, has units of volume, we need to divide it by an effective volume to make it unitless. In SWNTs, we can only accurately define that to the surface area which is $2\pi R_{cn} L$. That leaves one dimension of length undefined which we have called d. Here, we take $d = 2$ nm which is the effective size of an exciton. Figure 3.3 shows the dielectric function of Equation (3.41) in the THz range. The peaks show the frequencies of the plasmon resonances and it can be seen that the fundamental plasmon modes are in the low THz range which are well below the frequencies of the REI transitions.

3.3 Summary

We have derived a model for SWNT plasmon resonances by treating the SWNT as a transmission line. The model accurately replicates the plasmon resonances calculated by other models. The benefit of our model is that it is an analytic and inexpensive model as compared to numerical models used by others.

The fundamental plasmon resonances for SWNTs are in the THz frequency range as can be seen by Figure 3.3. However, in the visible/NIR range where REI transitions occur, we need to excite higher plasmon modes. The currents generated at the resonance frequency of Terbium have a sub-nanoamp magnitude. This magnitude of current will not have a large scattered field so the total field will be dominated by the external field. Therefore, we will not have any local field enhancements.

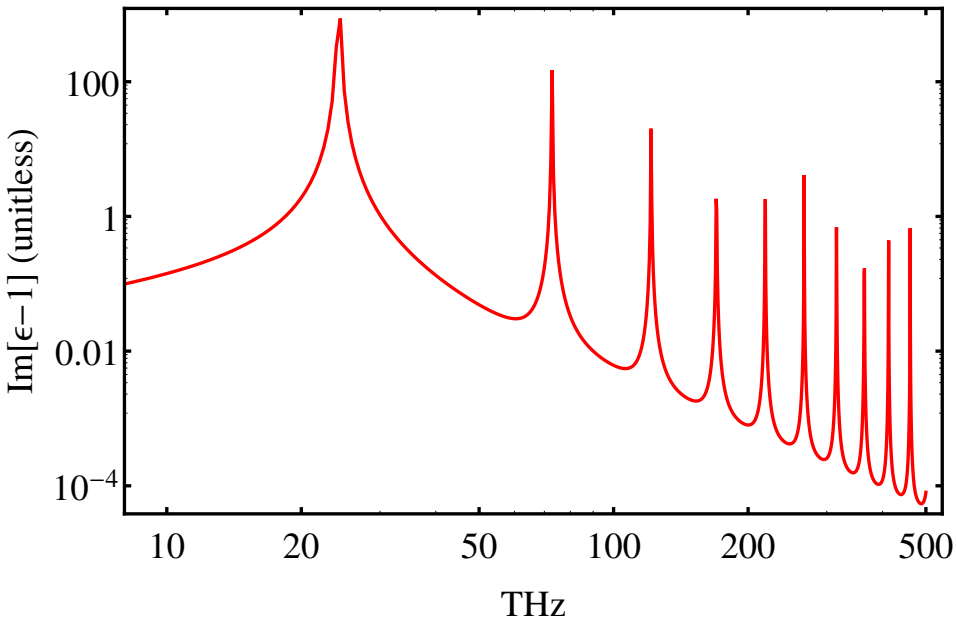

Figure 3.3: Log-log plot of the imaginary part of the dielectric function ϵ-1 as a function of frequency in the THz range.

There exists another problem when considering excitation in the visible/NIR range. By exciting the system in that range, we will also be exciting exciton resonances. These exciton resonances are not considered in the present TL model for plasmons. Therefore, in order to properly consider the local enhancements due to scattering in that frequency range, we need to include excitons into our model. This will be done in Chapter 4.

Chapter 4

SWNT Excitonic Antenna

In this chapter, we incorporate excitonic effects into SWNT antenna theory to obtain the antenna current distribution in the visible to NIR frequency range. From there, we can calculate the scattered and total fields around the SWNT antenna to observe locally enhanced hotspots of the polarization field. The spatial correlation of these hotspots are due to the light-matter interaction between the excitation field and the SWNT antenna. In these local hotspots, we calculate the excitation enhancements of multiple REI transitions with the most predominant SWNT chiralities used in experiments.

4.1 Historical Context

In 1947, T. Holstein published a theoretical paper on the imprisonment of resonance radiation in gases [118]. The basis of that paper was that a resonance quantum (photon) is highly absorbed by an atom. But if we were to place many of these atoms into a gas-filled enclosure, the escape of that quantum from the enclosure would require a large number of repeated absorptions and emissions as it traveled through. He formulated this radiative transport of excitation using a Boltzmann-type integro-differential equation,

$$\frac{\partial n(\mathbf{r})}{\partial t} = -\gamma n(\mathbf{r}) + \gamma \int n(\mathbf{r}')g(\mathbf{r},\mathbf{r}')d\mathbf{r}' \tag{4.1}$$

where $n(\mathbf{r})$ is the density of excited atoms, γ is the inverse radiative lifetime of the excited state, and $g(\mathbf{r}, \mathbf{r}')$ is the Green's function that is specified for certain cases such as Doppler and dispersion broadening of the resonance line in an infinite slab of gas. In his studies, he assumes isotropic emission of the particles. Therefore he is neglecting polarization effects because he states that "imprisonment has a strong depolarizing effect on resonance radiation emanating from a region originally excited by a polarized beam." By making this assumption, he arrives at an expression for his Green's function as

$$g(\mathbf{r}, \mathbf{r}') = -\frac{1}{4\pi\rho}\frac{\partial T(\rho)}{\partial \rho} \tag{4.2}$$

where $T(\rho)$ is the transmission coefficient related to the mean free path λ by

$$\lambda = -\int_0^\infty \rho \frac{\partial T(\rho)}{\partial \rho} d\rho. \tag{4.3}$$

where ρ is the distance traveled by the radiation. The transmission coefficient can be written explicitly for the specific cases of Doppler and dispersion broadening that he discusses.

In 1951, Holstein published the second part of his original paper [119]. There, he extended his treatment to a new type of enclosure geometry which was an infinite cylinder. His results for the cylindrical geometry were not much different from his results for the infinite planar 1D treatment because the symmetry between the two problems was the same so we should not expect a different result.

So far, the theory has been applied to systems with no order in polarizable matter. What Holstein did is valid for gas enclosures or color centers in glasses. To be more relevant to our system, we seek solutions for crystal lattices. The equation of motion for the electromagnetic interaction of identical oscillators which form a crystal of finite dimensions was derived by Muzikar in 1962 [120]. There, each single molecule dipole was acted on by four forces: (1) the elastic and dissipative forces associated with the dynamics of the isolated dipole with a particular frequency and broadening, (2) the retarded electric field of all the other dipoles, (3) the dipole's own field, and (4) the force of the driving field that causes the dipoles to be excited.

This equation of motion was expanded upon by Dubovskii in 1998 [121]. He theoretically studied superradiance of polaritons in 1D crystals. Superradiance is a quantum optics phenomenon that occurs when a dense group of N emitters interacts coherently with a common light field. When the wavelength of the light is much larger than the separation of the emitters (lattice constant of the crystal), then the emitters interact with the light in a collective and coherent fashion leading to an increase in emission with rate $\propto N^2$. This increase in emission is greater than that expected from spontaneous emission alone which has a rate $\propto N$. Dubovskii took Muzikar's expression for the equation of motion of a system of dipole emitters and wrote it in the form

$$\begin{aligned}\left(\omega^2-\omega_0^2+2i\gamma_0\omega_0\right)p_n^j &= \frac{e^2}{2\pi^2\mu}\int dq\frac{q^jq^j-(\omega^2/c^2)\delta_{jk}}{q^2-(\omega^2/c^2)-i\epsilon} \\ &\quad\times\sum_{m\neq n}p_m^k\exp\left[iq^1a(n-m)\right] \end{aligned} \tag{4.4}$$

where ω_0 is the resonant frequency of the dipole oscillators with charge e, mass μ, dipole moment $\mathbf{p}_n$ at node n with displacement $\mathbf{r}_n$, $\gamma_0 = e^2\omega_0^2/3\mu c$ is the intrinsic radiative half-width, $j,k = 1,2,3$ indicate the polarization indices (index 1 lies along the 1D crystal), and the term with $q^2-(\omega^2/c^2)-i\epsilon$ in the denominator is the photon's Green's function with $i\epsilon\to+0$. This Green's function comes from the quantization of the vector potential due to molecular dipole transitions and derivations can be found in [122] and [123]. From there, he was able to derive a dispersion relation for the polaritons

$$\begin{aligned}&\left(\omega^2-\omega_0^2+2i\gamma_0\omega_0\right) = \\ &\frac{4\omega_0\left|P\right|^2}{\hbar a^3(N+1)}\sum_{n\neq m}\left[\left(\frac{1}{|n-m|^3}-\frac{i\omega a/c}{|n-m|^2}\right)(1-3\cos^3\theta)-\frac{(\omega a/c)^2}{|n-m|}(1-cos^2\theta)\right] \\ &\times\exp\left(i\frac{i\omega a}{c}\left|n-m\right|\right)\sin(k_jn)\sin(k_jm)\end{aligned} \tag{4.5}$$

where P is the atomic dipole matrix element, N is the number of dipole oscillators, and θ is the angle of inclination of the dipoles relative to the crystal axis. There appears a term proportional to $(|n-m|^{-3})$ which corresponds to the dipole-dipole

interaction of the Coulomb kernel at short distances (near-field), a term proportional to $(|n-m|^{-2})$ for the interaction in the intermediate zone, and a term proportional to $(|n-m|^{-1})$ which is the interaction in the far-field zone. The k_j come from the orthonormalized eigenfunctions of a system of N nodes,

$$\psi_n(k_j) = \left(\frac{2}{N+1}\right)^{1/2} \sin(k_j n), \;\; k_j = \frac{\pi j}{N+1} \tag{4.6}$$

where $j = 1, 2, \cdots, N$. It is worthy to note that the frequency, ω, appearing in the dispersion equation (4.5) appears in a complex form $\omega = \omega_j = \omega_j' - i\omega_j''$, with real (ω_j') and imaginary (ω_j'') parts. Dubovskii goes on to evaluate the evolution of the dispersion curve for a number of dipoles ranging from $N = 2$ to $N = 70$. He traces the appearance and evolution of the radiative $(\omega > kc)$ and non-radiative $(\omega < kc)$ polariton branches.

Studies of superradiance are continuing even today. Marlan Scully's group published a paper in 2016 that examined superradiance and radiation trapping at the single photon level [124]. In his study, he began with an equation of motion which is almost identical to that used by Holstein. Scully's equation of motion was written as an eigenvalue equation

$$-i\gamma \int d\mathbf{r}' n(\mathbf{r}') \frac{\exp(ik_0|\mathbf{r}-\mathbf{r}'|)}{k_0|\mathbf{r}-\mathbf{r}'|} \beta(\mathbf{r}') = \Gamma\beta(\mathbf{r}) \tag{4.7}$$

where $\beta(\mathbf{r}, t) = \exp(-\Gamma t)\beta(\mathbf{r})$ is the probability amplitude of finding the atom at position $\mathbf{r}$ excited at time t, γ is the single atom decay rate, $k_0 = \omega/c$ is the wave number associated with the atomic transition, and $n(\mathbf{r})$ is the atomic density. Here, Γ is the eigenvalue which determines the evolution of the atomic system. The real part gives the decay rate and the imaginary part describes the frequency (Lamb) shift of the collective excitation. He solved this equation for the spherical shell, spheroidal shell, and infinite cylinder geometries. Here, we will discuss the cylindrical geometry since it is of most relevant interest to our problem. The geometry is an infinitely long cylinder of radius R along the z-axis. He found an interesting result for the eigenvalues:

$$\Gamma = \frac{\pi\gamma n_0}{k_0} J_n\left(\sqrt{k_0^2 - k_z^2}R\right) H_n^{(1)}\left(\sqrt{k_0^2 - k_z^2}R\right) \tag{4.8}$$

where n_0 is the number of atoms per unit length, k_z is the wave number of the mode along the cylinder axis, J_n is the Bessel function of the first kind, and $H_n^{(1)}$ is the Hankel function of the first kind. For the case where $k_z \ll k_0$, he found radiative modes (Re[Γ] > 0), while for $k_z > k_0$, (Re[Γ]=0). In other words, when the wave vector along the axis is greater than the cutoff wave vector, the superradiant mode is trapped and can no longer decay radiatively.

4.2 Derivation of Exciton Conductivity

4.2.1 Semi-Classical Description

We begin with the equation of motion for a single damped dipole in an external field

$$\ddot{\mathbf{p}} + \gamma\dot{\mathbf{p}} + \omega_0^2\mathbf{p} = \frac{e^2}{m}\mathbf{E}(t) \tag{4.9}$$

where the first term corresponds to the acceleration, the second term is damping, the third is the harmonic force which incorporates resonant transitions, and the right side of the equation is the driving field which consists of the self-consistent combination of the external field as well as the influence of the dipole distribution's own local field on itself. The solution of this equation for the dipole gives

$$\mathbf{p}(\mathbf{x}) = \frac{e^2}{m}\frac{1}{\omega_0^2 - \omega^2 - i\gamma\omega}\mathbf{E}_0(\mathbf{x}) \tag{4.10}$$

This is the equation for the contribution of a single oscillator. If the number density of the oscillators is $\mathcal{N}$ and we assume a 3D uniform, continuous distribution of excited dipoles, we can write the complex dielectric displacement vector as

$$\begin{aligned}\mathbf{D}(\mathbf{x}) &= \epsilon_0\mathbf{E}(\mathbf{x}) + \mathbf{P}(\mathbf{x}) = \epsilon_0\mathbf{E}(\mathbf{x}) + \epsilon_0\chi_e\mathbf{E}(\mathbf{x}) = \epsilon_0(1+\chi_e)\mathbf{E}(\mathbf{x}) = \varepsilon\mathbf{E}(\mathbf{x}) \\ &= \epsilon_0\left(1 + \frac{\mathcal{N}e^2}{m}\frac{1}{\omega_0^2 - \omega^2 - i\gamma\omega}\right)\mathbf{E}(\mathbf{x})\end{aligned} \tag{4.11}$$

Here, we can define the complex dielectric function ε as

$$\frac{\varepsilon(\omega)}{\epsilon_0} = \left(1 + \frac{\mathcal{N}e^2}{\epsilon_0 m}\frac{1}{\omega_0^2 - \omega^2 - i\gamma\omega}\right) \tag{4.12}$$

From this definition of ε and the above relations, we can define the polarizability of the exciton (in units of $\mathrm{fs^2C^2/kg}$):

$$\alpha(\omega) = \epsilon_0 \chi_e = \frac{Ne^2}{m} \frac{1}{\omega_0^2 - \omega^2 - i\gamma\omega} \tag{4.13}$$

where now, N is the number of carbon atoms given by

$$N = \frac{4L(n^2 + nm + m^2)}{a_0\sqrt{3(n^2 + nm + m^2)}} \tag{4.14}$$

and the conductivity (units of $\mathrm{nm^2}/\Omega$) is

$$\sigma(\omega) = -i\omega\alpha = \frac{Ne^2}{m} \frac{-i\omega}{\omega_0^2 - \omega^2 - i\gamma\omega} \tag{4.15}$$

So far, we have only considered one resonant transition. However, in a SWNT, there are multiple exciton resonances to consider. Including more than one resonance, we can express the conductivity as

$$\sigma(\omega) = \frac{Ne^2}{m} \sum_j \frac{-if_j\omega}{\omega_j^2 - \omega^2 - i\gamma_j\omega} \tag{4.16}$$

where f_j are the oscillator strengths per carbon atom. We can expand this into its real and imaginary parts

$$\Re[\sigma(\omega)] = \frac{Ne^2}{m} \sum_j \frac{\omega^2 f_j \gamma_j}{(\omega_j^2 - \omega^2)^2 + \gamma_j^2\omega^2} \tag{4.17}$$

and

$$\Im[\sigma(\omega)] = \frac{Ne^2}{m} \sum_j \frac{-\omega f_j(\omega_j^2 - \omega^2)}{(\omega_j^2 - \omega^2)^2 + \gamma_j^2\omega^2} \tag{4.18}$$

4.2.2 Quantum Description: Two-Level System

In quantum mechanics, the behavior of a system of N particles is described by the system's wave function

$$\Psi(\mathbf{r}, t) = \Psi(\mathbf{r}_1, \mathbf{r}_2, \cdots, \mathbf{r}_N, t) \tag{4.19}$$

where $\mathbf{r}_i$ denotes the coordinate of particle i at time t. This wave function is a solution of the time dependent Schrödinger equation

$$\hat{H}\Psi(\mathbf{r},t) = i\hbar\frac{d}{dt}\Psi(\mathbf{r},t) \tag{4.20}$$

where $\hat{H}$ is the Hamiltonian operator. For an isolated atom with no perturbations, the Hamiltonian is time independent and we can separate the spatial and temporal dependence of the wave function as

$$\Psi(\mathbf{r},t) = \sum_{n=1}^{\infty} e^{-iE_n t/\hbar}\psi_n(\mathbf{r}) \tag{4.21}$$

Inserting this wave function into Equation (4.20) and using $\hat{H} = \hat{H}_0$ gives the time independent Schrödinger equation

$$\hat{H}_0\psi_n(\mathbf{r}) = E_n\psi_n(\mathbf{r}) \tag{4.22}$$

where E_n are the eigenvalues of the stationary states $|n\rangle$. Let us now restrict ourselves to the case of a two-level system ($n = 1, 2$). We can write the two stationary wave functions as

$$\Psi_1(\mathbf{r},t) = e^{-iE_1 t/\hbar}\psi_1(\mathbf{r}) \tag{4.23}$$

$$\Psi_2(\mathbf{r},t) = e^{-iE_2 t/\hbar}\psi_2(\mathbf{r}) \tag{4.24}$$

Now, we can include the radiation field. This enters as an external, time-dependent perturbation, $\hat{H}'(t)$. The total Hamiltonian is then,

$$\hat{H} = \hat{H}_0 + \hat{H}'(t) \tag{4.25}$$

Since the radius of our SWNT and exciton size are much less than the wavelength of light, $R_{cn}, R_{exciton} \ll \lambda$, we can assume that the electric field is constant across the dimensions of our system. Using a time harmonic field, we have

$$\mathbf{E}(\mathbf{r},t) = \mathrm{Re}\left(\mathbf{E}(\mathbf{r})e^{-i\omega t}\right) \approx \mathbf{E}_0\cos(\omega t) \tag{4.26}$$

The interaction of a dipole with an external field is given by

$$\hat{H}' = -\mathbf{p}(\mathbf{r})\cdot\mathbf{E}_0\cos(\omega t). \tag{4.27}$$

To solve the time dependent Schrödinger equation (4.20) for our perturbed system, we write the total wave function of the system as a superposition of our two states

$$\Psi(\mathbf{r},t) = c_1(t)\Psi_1(\mathbf{r},t) + c_2(t)\Psi_2(\mathbf{r},t) \tag{4.28}$$

where the coefficients c_1 and c_2 are chosen such that the normalization condition $\langle\Psi|\Psi\rangle = \int \Psi^*\Psi dV = |c_1|^2 + |c_2|^2 = 1$ is fulfilled. Plugging this wave function into Equation (4.20) gives

$$\hat{H}'\left(c_1(t)\Psi_1(\mathbf{r,t}) + c_2(t)\Psi_2(\mathbf{r,t})\right) = i\hbar\left(\dot{c}_1\dot{\Psi}_1(\mathbf{r,t}) + \dot{c}_1\dot{\Psi}_1(\mathbf{r,t})\right) \tag{4.29}$$

To remove the spatial dependence, we multiply Equation (4.29) on the left by Ψ_1^* and integrate over all space. Then we exploit the normalization and orthogonality of the wave functions, i.e. $\langle\Psi_1|\Psi_2\rangle = 0$ and $\langle\Psi_1|\Psi_1\rangle = 1$. We then repeat this by multiplying Equation (4.29) on the left by Ψ_2^* and integrating over all space. This gives us two coupled time dependent equations

$$\dot{c}_1(t) = c_2(t)\frac{i}{\hbar}\mathbf{p}_{12}\cdot\mathbf{E}_0\cos(\omega t)e^{-i(E_2-E_1)t/\hbar} \tag{4.30}$$

$$\dot{c}_2(t) = c_1(t)\frac{i}{\hbar}\mathbf{p}_{21}\cdot\mathbf{E}_0\cos(\omega t)e^{i(E_2-E_1)t/\hbar} \tag{4.31}$$

where we have introduced the dipole matrix element

$$\mathbf{p}_{ij} = \langle i|\mathbf{p}|j\rangle = \int \psi_i^*(\mathbf{r})\mathbf{p}(\mathbf{r})\psi_j(\mathbf{r})d\mathbf{r} \tag{4.32}$$

It is worthy to note that due to $\mathbf{p}$ being a Hermitian operator, the dipole matrix elements must satisfy $\mathbf{p}_{12} = \mathbf{p}_{21}^*$. This can be further simplified by conveniently choosing the phases of the eigenfunctions ψ_1 and ψ_2 such that the matrix elements are real, i.e. $\mathbf{p}_{12} = \mathbf{p}_{21}$. We can also introduce the transition frequency defined by

$$\omega_0 = (E_2 - E_1)/\hbar = \Delta E/\hbar \tag{4.33}$$

One aspect of the problem which our derivation thus far has not included is spontaneous emission. This term would come from including a quantized radiation field term in the total Hamiltonian. To account for spontaneous emission without

including the quantized radiation field, we can introduce it by a phenomenological damping term into the equation for $\dot{c}_2$. Our coupled differential equations now take the form

$$\dot{c}_1(t) = c_2(t)\frac{i}{\hbar}\mathbf{p}_{12}\cdot\mathbf{E}_0\cos(\omega t)e^{-i\omega_0 t/\hbar} \tag{4.34}$$

$$\dot{c}_2(t)+\gamma c_2(t) = c_1(t)\frac{i}{\hbar}\mathbf{p}_{21}\cdot\mathbf{E}_0\cos(\omega t)e^{i\omega_0 t/\hbar} \tag{4.35}$$

where $1/\gamma$ is the damping parameter. The inclusion of the damping term ensures that the excited state must decay to its ground state. If the radiation field is absent ($\mathbf{E}_0 = 0$), then Equation (4.35) can be integrated directly to give

$$c_2(t) = c_2(0)e^{-\gamma t} \tag{4.36}$$

where $1/\gamma = \tau$ is the lifetime of the excited state. To solve the full set of coupled equations with the external field present, we seek an iterative method. To get the first order term, we can set $c_1(t) = 1$ and $c_2(t) = 0$ (so the system is completely in the ground state) on the right hand side of the coupled equations. Then those solutions can be plugged back in to get the second order correction, and so forth. Here, we will restrict ourselves to the first order case. The solution for c_1 is $c_1(t) = 1$ which indicates that the system always resides in the ground state. To get the first order solution for c_2, we express the result as a sum of the homogeneous equation (4.36) and a particular solution from Equation (4.35). We obtain for the first order solution for c_2,

$$c_2(t) = \frac{\mathbf{p}_{21}\cdot\mathbf{E}_0}{2\hbar}\left[\frac{e^{i(\omega_0+\omega)t}}{\omega_0+\omega-i\gamma}+\frac{e^{i(\omega_0-\omega)t}}{\omega_0-\omega-i\gamma}\right]+c_2(0)e^{-\gamma t} \tag{4.37}$$

where we have used the relation

$$\cos(\omega t) = \frac{e^{i\omega t}+e^{-i\omega t}}{2} \tag{4.38}$$

Now, we can express the dipole moment in terms of these coefficients. The expectation value of the dipole moment is given by

$$\mathbf{p}(t) = \langle\Psi|\mathbf{p}|\Psi\rangle = \int \Psi^*(\mathbf{r},t)\mathbf{p}(\mathbf{r})\Psi(\mathbf{r},t)d\mathbf{r}. \tag{4.39}$$

Using the wave function in Equation (4.28), the expectation value becomes

$$\mathbf{p}(t) = c_1^* c_2 \mathbf{p}_{12} e^{-i\omega_0 t} + c_1 c_2^* \mathbf{p}_{21} e^{i\omega_0 t} \tag{4.40}$$

Plugging in our first order expressions for c_1 and c_2, we get

$$\mathbf{p}(t) = \frac{\mathbf{p}_{12}(\mathbf{p}_{21} \cdot \mathbf{E}_0)}{2\hbar} \left[\frac{e^{i\omega t}}{\omega_0 + \omega - i\gamma} + \frac{e^{-i\omega t}}{\omega_0 - \omega - i\gamma} + \frac{e^{-i\omega t}}{\omega_0 + \omega + i\gamma} + \frac{e^{i\omega t}}{\omega_0 - \omega + i\gamma} \right]. \tag{4.41}$$

We can write the external field as

$$\mathbf{E} = \frac{\mathbf{E}_0}{2} \left(e^{i\omega t} + e^{-i\omega t} \right) \tag{4.42}$$

so we can simplify the dipole moment as

$$\mathbf{p}(t) = \frac{1}{2} \left[\overline{\alpha}^*(\omega) e^{i\omega t} + \overline{\alpha}(\omega) e^{-i\omega t} \right] \mathbf{E}_0 = \mathrm{Re} \left[\overline{\alpha}(\omega) e^{-i\omega t} \right] \mathbf{E}_0, \tag{4.43}$$

where $\overline{\alpha}(\omega)$ is the polarizability tensor

$$\overline{\alpha}(\omega) = \frac{\mathbf{p}_{12}\mathbf{p}_{21}}{\hbar} \left[\frac{1}{\omega_0 - \omega - i\gamma} + \frac{1}{\omega_0 + \omega + i\gamma} \right]. \tag{4.44}$$

Here, $\mathbf{p}_{12}\mathbf{p}_{21}$ is the outer product of the real transition moments. A final simplification can be made. We can represent the terms in brackets as one denominator. While doing this, we drop terms in γ^2 because it is much less than ω_0. Also, we generalize the equations to account for more than just two levels by summing over the states, n. Doing this gives the final form

$$\overline{\alpha}(\omega) = \sum_n \frac{e^2}{m} \frac{\overline{f}_n}{\omega_n^2 - \omega^2 - i\gamma_n \omega} \tag{4.45}$$

where e is the electron charge, m is the electron mass, and we define the oscillator strength as

$$\overline{f}_n = \frac{2m\omega_n}{e^2\hbar} \mathbf{p}_{1n}\mathbf{p}_{n1} \tag{4.46}$$

The expression for the polarizability given here in Equation (4.45) is equivalent to the expression derived in the previous section using the classical driven damped oscillator model as shown in Equation (4.13).

4.2.3 Rotating Wave Approximation

Recall Equation (4.44):

$$\overline{\alpha}(\omega) = \frac{\mathbf{p}_{12}\mathbf{p}_{21}}{\hbar}\left[\frac{1}{\omega_0 - \omega - i\gamma} + \frac{1}{\omega_0 + \omega + i\gamma}\right]$$

In this expression, we have two terms: the first term has $\omega_0 - \omega - i\gamma$ in the denominator while the second has $\omega_0 + \omega + i\gamma$. Near resonance, the term with $1/(\omega_0 - \omega)$ will be very much larger than the term with $1/(\omega_0 + \omega)$. Therefore, we can drop the second term in the expression since $1/(\omega_0 + \omega) \ll 1/(\omega_0 - \omega)$. This is known as the Rotating Wave Approximation (RWA). We are then left with

$$\overline{\alpha}(\omega) = \frac{\mathbf{p}_{12}\mathbf{p}_{21}}{\hbar}\left[\frac{1}{\omega_0 - \omega - i\gamma}\right] \tag{4.47}$$

which gives for a final form (defining the oscillator strength as we did before)

$$\overline{\alpha}(\omega) = \sum_n \frac{e^2}{m}\frac{\overline{f}_n}{\omega_n - \omega - i\gamma_n} \tag{4.48}$$

Near resonance, the RWA is a valid approximation. It is used frequently in quantum electrodynamic (QED) calculations where it greatly simplifies susceptibility tensors [125]. However, the RWA is not only restricted to QED calculations. It is also used in semiclassical theory near resonance.

For our calculations, we do not use the RWA for our polarizability or conductivity. We examine the behavior of our system at a wide range of frequencies going from well below resonance to well above resonance. Therefore, the RWA is not necessary for our model and we proceed with the Lorentzian polarizability in Equation (4.45).

If we return to the left hand side of Equation (4.4) for Dubovskii's equation of motion, it is evident that the RWA was not used in his derivations.

4.2.4 Distribution Function

If we specify the excitonic wave function, we can further evaluate Equation (4.39) to obtain a position dependence of the expectation value of the dipole moment. We

start with a localized exciton wave function

$$\Psi_{\alpha}^{nR}(\mathbf{x}) = C\sum_{q}\int d\mathbf{r}\int dQ\exp\left(\frac{-(\mathbf{r}-\mathbf{R})^2}{2\sigma}\right)\exp\left(i\mathbf{Q}\mathbf{r}\right)A_{\alpha Q}^{n}(q)\phi_q(\mathbf{x}) \tag{4.49}$$

where C is a constant determined from the normalization, $\exp(i\mathbf{Q}\mathbf{r})$ is the free exciton plane wave, $A_{\alpha Q}^{n}(q)\phi_q(\mathbf{x})$ is the free exciton envelope wave function which depends on the electron-hole separation distance $\mathbf{x}$, and we localize the exciton at a position $\mathbf{R}$ with a Gaussian envelope. Recall from Equations (2.59) and (2.63), the expectation value of the dipole operator. However, in terms of the localized excitonic wave function above in Equation (4.49), the expectation value takes the following form

$$\begin{aligned}\left\langle \Psi_{\alpha}^{nR}\left|p^{\dagger}\right|0\right\rangle &= \int d\mathbf{r}\int dQ\exp\left(\frac{-(\mathbf{r}-\mathbf{R})^2}{2\sigma}\right)\exp\left(-i\mathbf{Q}\mathbf{r}\right)\sum_{q}p_1(q)A_{\alpha Q}^{n}(q)\\ &= \int d\mathbf{r}\int dQ\exp\left(\frac{-(\mathbf{r}-\mathbf{R})^2}{2\sigma}\right)\exp\left(-i\mathbf{Q}\mathbf{r}\right)p_{\alpha}^{n}(Q)\end{aligned}$$

where we have defined $p_{\alpha}^{n}(Q)=\sum_{q}p_1(q)A_{\alpha Q}^{n}(q)$. We can now approximate $p_{\alpha}^{n}(Q)\approx p_{\alpha}^{n}(0)$ because the dipole moment has a weak dependence on Q. Doing this gives,

$$\begin{aligned}\left\langle \Psi_{\alpha}^{nR}\left|p^{\dagger}\right|0\right\rangle &\approx Cp_{\alpha}^{n}(0)\int d\mathbf{r}\int dQ\exp\left(\frac{-(\mathbf{r}-\mathbf{R})^2}{2\sigma}\right)\exp\left(-i\mathbf{Q}\mathbf{r}\right)\\ &= Cp_{\alpha}^{n}(0)\int dQ\sqrt{\sigma}\exp\left(-iQR\right)\exp\left(\frac{-Q^2\sigma}{2}\right)\\ &= Cp_{\alpha}^{n}(0)\exp\left(\frac{-R^2}{2\sigma}\right)=P(R)\end{aligned} \tag{4.50}$$

where $P(R)$ is the localized dipole matrix element, or, equivalently, the dipole distribution function.

4.3 Integral Equation for NT Current

4.3.1 Derivation of Integral Equation

From Maxwell's equations and the Lorentz gauge, we can define the inhomogeneous wave equation for the vector potential as

$$\left(\nabla^2 + k^2\right) \mathbf{A}(\mathbf{r}) = -\mu_0 \mathbf{J}(\mathbf{r}) \tag{4.51}$$

where $\mathbf{A}(\mathbf{r})$ is the vector potential, $\mathbf{J}$ is the source current, and $k = \omega/c$ is the free space wave vector. We can solve for the scalar Green's function for the Helmholtz operator by replacing the source term with a delta function

$$\left(\nabla^2 + k^2\right) G_0(\mathbf{r}, \mathbf{r}') = -\delta(\mathbf{r} - \mathbf{r}') \tag{4.52}$$

In free space, the solution of this equation is

$$G_0(\mathbf{r}, \mathbf{r}') = \frac{\exp(ik|\mathbf{r} - \mathbf{r}'|)}{4\pi|\mathbf{r} - \mathbf{r}'|} \tag{4.53}$$

which we can use to solve for the vector potential by

$$\mathbf{A}(\mathbf{r}) = \mu_0 \int \mathbf{J}(\mathbf{r}') G_0(\mathbf{r}, \mathbf{r}') d\mathbf{r}' \tag{4.54}$$

Everything to this point was defined for the vector potential. To describe what happens to the fields, we need to use tensors. The reason is that for the vector potential, a source current in the x-direction leads to a vector potential in the x-direction. But a source current in the x-direction leads to electric and magnetic fields with x-, y-, and z-components. The same is true for a source current in y- or z-directions. Therefore, we need a Green's function that relates all components of the source with all components of the fields. Again from Maxwell's equations, we can obtain the wave equation for the electric field

$$\nabla \times \nabla \times \mathbf{E}(\mathbf{r}) - k^2 \mathbf{E}(\mathbf{r}) = i\omega\mu_0 \mathbf{J}(\mathbf{r}) \tag{4.55}$$

We can obtain the dyadic Green's function for the vector Helmholtz equation similarly to before by replacing the source term with a delta function:

$$\nabla \times \nabla \times \mathbb{G}(\mathbf{r}, \mathbf{r}') - k^2 \mathbb{G}(\mathbf{r}, \mathbf{r}') = \mathbb{I}\delta(\mathbf{r} - \mathbf{r}') \tag{4.56}$$

Doing this gives,

$$\mathbb{G}(\mathbf{r},\mathbf{r}') = \left(\mathbb{I} + \frac{1}{k^2}\nabla\nabla\right)\frac{\exp(ik|\mathbf{r}-\mathbf{r}'|)}{4\pi|\mathbf{r}-\mathbf{r}'|} \tag{4.57}$$

where $k = \omega/c$ is the free space wavenumber, c is the speed of light in free space, and $\mathbb{I}$ is the identity dyadic. The electric field can be obtained from

$$\mathbf{E}(\mathbf{r}) = \frac{i\omega}{\epsilon_0 c^2}\int \mathbb{G}(\mathbf{r},\mathbf{r}')\cdot\mathbf{J}(\mathbf{r}')d\mathbf{r}' \tag{4.58}$$

We can rewrite the wave equation in terms of the dyads as

$$\left[(\nabla\times\mathbb{I})\cdot(\nabla\times\mathbb{I}) - k^2\mathbb{I}\right]\cdot\mathbf{E}(\mathbf{r}) = \frac{i\omega}{\epsilon_0 c^2}\mathbf{J}(\mathbf{r}) \tag{4.59}$$

Let the SWNT be aligned parallel to the z-axis of a cartesian coordinate system (x, y, z) with the centroid of the SWNT at the origin of the coordinate system as shown in Figure 3.1. Any point on the SWNT surface can be found from

$$\mathbf{r}_{cn} = R_{cn}\left(\cos\phi\hat{x} + \sin\phi\hat{y}\right) + z\hat{z}, \quad \phi\in[0,2\pi), \quad z\in[-L/2, L/2] \tag{4.60}$$

We assume that the induced surface current density, $\mathbf{J}$, is independent of ϕ and is purely axial: $\mathbf{J}(z) = J(z)\hat{z}$. This assumption smears the exciton distribution over the circumference of the SWNT. This is a valid assumption because the Bohr radius of the excitons, a_B, is larger than the radius of the SWNT: $a_B > R_{cn}$, and S_1 bright excitons correspond to the $m = 0$ angular momentum component of the two particle wave function. Also, for plane wave excitation, the source field is homogeneous along the SWNT circumference because the wavelength of light, λ, is much greater than the radius and greater than the length of the SWNT: $\lambda \gtrsim L \gg R_{cn}$. The current density also needs to satisfy the boundary condition at the edges

$$J(\pm L/2) = 0 \tag{4.61}$$

which ensures there no current density at the edges.

The total electric field can be expressed as

$$\mathbf{E}(\mathbf{r}) = \mathbf{E}^{inc}(\mathbf{r}) + \mathbf{E}^{sc}(\mathbf{r}) \tag{4.62}$$

where $\mathbf{E}^{inc}(\mathbf{r})$ is the incident field (which will be defined later), and the scattered field is given by

$$\mathbf{E}^{sc}(\mathbf{r}) = \frac{i\omega}{\epsilon_0 c^2} \int \mathbb{G}(\mathbf{r}, \mathbf{r}') \cdot \mathbf{J}(z) d\mathbf{r}'. \tag{4.63}$$

We can obtain an axial surface conductivity by relating the current distribution to the axial electric field from

$$E_z(\mathbf{r}) = \frac{J_z(z)}{\sigma(\omega)} \tag{4.64}$$

where we have used the local continuum approximation where we take σ to be coordinate independent. Taking the z-component of Equation (4.63), we get

$$E_z^{sc}(\mathbf{r}) = \frac{i\omega}{\epsilon_0 c^2} \int G_{zz}(\mathbf{r}, \mathbf{r}') J_z(z') d\mathbf{r}' \tag{4.65}$$

Combine with Equation (4.62) to get

$$\begin{aligned}
E_z(\mathbf{r}) &= E_z^{inc}(\mathbf{r}) + \frac{i\omega}{\epsilon_0 c^2} \int G_{zz}(\mathbf{r}, \mathbf{r}') J_z(z') d\mathbf{r}' \\
\frac{J(z)}{\sigma(\omega)} &= E_z^{inc}(z) + \frac{i\omega}{\epsilon_0 c^2} \int G_{zz}(\mathbf{r}, \mathbf{r}') J_z(z') d\mathbf{r}' \\
\frac{J(z)}{\sigma(\omega)} - E_z^{inc}(z) &= \frac{i\omega}{\epsilon_0 c^2} \int G_{zz}(\rho, \Phi, z, \rho', \Phi', z') J_z(z') \delta(\rho' - R_{cn}) \rho' d\rho' d\Phi' dz' \\
&= \frac{i\omega R_{cn}}{\epsilon_0 c^2} \int_{-L/2}^{L/2} \int_{-\pi}^{\pi} G_{zz}(\rho, \Phi, z, R_{cn}, \Phi', z') J_z(z') d\Phi' dz'
\end{aligned}$$

where we have used $d\mathbf{r}' = \rho' d\rho' d\Phi' dz'$ and we have restricted the current distribution to only exist at the surface of the SWNT by implementing the delta function

relationship $\delta(\rho' - R_{cn})$. Further simplifying gives,

$$\begin{aligned}
&= \frac{i\omega R_{cn}}{\epsilon_0 c^2} \int_{-L/2}^{L/2} \int_{-\pi}^{\pi} \left(1 + \frac{1}{k^2}\partial_z^2\right) \frac{\exp[ik\sqrt{4R_{cn}^2 \sin^2(\phi'/2) + (z-z')^2}]}{4\pi\sqrt{4R_{cn}^2 \sin^2(\phi'/2) + (z-z')^2}} J_z(z') d\phi' dz' \\
&= \left(1 + \frac{1}{k^2}\partial_z^2\right) \frac{i\omega R_{cn}}{4\pi\epsilon_0 c^2} \int_{-L/2}^{L/2} J_z(z') dz' \int_{-\pi}^{\pi} \frac{\exp[ik\sqrt{4R_{cn}^2 \sin^2(\phi'/2) + (z-z')^2}]}{\sqrt{4R_{cn}^2 \sin^2(\phi'/2) + (z-z')^2}} d\phi' \\
&= \left(k^2 + \partial_z^2\right) \frac{iR_{cn}}{4\pi\epsilon_0\omega} \int_{-L/2}^{L/2} J_z(z') dz' \int_{-\pi}^{\pi} \frac{\exp[ik\sqrt{4R_{cn}^2 \sin^2(\phi'/2) + (z-z')^2}]}{\sqrt{4R_{cn}^2 \sin^2(\phi'/2) + (z-z')^2}} d\phi'
\end{aligned} \tag{4.66}$$

where we have made the substitution $(\Phi - \Phi') \to \phi'$. Here, we can define the scalar Hertz potential as

$$\Pi(z) = \frac{iR_{cn}}{4\pi\epsilon_0\omega} \int_{-L/2}^{L/2} J_z(z') dz' \int_{-\pi}^{\pi} \frac{\exp[ik\sqrt{4R_{cn}^2 \sin^2(\phi'/2) + (z-z')^2}]}{\sqrt{4R_{cn}^2 \sin^2(\phi'/2) + (z-z')^2}} d\phi' \tag{4.67}$$

so that

$$\frac{J(z)}{\sigma(\omega)} - E_z^{inc}(z) = \left(k^2 + \partial_z^2\right) \Pi(z) \tag{4.68}$$

This is an integro-differential equation that needs to be solved for the induced current. From Arfken and Weber pg. 598 (noting his definition of the Green's function being defined for $-\delta(z - z')$ so we get a negative sign for this Green's function), an equation of this form has a solution

$$\begin{aligned}
\left(k^2 + \partial_z^2\right) \psi(z) &= g(z) \\
\left(k^2 + \partial_z^2\right) F(z, z') &= \delta(z - z') \\
F(z, z') &= \frac{1}{2ik} e^{ik|z-z'|}
\end{aligned} \tag{4.69}$$

Therefore, the formal solution for the scalar Hertz potential is

$$\Pi(z) = C_1 e^{-ikz} + C_2 e^{ikz} + \frac{1}{2ik} \int_{-L/2}^{L/2} e^{ik|z-z'|} \left(\frac{J(z)}{\sigma(\omega)} - E_z^{inc}(z)\right) dz' \tag{4.70}$$

Combining Equations (4.67) and (4.70), we get

$$\frac{iR_{cn}}{4\pi\epsilon_0\omega}\int_{-L/2}^{L/2} J_z(z')dz' \int_{-\pi}^{\pi} \frac{\exp[ik\mathfrak{R}]}{\mathfrak{R}} d\phi' = C_1 e^{-ikz} + C_2 e^{ikz} + \frac{1}{2ik}\int_{-L/2}^{L/2} e^{ik|z-z'|}\left(\frac{J(z)}{\sigma(\omega)} - E_z^{inc}(z)\right) dz' \tag{4.71}$$

where $\mathfrak{R} = \sqrt{(z-z')^2 + 4R_{cn}^2 \sin^2(\phi'/2)}$. Rearranging, gives

$$C_1 e^{-ikz} + C_2 e^{ikz} + \int_{-L/2}^{L/2} \mathcal{K}(z-z')J(z')dz' = \frac{1}{2ik}\int_{-L/2}^{L/2} e^{ik|z-z'|} E_z^{inc}(z')dz' \tag{4.72}$$

where C_1 and C_2 are to be determined from the edge conditions and where the kernel $\mathcal{K}$ is given by

$$\mathcal{K}(z-z') = \frac{e^{ik|z-z'|}}{2ik\sigma} + \frac{R_{cn}}{4\pi\epsilon_0 i\omega}\int_{-\pi}^{\pi} \frac{\exp\left[ik\sqrt{(z-z')^2 + 4R_{cn}^2\sin^2(\phi'/2)}\right]}{\sqrt{(z-z')^2 + 4R_{cn}^2\sin^2(\phi'/2)}} d\phi' \tag{4.73}$$

4.3.2 Incident Field

For our excitation field, we use a plane wave given by

$$E_0^z = E_0 \cos(\theta) e^{i(kx\cos(\theta) - kz\sin(\theta))} \tag{4.74}$$

For the special case of perpendicular incidence where the field is polarized along the z-axis and travels along x, $\theta = 0$ and $E_0^z = E_0 e^{ikx}$.

The integral on the RHS of Equation (4.72) can be analytically solved for plane wave excitation. For the case of perpendicular incidence where $E_z^{inc}(z) = E_0$,

$$\frac{1}{2ik}\int_{-L/2}^{L/2} e^{ik|z-z'|} E_0 dz' = \frac{E_0}{k^2}\left(1 - e^{ikL/2}\cos(kz)\right) \tag{4.75}$$

For the case of an arbitrary incidence angle θ,

$$\begin{aligned}
&\frac{1}{2ik}\int_{-L/2}^{L/2} e^{ik|z-z'|}E_0\cos(\theta)e^{-ik\sin(\theta)}dz' = \\
&\frac{-E_0\sec(\theta)}{2k^2}e^{-ik(\sin(\theta)(L+4z)-L+4z)/2} \\
\times\quad &\left(\sin(\theta)\left(e^{ikz(2\sin(\theta)+1)} - e^{ik(\sin(\theta)(L+2z)+3z)}\right) + e^{ik(\sin(\theta)(L+2z)+3z)}\right. \\
&\left.-2e^{\frac{1}{2}ik(\sin(\theta)(L+2z)-L+4z)} + e^{ikz(2\sin(\theta)+1)}\right)
\end{aligned} \tag{4.76}$$

4.3.3 Solving by Quadrature

We have a Hallen type integral equation of the form

$$\int_{-L/2}^{L/2} \mathcal{Z}(z-z')J(z')dz' = C_1e^{-ikz} + C_2e^{ikz} + \int_{-L/2}^{L/2} F(z-z')E_z^{inc}(z')dz' \tag{4.77}$$

where we can define

$$\mathcal{Z}(z-z') = \frac{e^{ik|z-z'|}}{2ik\sigma} + \frac{R_{cn}}{4\pi\epsilon_0 i\omega}\int_{-\pi}^{\pi} \frac{\exp\left[ik\sqrt{(z-z')^2+4R_{cn}^2\sin^2(\phi/2)}\right]}{\sqrt{(z-z')^2+4R_{cn}^2\sin^2(\phi/2)}}d\phi \tag{4.78}$$

as the impedance kernel, and

$$F(z-z') = \frac{1}{2ik}e^{ik|z-z'|} \tag{4.79}$$

To numerically solve this equation for the current density J, we use a numerical quadrature method to transform this integral equation into a matrix equation [112]. First, we replace the current distribution and the incident field by their sampled versions, sampled at $N = 2M+1$ equally spaced points along the length:

$$J(z') = \sum_{m=-M}^{M} J(z_m)\delta(z'-z_m)\Delta z \tag{4.80}$$

and

$$E_z^{inc}(z') = \sum_{m=-M}^{M} E_z^{inc}(z_m)\delta(z'-z_m)\Delta z \tag{4.81}$$

where for $-M \leq m \leq M$,

$$z_m = m\Delta z, \quad \Delta z = \frac{L/2}{M} = \frac{L}{N-1} \tag{4.82}$$

The kernels $\mathcal{Z}(z-z')$ and $F(z-z')$ can be discretized, and this yields $N \times N$ matrices:

$$\begin{aligned} \mathcal{Z}_{nm} &= \mathcal{Z}(z_n - z_m)\Delta z = \Delta z \left(\frac{e^{ik\Delta z(n-m)}}{2ik\sigma} \right. \\ &\left. + \frac{R_{cn}}{4\pi i \epsilon_0 \omega} \int_{-\pi}^{\pi} \frac{\exp\left[ik\sqrt{\Delta z^2(n-m)^2 + 4R_{cn}^2 \sin^2(\phi/2)}\right]}{\sqrt{\Delta z^2(n-m)^2 + 4R_{cn}^2 \sin^2(\phi/2)}} d\phi \right) \end{aligned} \tag{4.83}$$

and

$$F_{nm} = F(z_n - z_m) = \frac{1}{2ik} e^{ik\Delta z|n-m|} \tag{4.84}$$

Now, we can express the discretized integral equation as

$$\sum_{m=-M}^{M} \mathcal{Z}_{nm} J_m = C_1 e^{-ikz_n} + C_2 e^{ikz_n} + \sum_{m=-M}^{M} F_{nm} E_m^{inc} \tag{4.85}$$

where we have denoted $E_m^{inc} = E^{inc}(z_m)$. This can be written in an even more compact form

$$\mathcal{Z}\mathbf{J} = C_1 \mathbf{s}_1 + C_2 \mathbf{s}_2 + F\mathbf{E}^{inc} \tag{4.86}$$

where $\mathbf{s}_1$ and $\mathbf{s}_2$ are vectors with elements $s_1(n) = e^{-ikz_n}$ and $s_2(n) = e^{ikz_n}$. We can define a $N \times 2$ matrix $S = [\mathbf{s}_1, \mathbf{s}_2]$ and the two dimensional vector of constants $\mathbf{C} = [C_1, C_2]^T$. With these definitions, the matrix equation becomes even more simplified

$$\mathcal{Z}\mathbf{J} = S\mathbf{C} + F\mathbf{E}^{inc} \tag{4.87}$$

The constants $\mathbf{C}$ must be found by imposing two separate edge conditions $J(z_M) = J(z_{-M}) = 0$. This boundary condition can be expressed compactly as

$$U^T \mathbf{J} = 0 \tag{4.88}$$

where $U = [\mathbf{u}_{top}, \mathbf{u}_{bot}]$ and $\mathbf{u}_{top} = [1, 0, \cdots, 0]^T$ selects the top entry of the vector $\mathbf{J}$ while $\mathbf{u}_{bot} = [0, \cdots, 0, 1]^T$ selects the bottom entry. We can now solve the matrix

equation for the current density $\mathbf{J}$

$$\mathbf{J} = \mathcal{Z}^{-1} S\mathbf{C} + \mathcal{Z}^{-1} F\mathbf{E}^{inc} \tag{4.89}$$

If we multiply from the left by U^T, we obtain the condition

$$U^T\mathbf{J} = U^T\mathcal{Z}^{-1} S\mathbf{C} + U^T\mathcal{Z}^{-1} F\mathbf{E}^{inc} = 0 \tag{4.90}$$

which can be solved for the coefficients

$$\mathbf{C} = -\left(U^T\mathcal{Z}^{-1}S\right)^{-1}\left(U^T Z^{-1} F\right)\mathbf{E}^{inc} \tag{4.91}$$

Equation (4.91) is used to calculate the coefficients that satisfy the edge conditions. Once these are calculated, Equation (4.89) can be solved for the current density. Note that the current density J is related to the linear current I by the relation

$$I(z) = \frac{J(z)}{2\pi R} \tag{4.92}$$

4.3.4 Handling the Singularity in $\mathcal{Z}_{nm}$

We begin by separating the kernel

$$\frac{e^{ik|\mathbf{r}-\mathbf{r}'|}}{|\mathbf{r}-\mathbf{r}'|} = \frac{1}{|\mathbf{r}-\mathbf{r}'|} + \frac{e^{ik|\mathbf{r}-\mathbf{r}'|}-1}{|\mathbf{r}-\mathbf{r}'|} \tag{4.93}$$

Now, we can analytically integrate the first term with the singularity around ϕ

$$\int_{-\pi}^{\pi} \frac{d\phi'}{|\mathbf{r}-\mathbf{r}'|} = \int_{-\pi}^{\pi} \frac{d\phi'}{\sqrt{4R_{cn}^2\sin^2(\phi'/2)+(z-z')^2}} = \frac{4\mathcal{K}\left[4R_{cn}^2/(4R_{cn}^2+(z-z')^2)\right]}{\sqrt{4R_{cn}^2+(z-z')^2}} \tag{4.94}$$

where $\mathcal{K}[x]$ is the elliptic integral of the first kind. Note that this term still has a logarithmic singularity at $(z-z')=0$. However, this logarithmic singularity is integrable. The second term in the separated kernel is calculated numerically with no issues since it is a slowly varying function with no singularities.

Performing our quadrature technique to this elliptic integral term will still give $-\infty$ when $n = m$ in the impedance matrix. However, since the singularity is integrable, we can replace the $n = m$ term in the matrix with

$$\mathcal{Z}_0 = \int_{-1}^{1} \frac{4\mathcal{K}\left[4R_{cn}^2/(4R_{cn}^2 + \Delta z^2(x)^2)\right]}{\sqrt{4R_{cn}^2 + \Delta z^2(x)^2}} dx \tag{4.95}$$

where x is a dummy index representing the singular part between $n = m - 1$ and $n = m + 1$. We are integrating over the singularity to obtain a value for the $n = m$ impedance matrix element. The full impedance kernel now reads

$$\begin{aligned} \mathcal{Z}_{nm} &= \Delta z \left[\frac{e^{ik\Delta z(n-m)}}{2ik\sigma} + \frac{R_{cn}}{4\pi i\epsilon_0\omega} \left(\frac{4\mathcal{K}\left[4R_{cn}^2/(4R_{cn}^2 + \Delta z^2(n-m)^2)\right]}{\sqrt{4R_{cn}^2 + \Delta z^2(n-m)^2}} \right.\right. \\ &\quad \left.\left. + \int \frac{\exp(ik\sqrt{4R_{cn}^2\sin^2(\phi'/2) + \Delta z^2(n-m)^2}) - 1}{\sqrt{4R_{cn}^2\sin^2(\phi'/2) + \Delta z^2(n-m)^2}} d\phi' \right) \right] \end{aligned} \tag{4.96}$$

for when $n \neq m$ and

$$\begin{aligned} \mathcal{Z}_{00} &= \Delta z \left[\frac{1}{2ik\sigma} + \frac{R_{cn}}{4\pi i\epsilon_0\omega} \left(\int_{-1}^{1} \frac{4\mathcal{K}\left[4R_{cn}^2/(4R_{cn}^2 + \Delta z^2(x)^2)\right]}{\sqrt{4R_{cn}^2 + \Delta z^2(x)^2}} dx \right.\right. \\ &\quad \left.\left. + \int \frac{\exp(ik\sqrt{4R_{cn}^2\sin^2(\phi'/2)}) - 1}{\sqrt{4R_{cn}^2\sin^2(\phi'/2)}} d\phi' \right) \right] \end{aligned} \tag{4.97}$$

when $n = m$.

4.3.5 PL Enhancement

The PL rate of a two-level molecule can be expressed as [126]

$$\gamma_{PL} = \gamma_{exc}\left(\frac{\gamma_r}{\gamma}\right) \tag{4.98}$$

where γ_{exc} is the rate of excitation, γ_r is the radiative decay rate, and $\gamma = \gamma_r + \gamma_{nr}$ is the total decay rate of the molecule. Radiative losses should be negligable for REIs. However, other non-radiative mechanisms not associated with the SWNT

may play a signficant role. In that case, the total decay rate of the REI would then be $\gamma = \gamma_r + \gamma_{nr} + \gamma_{other}$. In our system, we assume that the only non-radiative decay channel of the REI is due to dissipative losses. Therefore,

$$\gamma_{nr} = \frac{1}{2} \int \mathrm{Re}\left[\mathbf{E}^*(\mathbf{x}) \cdot \mathbf{j}(\mathbf{x}) d\mathbf{x}\right] \tag{4.99}$$

where $\mathbf{E}^*(\mathbf{x})$ is the conjugate of the total electric field and $\mathbf{j}(\mathbf{x})$ is the current density. Without any objects in the environment, the molecule is simply excited by the external field E_0. Having the NT antenna in the vicinity generates an additional field which interacts with the molecule. Therefore, the excitation rate is proportional to the ratio of the total field intensity (incident plus scattered field) to the incident field intensity:

$$\gamma_{exc} = \left| \frac{\mathbf{E}(\mathbf{r}_0)}{\mathbf{E}_0(\mathbf{r}_0)} \right|^2 \tag{4.100}$$

where $\mathbf{r}_0$ is the position of the REI.

4.4 REI Excitation Enhancements

Figure 4.1 shows the fitted excitonic conductivity for a (6,5) semiconducting SWNT including the S_1 and S_2 transitions. The parameters used for the conductivity fitting are shown in Table 4.1. The S_1 transition has a maximum conductivity of approximately $7G_0$, where $G_0 = e^2/h$ is the quantum of conductance. This value fits within the range of values calculated for many other SWNTs using quantum mechanical calculations [117].

Figure 4.2 shows the calculated linear current for a 50 nm long (6,5) SWNT excited at perpendicular incidence at the ${}^5D_0 \rightarrow {}^7F_0$ Eu^{3+} transition at 2.14 eV. In the center of the SWNT, the current distribution is flat due to the external field having no spatial variance along the tube at perpendicular incidence ($E_z^{xt}(z) = E_0$).

Figure 4.3 shows a density plot of the normalized scattered field from Equation (4.63) as a function of distance away from the SWNT surface. The hotspots are located around the tube edges. The field enhancements decay as you move farther away and virtually disappear at a distance of 5 nm. This shows that these hotspots

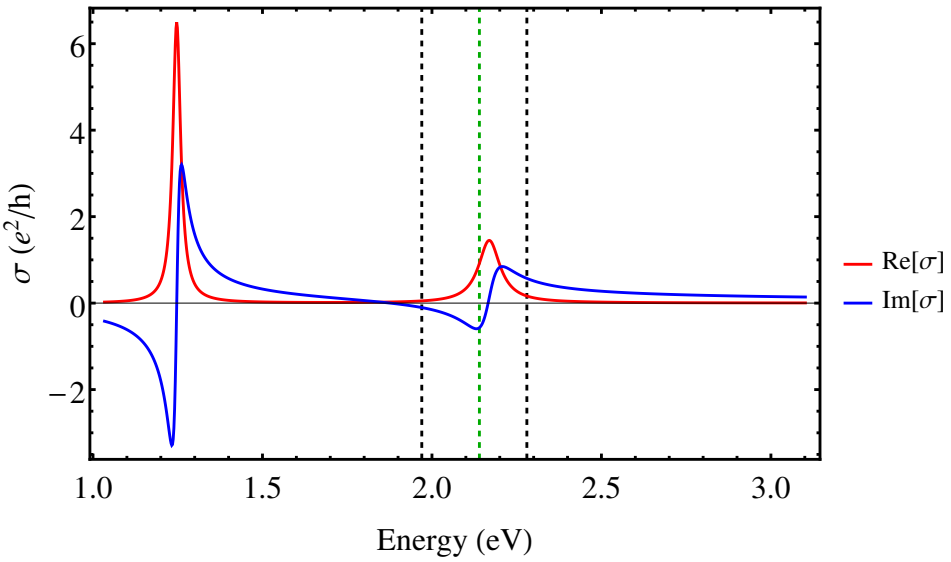

Figure 4.1: Fitted exciton conductivity for (6,5) semiconducting SWNT using Equation (4.16) with experimental parameters.[6, 7] The black dashed lines indicate range of REI transitions overlapping with the S_2 level of the (6,5) SWNT. The green dashed line corresponds to the ${}^5D_0 \rightarrow {}^7F_0$ Eu^{3+} transition at 2.14 eV.

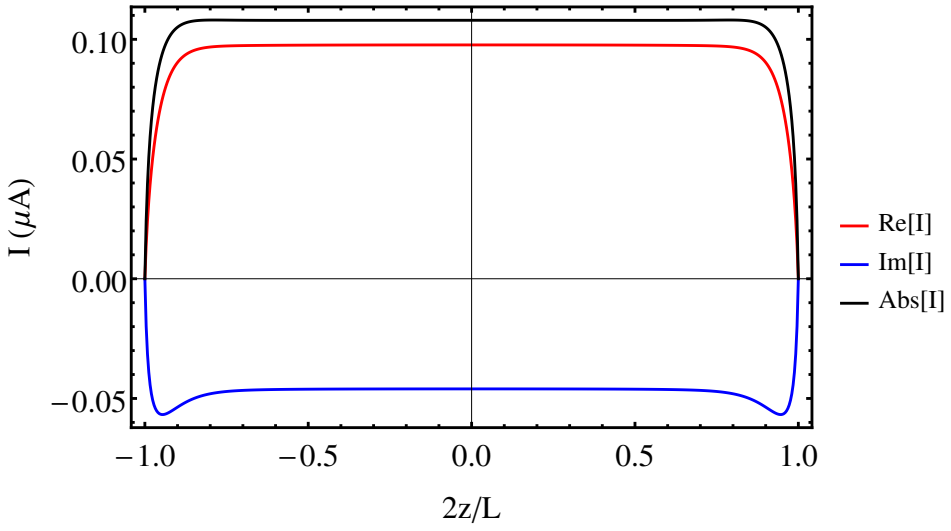

Figure 4.2: Calculated linear current for $L = 50$ nm (6,5) semiconducting SWNT resonant with the ${}^5D_0 \rightarrow {}^7F_0$ Eu^{3+} transition at 2.14 eV with the external field perpendicularly incident ($\theta = 0°$).

(n,m)	S_1 (eV) $^{(a)}$	f_1 $^{(b)}$	γ_1 (meV)	S_2 (eV) $^{(a)}$	f_2 $^{(b)}$	γ_2 (meV)
(6,5)	1.25	0.01	27.3	2.17	0.0061	76.9
(7,5)	1.19	0.0064	20.8	1.91	0.0058	66.6
(7,6)	1.09	0.008	19.4	1.90	0.0047	64.1
(8,6)	1.04	0.0054	19.1	1.72	0.0049	55.4
(8,7)	0.96	0.0065	17.8	1.68	0.0036	45.9

Table 4.1: Experimentally measured parameters used for the fitting of the exciton conductivity.
(a) from [6].
(b) from [7].

are extremely localized to the near field around the antenna. Figure 4.4 shows the scattered electric fields around the edge of the SWNT. From the red line in Figure 4.5, it can be seen that the main contribution for this field enhancement comes from the radial (x) component of the scattered field which can also be verified from Figure 4.4. For REI/SWNT complexes, it was experimentally measured that the Förster distance in solution was approximately 1 nm from the SWNT surface [6, 127]. Therefore, when forming complexes, REIs are in very close proximity to the SWNT and will be experiencing these field enhancements.

Figure 4.6 shows the total normalized field (incident plus scattered). This shows an area just prior to the tube ends where the total field magnitude is less than the incident field. The cross section of this field at 1 nm can be seen in Figure 4.7. This is due to the z-component of the scattered field. Because the magnitude of $E_z^{sc} + E_z^{inc}$ is larger than E_x^{sc}, the total field mostly follows the dependence of the z-component of the scattered field. This means that for a REI sitting in the vicinity of the tube edge, depending on where along the tube it is, it could either see an enhanced field or a diminished field which leads to an enhancement of PL emission or a decrease of PL emission, respectively. Figure 4.7 shows the cross section of the total field 1 nm away from the SWNT surface.

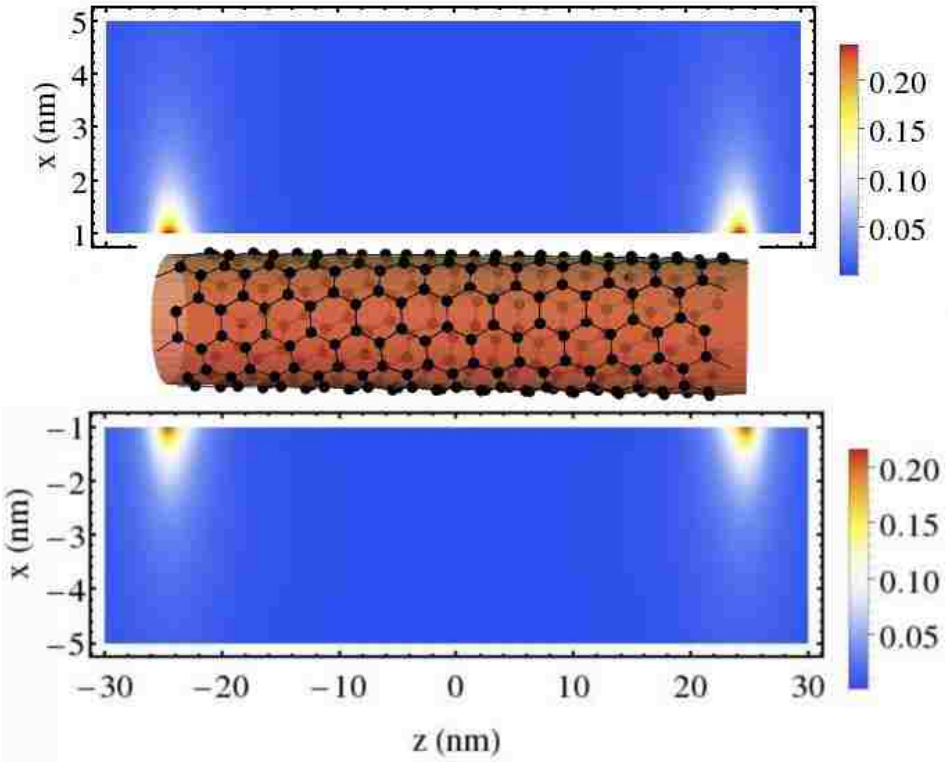

Figure 4.3: Density plot of the normalized scattered field of a 50 nm long (6,5) SWNT at the ${}^5D_0 \rightarrow {}^7F_0$ Eu^{3+} transition at 2.14 eV as a function of distance away from the SWNT surface. Note that the SWNT lattice is not to scale.

Figure 4.8 shows the integrated total field,

$$\int_{-L/2}^{L/2} \left(\left(\frac{E_{tot}(z)}{E_0} \right)^2 - 1 \right) dz \tag{4.101}$$

as a function of energy where we have integrated over the length of the SWNT. The black, dashed lines indicate the S_1 and S_2 peaks. If we were to assume uniform coverage of the SWNT by REIs, this can give us a good estimate of the quantum yield due to the SWNT we should expect. The S_1 resonance shows the best average difference in enhancement. The average enhancements around the S_2 peak do not show as strong enhancements as around the S_1.

Once the field enhancements are calculated, we can then proceed to calculate

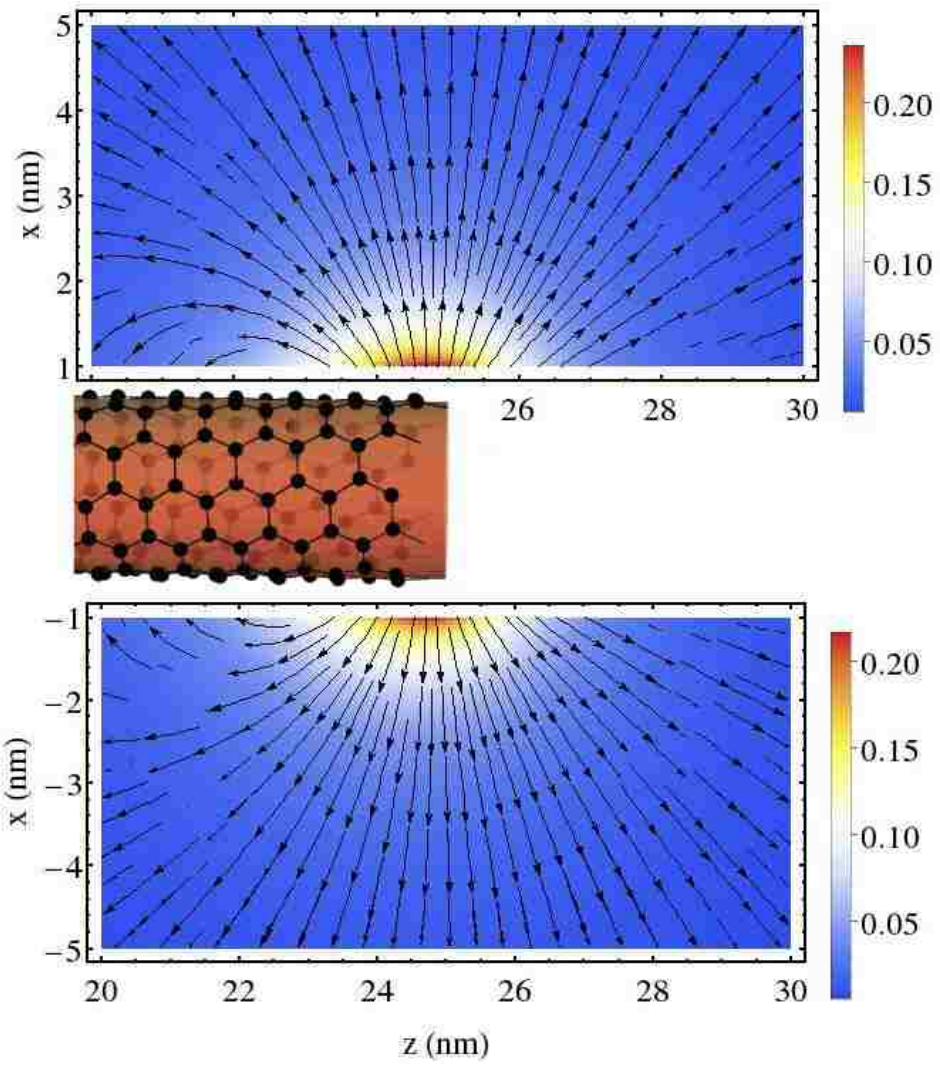

Figure 4.4: Vector density plot of the normalized scattered field of a 50 nm long (6,5) SWNT at the ${}^5D_0 \rightarrow {}^7F_0$ Eu^{3+} transition at 2.14 eV showing the electric field lines at the edge of the SWNT.

the excitation enhancement of the REIs from Equation (4.100). These calculations were done not only for one particular SWNT and one particular REI transition: we calculated excitation enhancements for the five most predominant chiralities of SWNTs found in solution with a range of REI transitions that overlap with the S_1 and S_2 transitions. The results for the S_2 resonances can be seen in Figure 4.9. We

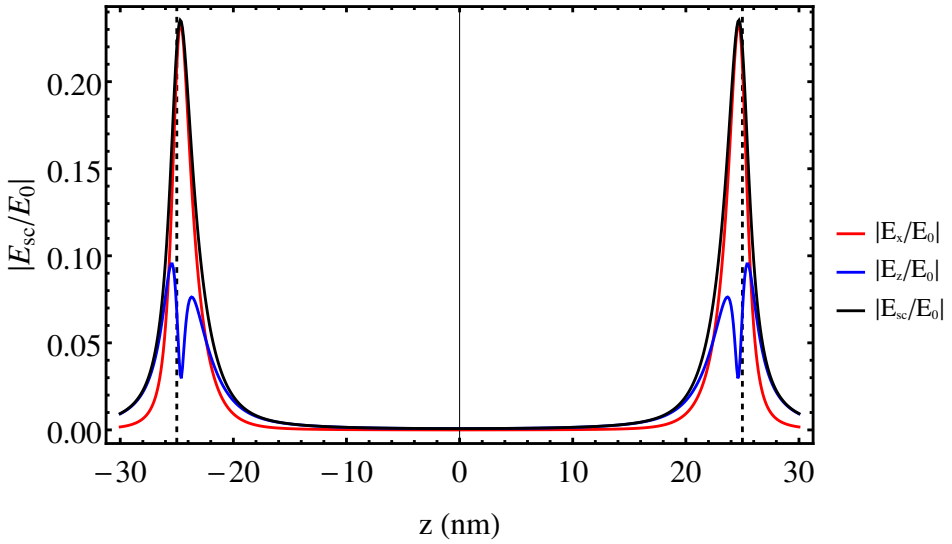

Figure 4.5: Cross section of the normalized scattered fields in Figure 4.3. The cross section is taken at a distance of 1 nm away from the surface of the SWNT. The red line is the magnitude of the radial field, the blue line is the magnitude of the axial field, and the black line is the magnitude of the total scattered field. The antenna edges are shown by the vertical, dashed, black lines.

calculate the percentage excitation enhancement (calculated excitation enhancement normalized by the excitation rate in the external field alone) for the REIs sitting in the location of maximum enhancement of Figure 4.6. We obtain a wide range of values for different chiralities and transitions. We can see maximum excitation enhancements of approximately 40% for the ${}^6F_{1/2} \rightarrow {}^6H_{15/2}$ Dy^{3+} transition with the (8,6) and (8,7) SWNTs.

The results for the S_1 enhancements can be seen in Figure 4.10. The magnitudes of the currents are larger around the S_1 resonances so they scatter a stronger electric field leading to larger local enhancements. Excitation enhancements of over 200% can be seen for certain REI transitions.

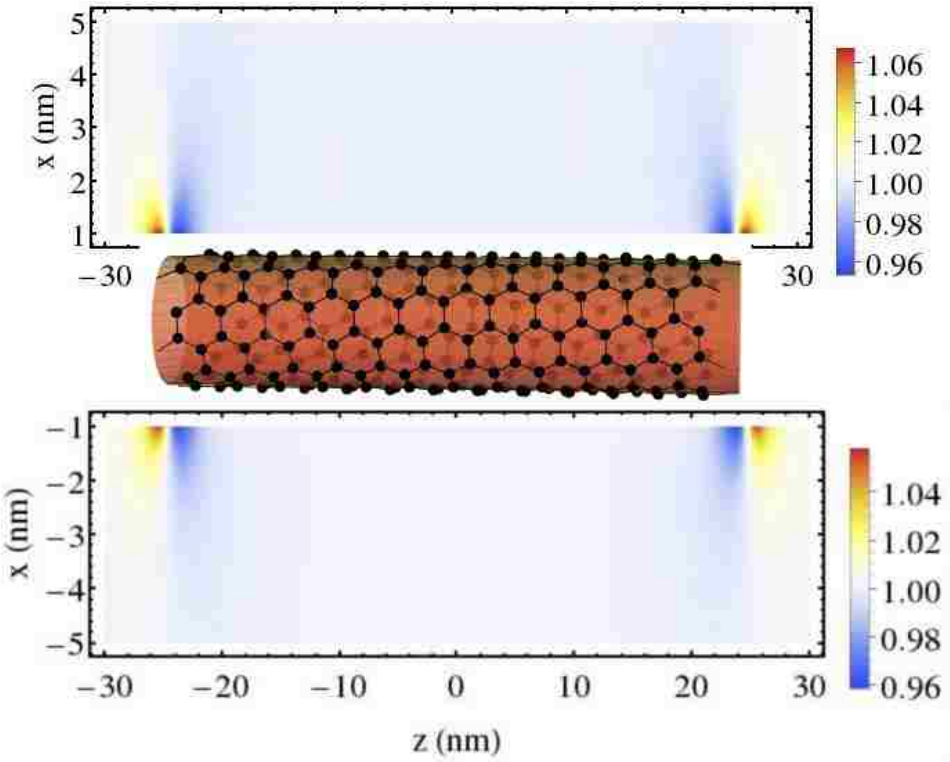

Figure 4.6: Density plot of the normalized total (incident plus scattered) field of a 50 nm long (6,5) SWNT at the ${}^5D_0 \rightarrow {}^7F_0$ Eu^{3+} transition at 2.14 eV as a function of distance away from the SWNT surface. Note that the SWNT is not to scale.

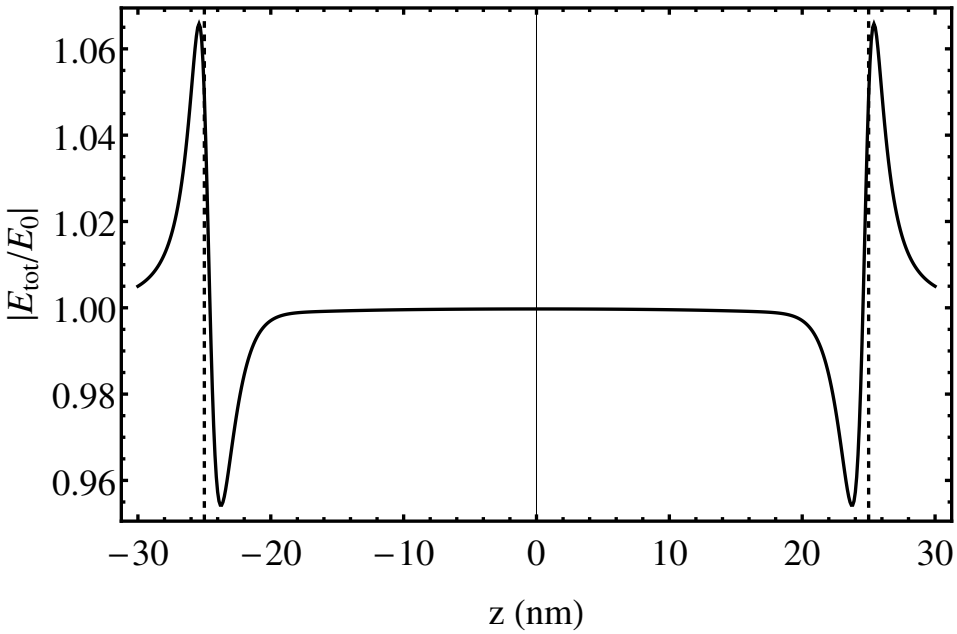

Figure 4.7: Cross section of the normalized total (incident plus scattered) field of Figure 4.6 taken at 1 nm away from the surface of the SWNT.

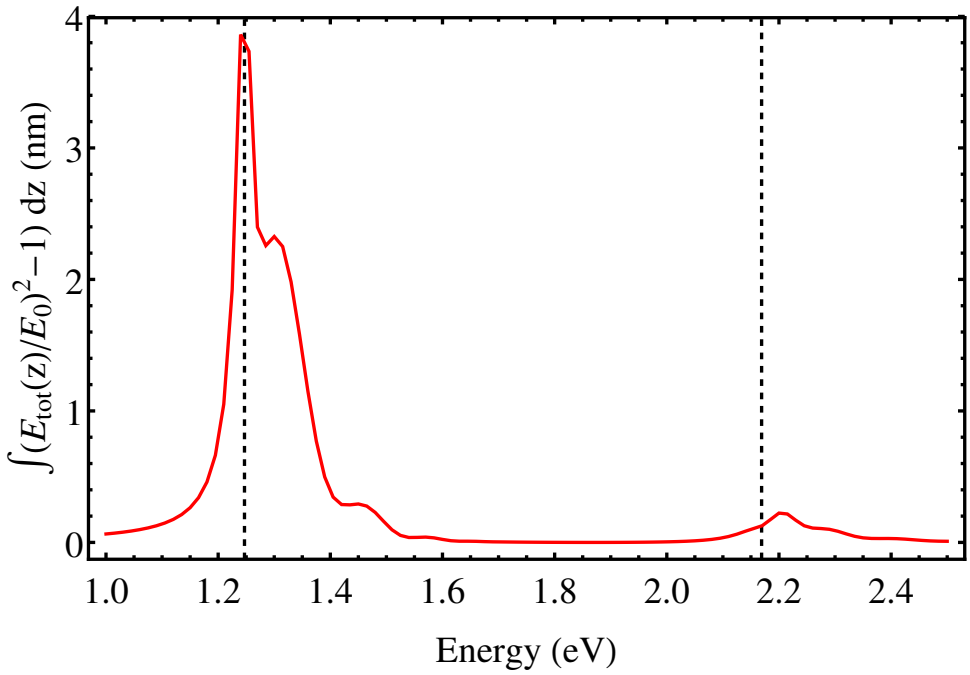

Figure 4.8: Total integrated field intensity 1 nm away from (6,5) SWNT surface integrated along the SWNT as a function of energy ranging from below S_1 (left dashed line) to above S_2 (right dashed line).

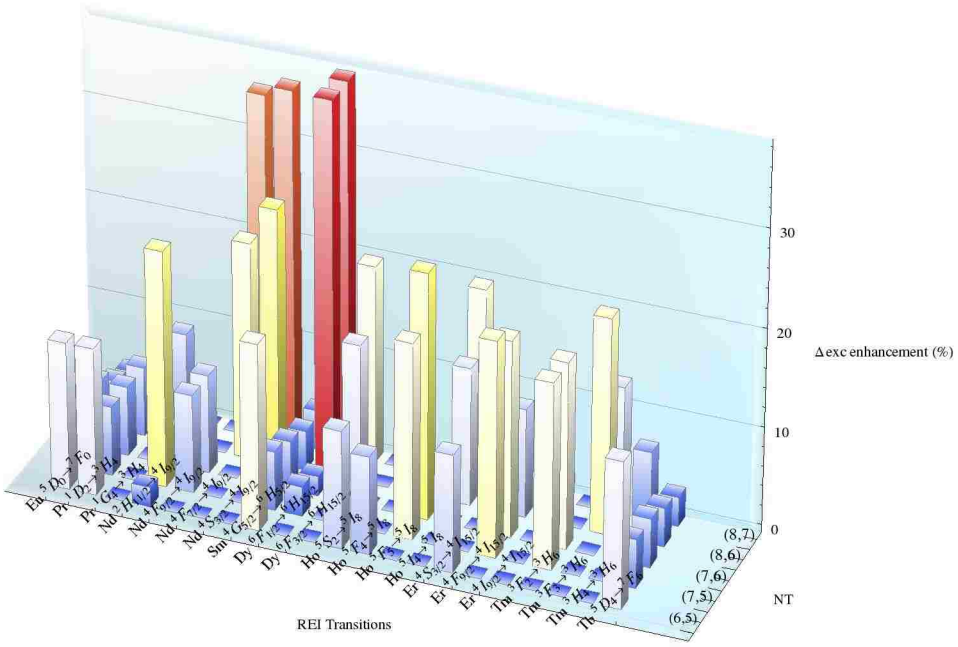

Figure 4.9: Calculated percentage excitation enhancements of multiple REI transitions with various S_2 transitions of predominant SWNT chiralities.

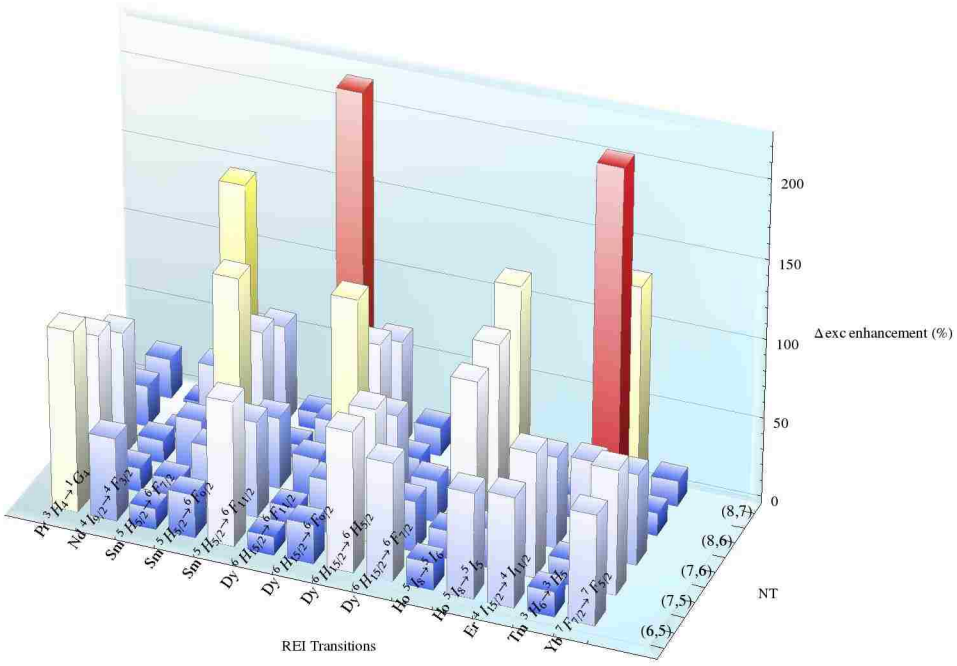

Figure 4.10: Calculated percentage excitation enhancements of multiple REI transitions with various S_1 transitions of predominant SWNT chiralities.

4.5 Oscillatory Patterns

Figure 4.11 shows the conductivity in units of the conductance quantum around the S_1 transition of the (6,5) SWNT. The dashed vertical lines indicate particular frequencies used to evaluate the current distribution. The frequencies were chosen to be symmetric about the S_1 conductivity peak. Figures 4.12, 4.13, and 4.14 show the calculated current distributions at the frequencies indicated in Figure 4.11 with the color coding remaining the same. The maximum currents are observed to be at the S_1 transition as we should expect due to the conductivity being a maximum there. However, different behavior is seen below the resonance than above the resonance. Below S_1, the current distributions are flat and show no features. Approaching S_1, the currents increase in magnitude, but also begin to show some structure. On resonance, a dip can be seen in the middle of the tube. Above resonance, definite oscillatory patterns appear. As we get further away from the resonance, the amplitude decreases and the wavelength of oscillations becomes smaller.

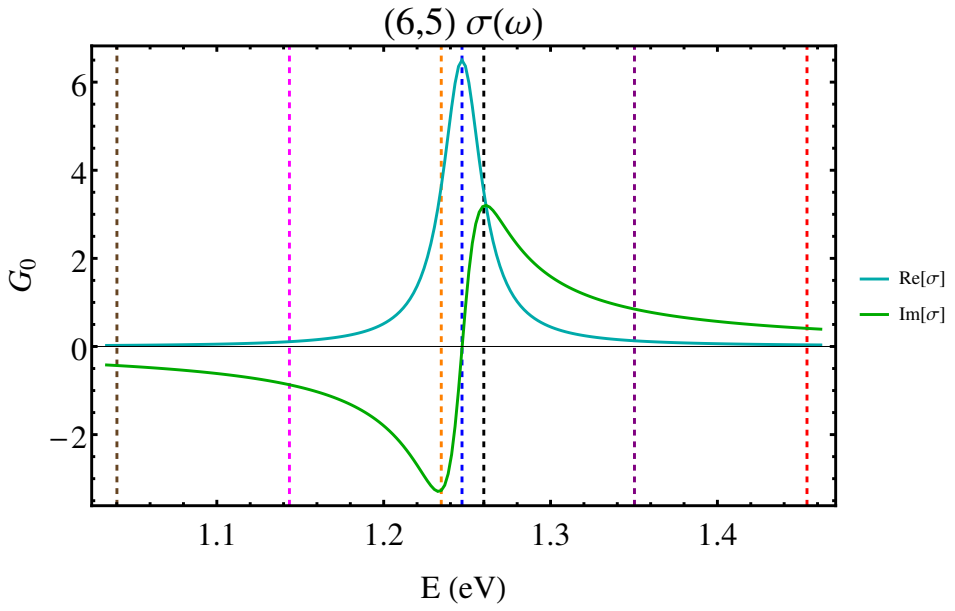

Figure 4.11: Real and imaginary parts of the (6,5) conductivity with the energies (frequencies) used in the current calculations.

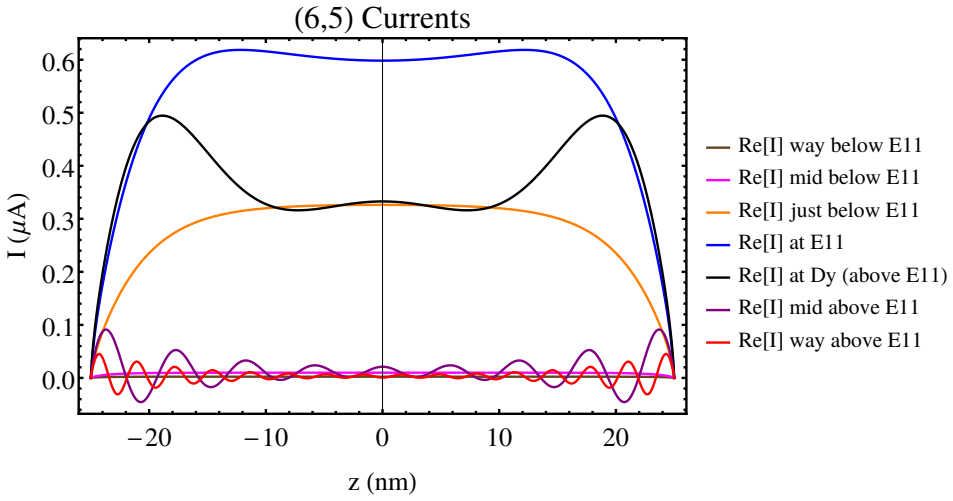

Figure 4.12: Calculated real part of the current at the frequencies indicated on Figure 4.11. The maximum current is obtained when on resonance with the E11 transition.

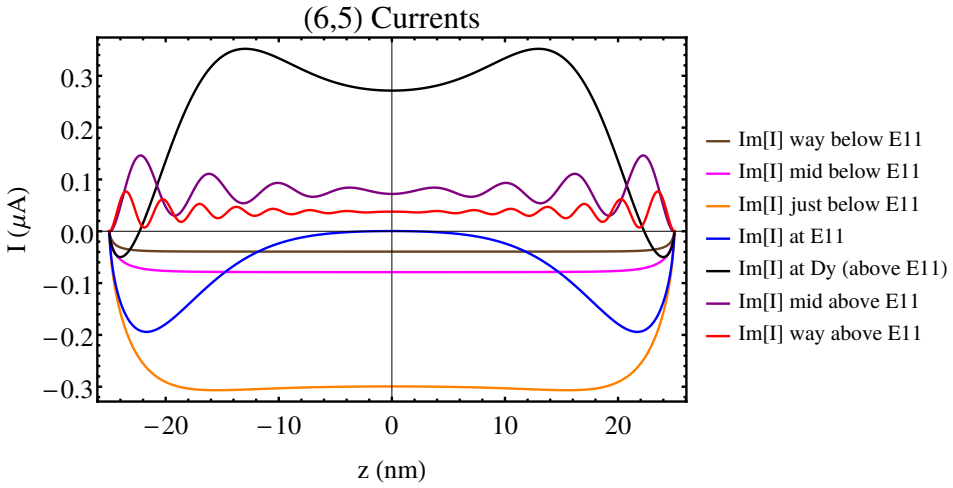

Figure 4.13: Calculated imaginary part of the current at the frequencies indicated on Figure 4.11.

These oscillations occur above the S_2 transition as well. The transitions between non-oscillatory and oscillatory currents above and below both resonances can be seen in Figure 4.15.

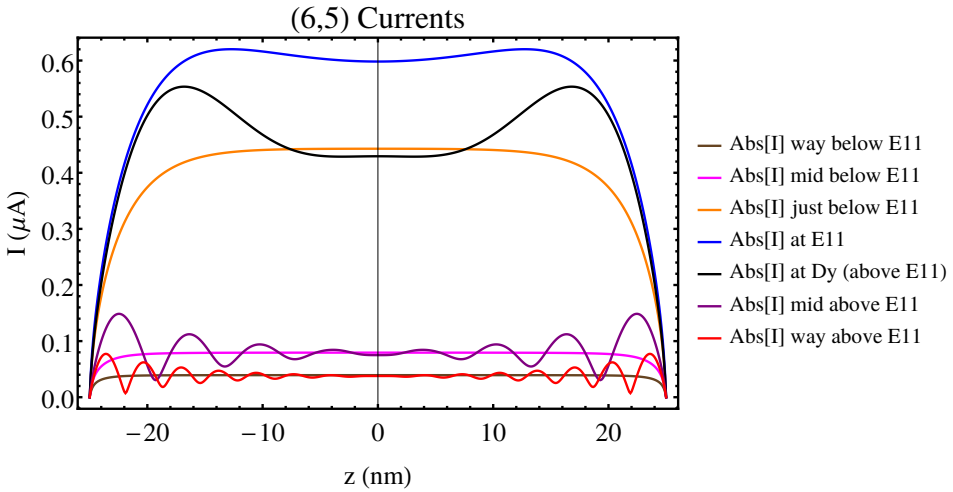

Figure 4.14: Calculated magnitudes of the currents at the frequencies indicated on Figure 4.11.

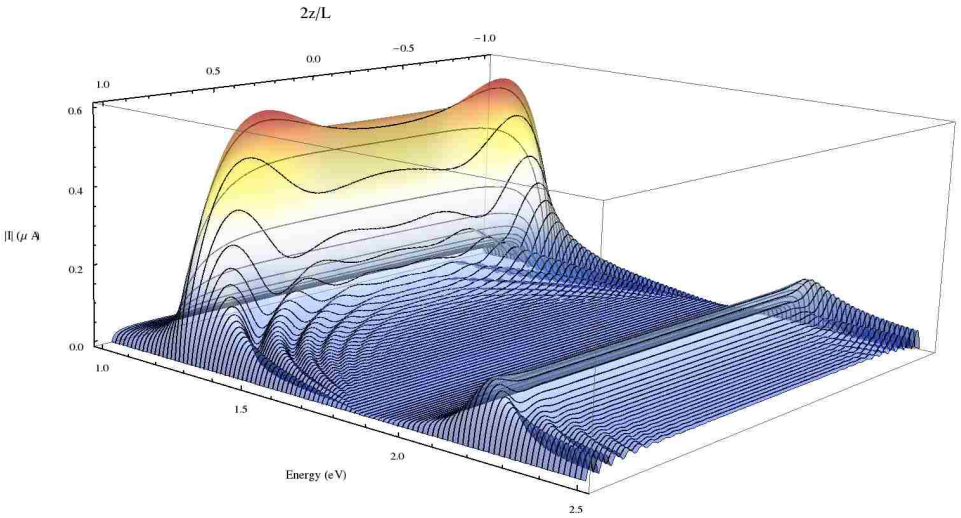

Figure 4.15: Surface plot of calculated current distributions over a frequency range covering the S_1 and S_2 transitions of the (6,5) SWNT. The continuous transition between non-oscillatory and oscillatory currents when passing over the exciton resonances can be seen.

To understand how material parameters change these oscillatory patterns, we chose a frequency that exhibits oscillatory behavior at 1.3 eV. We then calculated

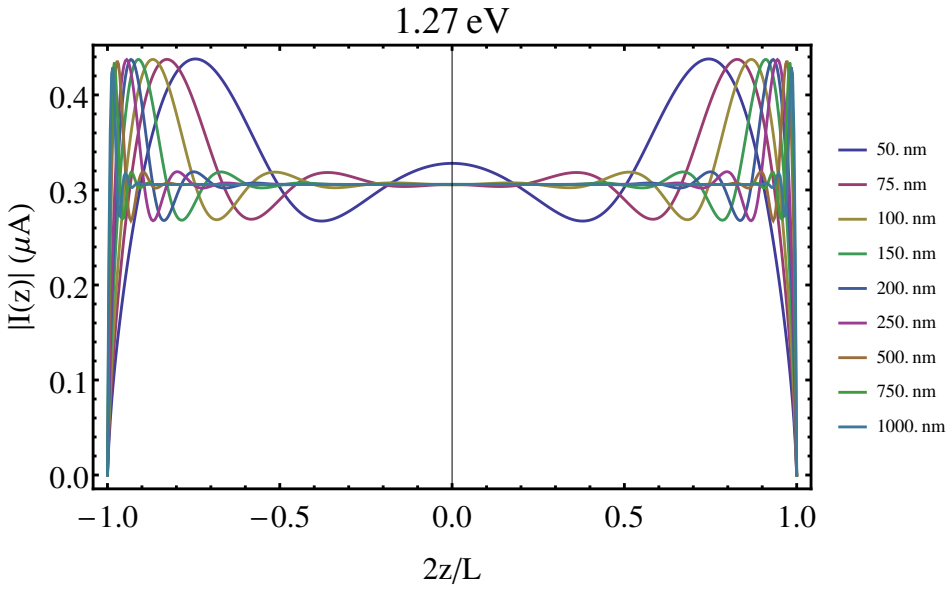

Figure 4.16: Oscillatory current calculated at 1.27 eV as a function of length of SWNT. As the length is increased, so is the wavelength of oscillations.

the current distribution at this frequency as a function of SWNT length. The results can be seen in Figure 4.16. As L is increased, the wavelength of oscillations decreases. Figure 4.17 shows a fit of the measured wave vector, k, as a function of the length. The data was fitted with a power law and the fit shows an exact dependence of L^{-1}.

To analyze the observed oscillatory behavior when passing over a resonance, we fit the calculated current distributions with a function

$$A + Be^{i\mathcal{K}z} \tag{4.102}$$

where A and B are complex parameters and $\mathcal{K} = k + i\kappa$ is the complex wave vector accounting for the oscillatory behavior (real component) and the damping (imaginary component). Figure 4.18 shows the fitted values of the real component of the complex wave vector as a function of frequency at an energy range just after the S_1 where the oscillatory behavior begins. Deviations from a linear dependence is observed. When the value of k passes an odd multiple of π/L, the line flattens for a moment before continuing to the next odd multiple of π/L.

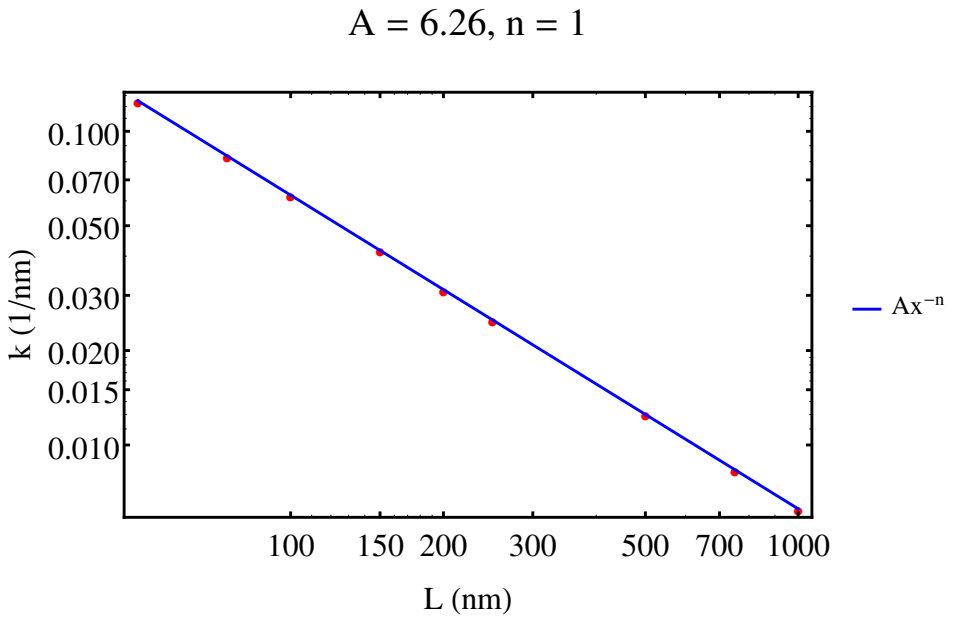

Figure 4.17: Fit of the wave vector as a function of length for the oscillations in Figure 4.16. The fit shows a $1/L$ fit showing that k is inversely proportional to the length.

Figure 4.19 shows the fitted values of the imaginary component of the complex wave vector as a function of frequency. Two distinct behaviors can be observed. The first is the overall trend which shows that the damping is higher when we are close to the S_1 resonance, and κ decreases as we go further away. The second trend is the oscillatory behavior. The local minima that are observed in the oscillations correspond to the positions where k crosses multiples of π/L. The local maxima positions are when k is between multiples. When k lies on an odd multiple of π/L, the damping is smaller than when k is not an odd multiple of π/L. This behavior can be more easily seen in Figure 4.20.

From this Figure 4.18, a linear fit can be made to extract the slope which by definition is the inverse of the group velocity: $v_g = \partial\omega/\partial k$. From the fit, we calculate a group velocity of $0.175v_F$, where $v_F = 1$ nm/fs is the Fermi velocity of carbon materials. The Fermi velocity is approximately 300 times smaller than the speed of light in vacuum. More analysis is required to explain why the group velocity is only

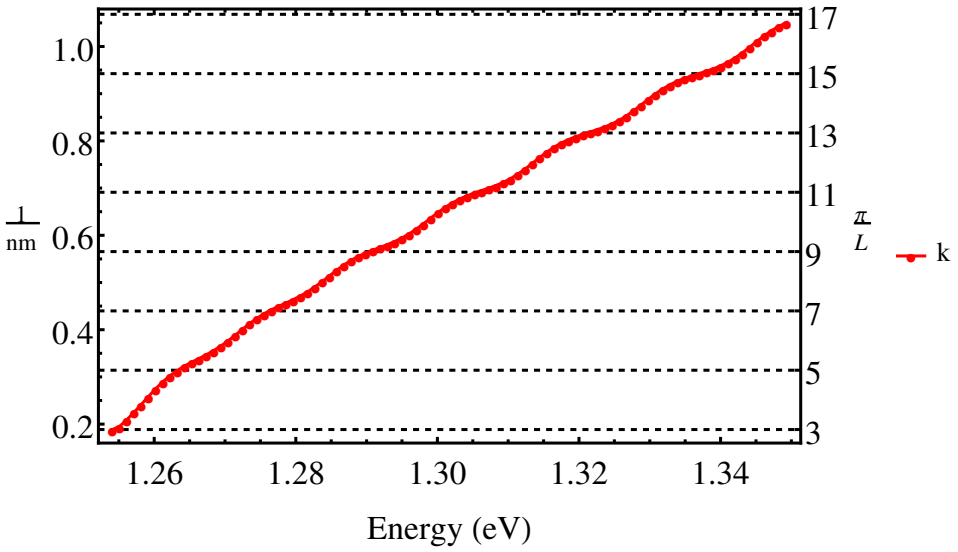

Figure 4.18: Fitted values of the real component of the complex wave vector of oscillations as a function of energy.

a fraction of the Fermi velocity.

The behavior of the system in the complex plane can be observed by making an Argand plot. We fit the k dependence on energy from Figure 4.18 and subtracted that linear dependence to form a new variable which we denoted as k'. That value is plotted along the real axis while κ is plotted along the imaginary axis. The third axis is energy. This 3D Argand plot can be seen in Figure 4.21. Spirals can be observed from the plot which illustrate the phase behavior of the system. Between the energies where k crosses odd multiples of π/L, the system goes through a phase change of 2π which is shown from the spirals of the Argand plot.

We also wanted to calculate the dependence of these oscillations on the width of the excitonic transition, γ. To do this, we increased the quality factor, or Q factor, of the transitions. The quality factor is defined as the frequency of the transition divided by the full width at half maximum (FWHM) of the transition. We chose an arbitrarily high Q factor of 1000 to compare our results. The resulting excitonic conductivity can be seen in Figure 4.22. The transition lines are now very sharp and

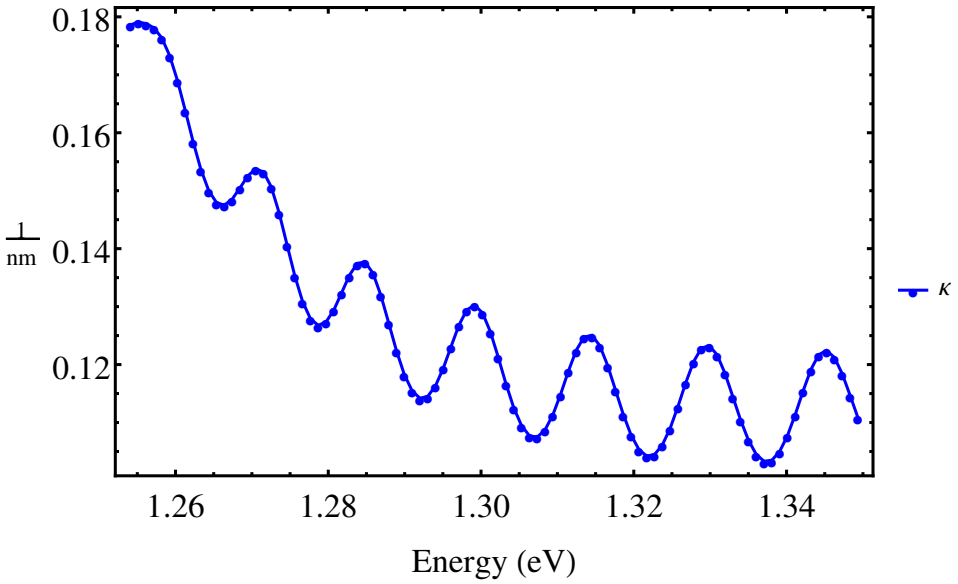

Figure 4.19: Fitted values of the imaginary component of the complex wave vector of oscillations as a function of energy.

their magnitudes are almost two orders of magnitude higher than they were when using the experimental values.

We then fitted the currents calculated with the increased quality factor and the results for the fitted values of k and κ can be seen in Figure 4.23. A striking difference in the behavior as compared Figure 4.20 can be seen. Now, k plateaus on the odd multiples of π/L for an extended energy range. Again, the local minima of κ occur when k is a multiple of π/L and the local maxima are when k is transitioning between the multiples. This is now showing us evidence that what we are calculating are polaritonic modes. The exciton line is crossing the antenna resonance line, creating an exciton polariton.

We also calculated the effect of the exciton conductivity on the current oscillations. Figure 4.24 shows the calculated real part of the (6,5) current distribution at 1.35 eV (this corresponds to the purple dashed line in Figure 4.11). By independently changing the real and imaginary components of the conductivity, we see that the oscillations with the least amount of damping occur when Im$[\sigma]$ is higher.

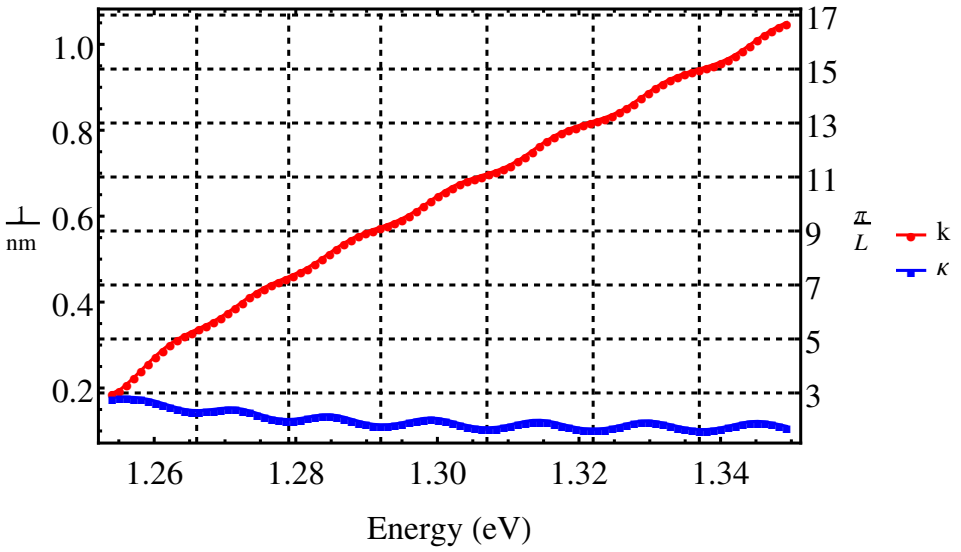

Figure 4.20: Fitted values of both the real and imaginary component of the complex wave vector as a function of energy.

This agrees with the increased Q factor data. By increasing the Q value, we have increased the imaginary component of the conductivity and we observe oscillations with lower damping. By decreasing the imaginary component of the conductivity, we increase the damping in our system.

The behavior of this system also exhibits behavior seen in non-Hermitian Hamiltonians. For a discrete, two level quantum system with non-vanishing interaction strength, we observe anti-crossing of the two levels as can be seen in Figure 4.25. The two levels without interaction are shown as the black, dashed lines. Due to their interaction, the two levels repel one another. However, when the Hamiltonian has complex energies,

$$\mathrm{H} = \begin{pmatrix} \varepsilon_1 - i\gamma_1 & g \\ g & \varepsilon_2 - i\gamma_2 \end{pmatrix} = \begin{pmatrix} e_1 & g \\ g & e_2 \end{pmatrix} \tag{4.103}$$

where ε_1 and ε_2 are the energies of the two levels, γ_1 and γ_2 are the widths of the two levels, and g is the interaction strength, the eigenvalues of the Hamiltonian become

complex:

$$E_i - i\Gamma_i = \frac{e_1 - e_2}{2} \pm \frac{1}{2}\sqrt{(e_1 - e_2)^2 + 4g^2} \tag{4.104}$$

where the real part of the eigenvalue gives the energies while the imaginary part gives the widths.

When γ is small, the levels exhibit anti-crossing similar to the case where $\gamma = 0$. This can be seen in Figure 4.26 for the energy and in Figure 4.27 for the widths. However, when γ becomes significant, the levels begin to cross as can be seen in Figures 4.28 and 4.29. The energy levels now allowed to cross at a point.

Further evidence that we are calculating exciton-polaritonic modes can be extracted from properties of phonon-polaritons. It is a known property of phonon polaritons that they can only exist in a certain region known as the Reststrahlen band [128, 129, 130]. The Reststrahlen band is defined as the region where the real part of the complex dielectric function, Re[ϵ]< 0. Outside of that region, phonon-polaritons are not allowed to propagate. In our system, the Reststrahlen band is the region following the S_1 and S_2 transitions. Outside of that range, we observe featureless current distributions. However, inside of that region where the real part of our dielectric function is negative, we observe these polaritonic modes which follow a π/L wavevector dependence.

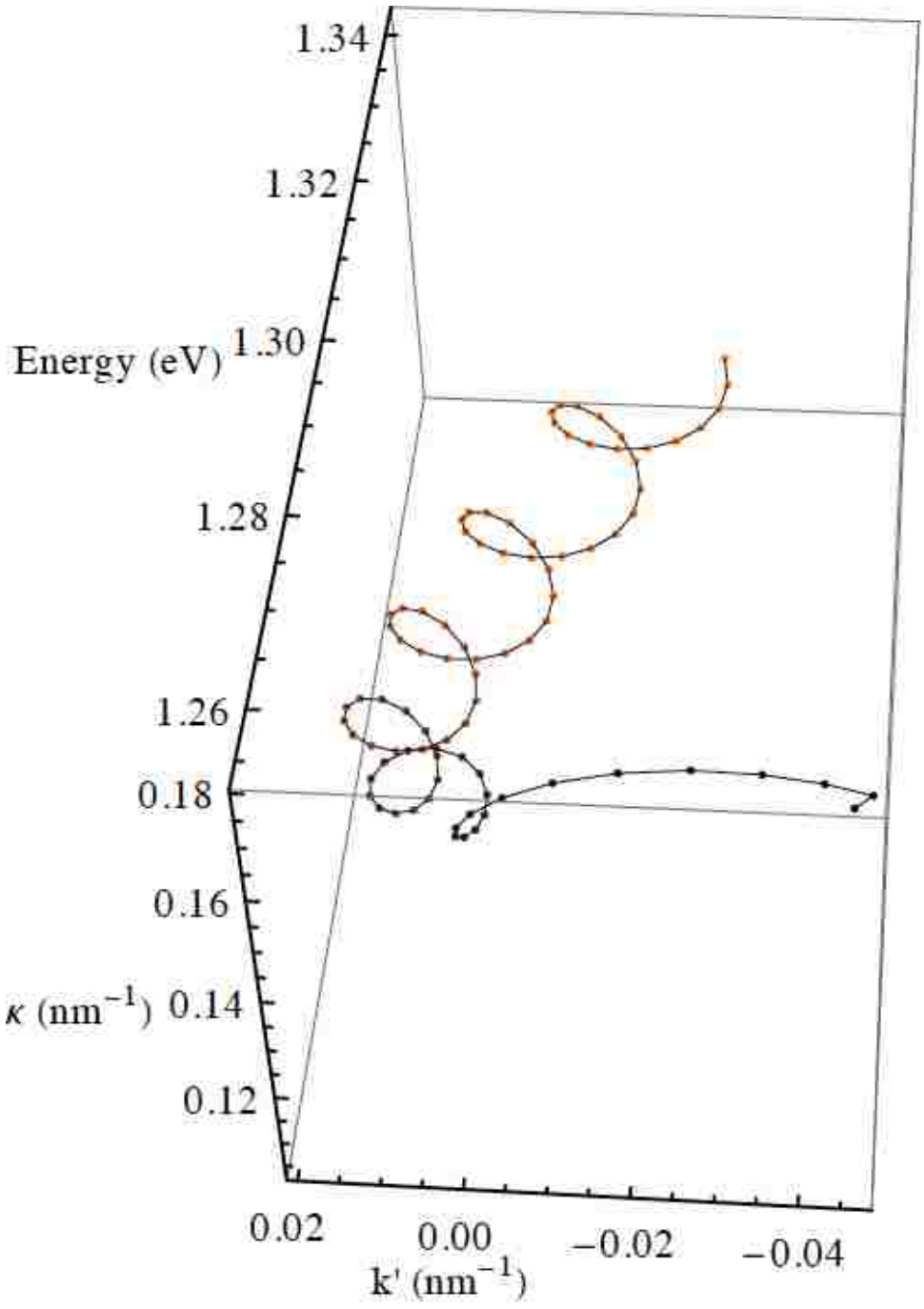

Figure 4.21: A 3D Argand plot of the complex wave vector versus energy. The linear dispersion of k was subtracted to illustrate the deviations from the linear fit.

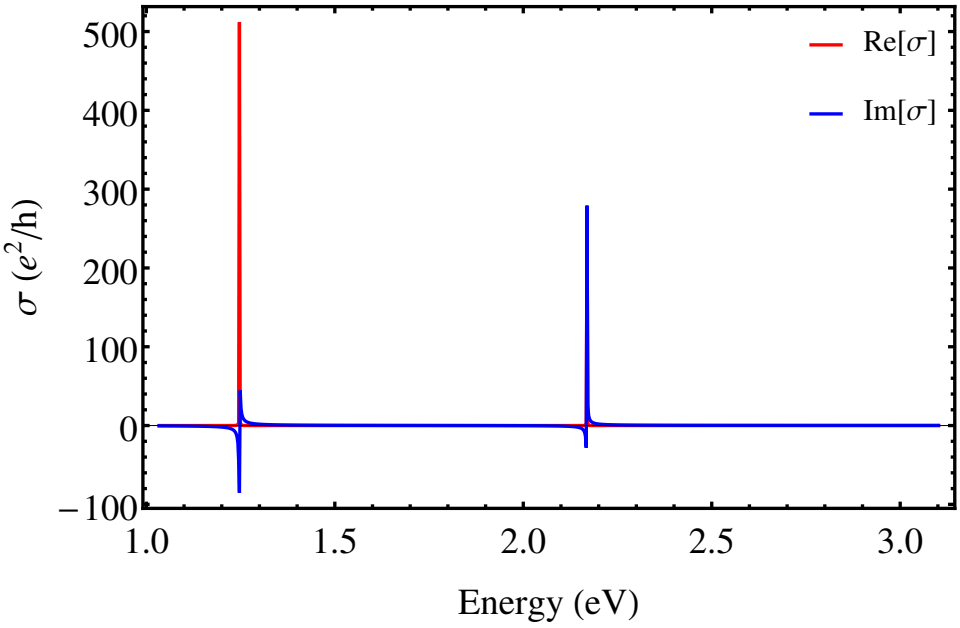

Figure 4.22: Excitonic conductivity for Q = 1000. The transitions are now very sharp peaks.

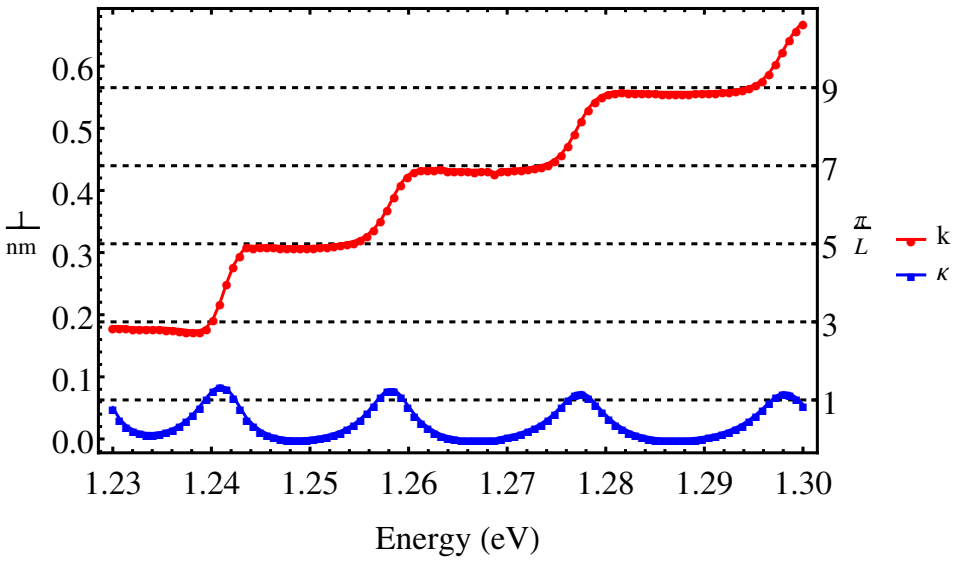

Figure 4.23: Dependence of k and κ versus energy for Q = 1000.

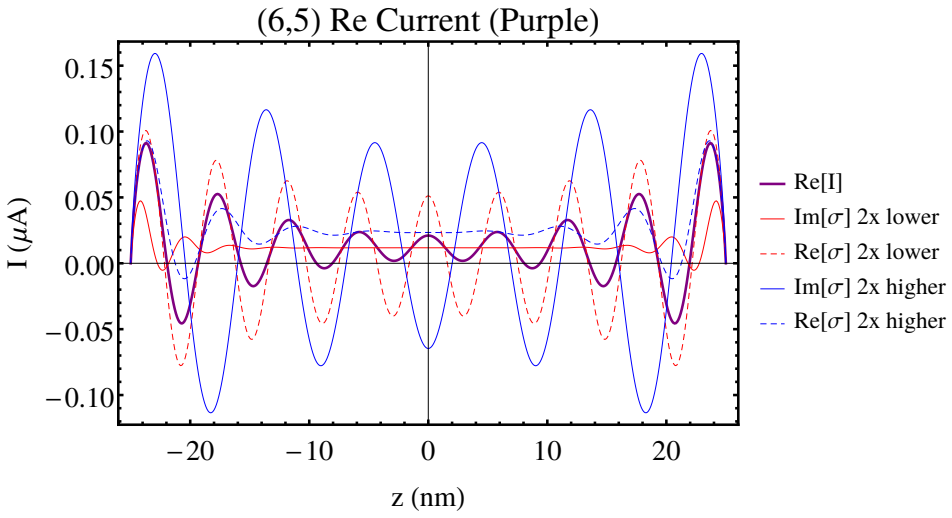

Figure 4.24: Behavior of the real part of the (6,5) current distribution at 1.35 eV with changing real and imaginary parts of the exciton conductivity.

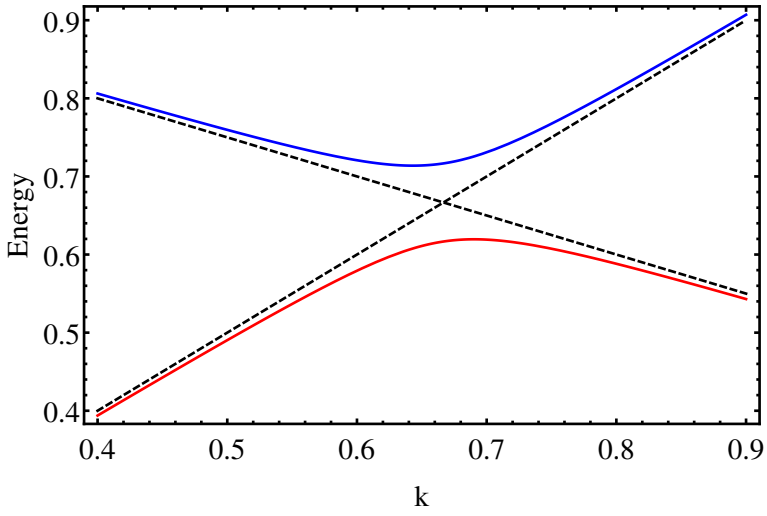

Figure 4.25: Anti-crossing of two quantum states. The parameters used in this calculation are $\epsilon_1 = 1 - k/2$, $\epsilon_2 = k$, $\gamma_1 = 0$, $\gamma_2 = 0$, and $g = 0.05$.

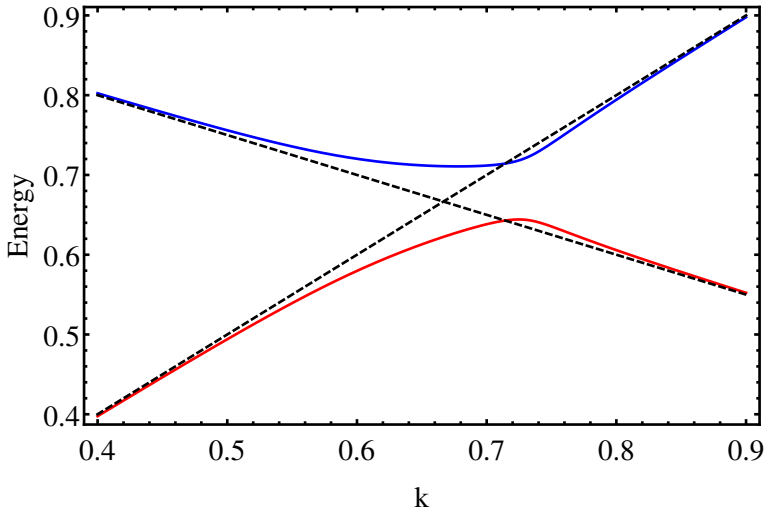

Figure 4.26: Energy behavior of a two level system with small imaginary components. The parameters used in this calculation are $\epsilon_1 = 1 - k/2$, $\epsilon_2 = k$, $\gamma_1 = 0.7$, $\gamma_2 = 1.1\gamma_1$, and $g = (1 + i)0.05$.

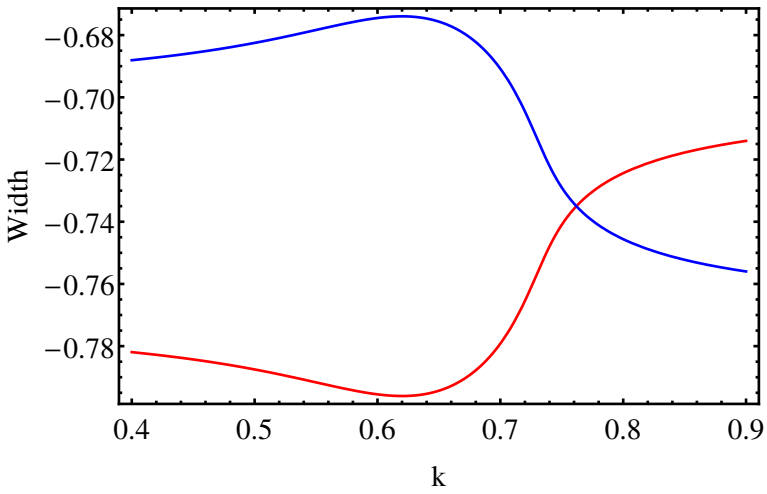

Figure 4.27: Width behavior of a two level system with a small imaginary components. The parameters used in this calculation are $\epsilon_1 = 1 - k/2$, $\epsilon_2 = k$, $\gamma_1 = 0.7$, $\gamma_2 = 1.1\gamma_1$, and $g = (1 + i)0.05$.

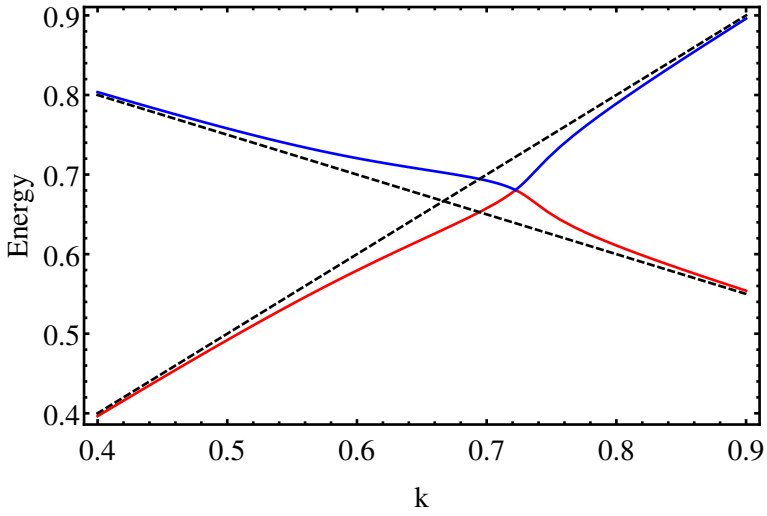

Figure 4.28: Energy behavior of a two level system with large imaginary components. The parameters used in this calculation are $\epsilon_1 = 1 - k/2$, $\epsilon_2 = k$, $\gamma_1 = 1.2$, $\gamma_2 = 1.1\gamma_1$, and $g = (1 + i)0.05$.

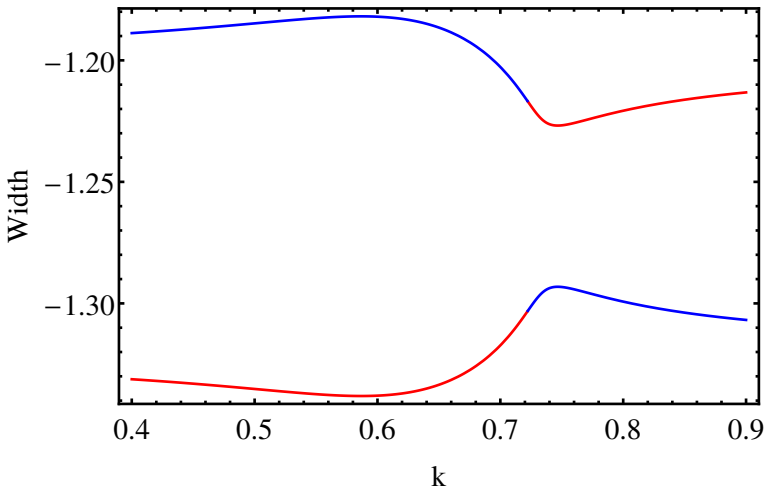

Figure 4.29: Width behavior of a two level system with a large imaginary components. The parameters used in this calculation are $\epsilon_1 = 1 - k/2$, $\epsilon_2 = k$, $\gamma_1 = 1.2$, $\gamma_2 = 1.1\gamma_1$, and $g = (1 + i)0.05$.

4.6 Discussion

We were able to calculate the scattered electric fields from a SWNT antenna by solving an integral equation for the induced current distribution. The scattered fields generated localized hotspots of field intensity in the near-field of the SWNT antenna. REIs sitting in these hotspots could experience excitation enhancements upwards of 200%.

The behavior we observe with the current distributions over the frequency range of the S_1 and S_2 SWNT transitions resembles what Scully observed [124]. He saw that the resonant transition wave vector has a cutoff between the superradiance regime and the radiation trapping regime. Here, we observe that once the frequency of light is greater than the transition frequency, oscillations occur as can be seen in Figure 4.15. In this range, $\mathrm{Re}[\sigma(\omega)] > 0$ which means that the SWNT creates gain for light quanta.

Our fitting procedure of using a complex exponential function with complex wave vector $\mathcal{K} = k + i\kappa$ resembles what Dubovskii saw in his dispersion relation for the 1D crystal in Equation (4.5). There, he saw a dependence on a complex frequency corresponding to damped solutions as we see above the excitonic resonances. It is likely that the quantization of $k \propto \pi/L$ is similar in our case to Fabri-Perot modes of a 1D resonator, a wave guide, a fiber, or most closely related to an open antenna resonator. Such antenna resonances are being enhanced in the region where the antenna medium has a positive gain.

A recent experiment on Boron Nitride nanotubes (BNNTs) observed phonon-polariton resonances [131]. The behavior of the dielectric function for the phonon resonances in these experiments was similar to our excitonic dielectric function, although in a different frequency range. They used scattering based scanning near field optical microscopy (s-SNOM) to visualize the mid-IR phonon polaritons. What they observed was that below the phonon resonance, they saw no propagating polariton modes. However, upon crossing the resonance, they saw the appearance of standing wave modes which they classified as phonon polariton modes which exist within the Reststrahlen band.

We calculate that below the exciton resonance, no oscillations are observed. When passing the resonance, we see the formation of standing wave patterns along the surface of the SWNT that decrease in wavelength as the frequency is increased. This is similar to what Xu, et al. saw with the BNNT phonon polaritons. As they increased the excitation frequency, the oscillatory modes decreased in wavelength, as well.

Therefore, we have come to the conclusion that what we are calculating are exciton-polariton modes. The photon is coupling the exciton with the antenna resonances to form the polaritonic modes. These modes can be calculated in the region where the real part of the dielectric function is negative which agrees with previous work done on phonon-polaritons.

Chapter 5

Conclusions and Future Work

In Chapter 3, we derived an analytic model for SWNT surface plasmons by treating the SWNT as a transmission line. The results of this model illustrate that the model indeed replicates the plasmon resonances on SWNTs with less computational expense than more rigorous, numerical models. However, because the plasmon resonant frequencies for SWNTs are in the THz range, they do not contribute to any enhancements for excitations with visible/NIR frequencies for REI applications.

Since we have a working model, there are two directions this project can go in the future. The first is to continue using the model for SWNT plasmons and find other ions/molecules/dyes that could have resonant frequencies closer to the THz range. The other direction is to replace the SWNT with a different material. Materials such as gold or silver nanowires, or even boron nitride nanotubes will have different plasmon resonant frequencies. Doing this would require changing the TL parameters for each different material and calculating the plasmon resonance frequencies. If any of those materials have resonances in the visible or NIR, then they can be used with the REIs to see what mangitude of enhancements can be seen. If the resonances are elsewhere, one could find molecules or dyes that have similar resonance frequencies.

In Chapter 4, we derived a numerical model for calculating the induced current distribution on the surface of the SWNT including excitonic resonances for use in the visible and NIR range to couple with the REIs. By incorporating a semi-classical, analytic model for the excitonic conductivity, we were able to calculate the

scattered fields around the SWNT antenna. We found hotspots of field enhancement around the antenna and were able to calculate the excitation enhancements of REI transitions for various chirality SWNTs. Excitation enhancements of over 200% were calculated for particular transitions.

In addition to the REI enhancements, we also observed oscillatory behavior of the current distributions in the region of gain in the response function of the exciton resonances. This behavior resembles that of superradiance and radiation trapping as calculated by Holstein [118, 119], Dubovskii [121], and Scully [124]. It also resembles the behavior of phonon polaritons in BNNTs as measured by Xu, et al [131]. Therefore, we conclude that the oscillatory behavior we are calculating are due to exciton-polariton modes. The photon is coupling the exciton modes with the antenna resonance modes to form the polariton.

The next step in this project would be to further analyze the polaritonic modes. Also, an approximate analytical expression for the current distribution could be obtained and used to explain what we see in the dispersion and compare to the dispersion equation calculated by Dubovskii [121].

Our model can also apply to BNNTs to simulate the phonon polariton modes Xu observed [131]. Our model needs to be altered to account for the thick, multi-walled structure of the BNNTs as compared to the the single layer structure of the SWNT.

An additional step in this project would be to include non-radiative decay channels for the REIs. So far, we have only considered excitation enhancements. However, once REIs are excited, they non-radiatively recombine to a lower energy level before re-emitting a photon. Including these non-radiative recombinations will allow us to calculate the full PL enhancement of the REI in the presence of the SWNT antenna.

Also, thus far we have not considered that a REI sitting in these enhanced fields will experience a shift in energy levels (Stark splitting). The energy levels used here were the free-ion energy levels of REIs in aqueous solution. Experiencing such large electric fields will surely alter their energy level structures. Calculations will need to be performed to see if these fields can be treated perturbitavely. If so, perturbative methods can be applied. If not, we must consider adding an electric field term to

the REI Hamiltonian. Solving that Hamiltonian will not be an easy task since just solving the free-ion Hamiltonian with the crystal field perturbation is not a simple thing to do.

One more aspect that we have not considered up to this point is the shifting of exciton transition frequencies due to changes in the dielectric environment. Placing a REI in the near field of the SWNT antenna will alter the potential felt by the exciton. This potential could either scatter the exciton or trap it in a bound state local to the position of the REI as seen in Ref [109]. The resonant frequencies of the excitons on the SWNT antenna may also change over the length of the tube, depending on the specific environment it is sitting in. A more accurate approach would be to apply the formalism of Section 2.3.9 to calculate the shifts in energy due to the presence of the REI. This is not a simple adjustment to make to the model and the exact method on how to properly apply it will require some thought and time.

Source code for all calculations is available upon request.

Bibliography

[1] Riichiro Saito, Gene Dresselhaus, and Mildred S. Dresselhaus, editors. *Physical Properties of Carbon Nanotubes*. Imperial College Press, 1998.

[2] W.T. Carnall. The absorption and fluorescence spectra of rare earth ions in solution. In Jr Karl A. Gschneidnet and LeRoy Eyring, editors, *Handbook on the Physics and Chemistry of Rare Earths*, volume 3, pages 171–208. North-Holland Publishing Co., 1979.

[3] John L. Kropp and Maurice W. Windsor. Luminescence and energy transfer in solutions of rareearth complexes. i. enhancement of fluorescence by deuterium substitution. *The Journal of Chemical Physics*, 42(5):1599–1608, 1965.

[4] N. A. Kazanskaya and E. B. Sveshnikova. *Opt. Spektrosk.*, 28:699, 1970.

[5] W.T. Carnall, P.R. Fields, and K. Rajnak. Electronic energy levels of the trivalent lanthanide aquo ions. iii. tb3+. *J. Chem. Phys.*, 49:4447–4449, 1968.

[6] Tetyana Ignatova, Hikmat Najafov, Aleksandr Ryasnyanskiy, Ivan Biaggio, Ming Zheng, and Slava V. Rotkin. Significant fret between swnt/dna and rare earth ions: A signature of their spatial correlations. *ACS Nano*, 5(7):6052–6059, 2011.

[7] Jason K. Streit, Sergei M. Bachilo, Saunab Ghosh, Ching-Wei Lin, and R. Bruce Weisman. Directly measured optical absorption cross sections for structure-selected single-walled carbon nanotubes. *Nano Letters*, 14(3):1530–1536, 2014.

[8] A. K. Geim and K. S. Novoselov. The rise of graphene. *Nature Materials*, 6:183 – 191, 2007.

[9] Eduardo B. Barros, Ado Jorio, Georgii G. Samsonidze, Rodrigo B. Capaz, Antonio G. Souza Filho, Josué Mendes Filho, Gene Dresselhaus, and Mildred S. Dresselhaus. Review on the symmetry-related properties of carbon nanotubes. *Physics Reports*, 431(6):261 – 302, 2006.

[10] Ermin Malić, Matthias Hirtschulz, Frank Milde, Marten Richter, Janina Maultzsch, Stephanie Reich, and Andreas Knorr. Coulomb effects in single-walled carbon nanotubes. *physica status solidi (b)*, 245(10):2155–2158, 2008.

[11] Tetyana Ignatova. *Photophysical properties and interactions in Single Wall Nanotube - DNA - Rare Earth systems*. PhD thesis, Lehigh University, 2014.

[12] Daniel Roxbury, Prakrit V. Jena, Yosi Shamay, Christopher P. Horoszko, and Daniel A. Heller. Cell membrane proteins modulate the carbon nanotube optical bandgap via surface charge accumulation. *ACS Nano*, 10(1):499–506, 2016.

[13] Lukas Novotny and Bert Hecht. *Principles of Nano-Optics*. Cambridge University Press, 2006.

[14] J M Pitarke, V M Silkin, E V Chulkov, and P M Echenique. Theory of surface plasmons and surface-plasmon polaritons. *Reports on Progress in Physics*, 70(1):1, 2007.

[15] Qi Zhang, Erik H. Hroz, Zehua Jin, Lei Ren, Xuan Wang, Rolf S. Arvidson, Andreas Lttge, and Junichiro Kono. Plasmonic nature of the terahertz conductivity peak in single-wall carbon nanotubes. *Nano Letters*, 13(12):5991–5996, 2013.

[16] Roger Bacon. Growth, structure, and properties of graphite whiskers. *Journal of Applied Physics*, 31(2):283–290, 1960.

[17] H.W. Kroto, J.R. Heath, S.C. O'Brien, R.F. Curl, and R.E. Smalley. C60: Buckminsterfullerene. *Nature*, 318:162–163, 1985.

[18] S. Iijima. Helical microtubules of graphitic carbon. *Nature*, 354:56–58, 1991.

[19] Alexandra M. Mnzer, Wanji Seo, Gregory J. Morgan, Zachary P. Michael, Yong Zhao, Katharina Melzer, Giuseppe Scarpa, and Alexander Star. Sensing reversible proteinligand interactions with single-walled carbon nanotube field-effect transistors. *The Journal of Physical Chemistry C*, 118(31):17193–17199, 2014.

[20] Mitchell B. Lerner, Jennifer Dailey, Brett R. Goldsmith, Dustin Brisson, and A.T.C. Johnson. Detecting lyme disease using antibody-functionalized single-walled carbon nanotube transistors. *Biosensors and Bioelectronics*, 45:163–167, 2013.

[21] Jun Li and Nianqiang Wu, editors. *Biosensors Based on Nanomaterials and Nanodevices*. CRC Press, 2013.

[22] Chao Gao, Zheng Guo, Jin-Huai Liu, and Xing-Jiu Huang. The new age of carbon nanotubes: An updated review of functionalized carbon nanotubes in electrochemical sensors. *Nanoscale*, 4:1948–1963, 2012.

[23] Christopher B. Jacobs, M. Jennifer Peairs, and B. Jill Venton. Review: Carbon nanotube based electrochemical sensors for biomolecules. *Analytica Chimica Acta*, 662(2):105 – 127, 2010.

[24] Yongki Choi, Tivoli J. Olsen, Patrick C. Sims, Issa S. Moody, Brad L. Corso, Mytrang N. Dang, Gregory A. Weiss, and Philip G. Collins. Dissecting single-molecule signal transduction in carbon nanotube circuits with protein engineering. *Nano Letters*, 13(2):625–631, 2013.

[25] Philip G. Collins, Keith Bradley, Masa Ishigami, and A. Zettl. Extreme oxygen sensitivity of electronic properties of carbon nanotubes. *Science*, 287(5459):1801–1804, 2000.

[26] Tivoli J. Olsen, Yongki Choi, Patrick C. Sims, O. Tolga Gul, Brad L. Corso, Chengjun Dong, William A. Brown, Philip G. Collins, and Gregory A. Weiss. Electronic measurements of single-molecule processing by dna polymerase i (klenow fragment). *Journal of the American Chemical Society*, 135(21):7855–7860, 2013.

[27] Lu Zhu, Cheng Deng, Ping Chen, Xiu dong You, Hong bo Su, Ying hai Yuan, and Meng fu Zhu. Glucose oxidase biosensors based on carbon nanotube nonwoven fabrics. *Carbon*, 67:795 – 796, 2014.

[28] Ling Tong, Yuxiang Liu, Bridget D. Dolash, Yookyung Jung, Mikhail N. Slipchenko, Donald E. Bergstrom, and Ji-Xin Cheng. Label-free imaging of semiconducting and metallic carbon nanotubes in cells and mice using transient absorption microscopy. *Nature Nanotechnology*, 7:56–61, 2012.

[29] Kevin Welsher, Zhuang Liu, Sarah P. Sherlock, Joshua Tucker Robinson, Zhuo Chen, Dan Daranciang, and Hongjie Dai. A route to brightly fluorescent carbon nanotubes for near-infrared imaging in mice. *Nature Nanotechnology*, 4:773–780, 2009.

[30] M. Ito, T. Kobayashi, Y. Ito, T. Hayashida, D. Nii, K. Umemura, and Y. Homma. Intense photoluminescence from dried double-stranded dna and single-walled carbon nanotube hybrid. *Applied Physics Letters*, 104(4), 2014.

[31] Joshua T. Robinson, Guosong Hong, Yongye Liang, Bo Zhang, Omar K. Yaghi, and Hongjie Dai. In vivo fluorescence imaging in the second near-infrared window with long circulating carbon nanotubes capable of ultrahigh tumor uptake. *Journal of the American Chemical Society*, 134(25):10664–10669, 2012.

[32] Jingqing Zhang, Sebastian Kruss, Andrew J. Hilmer, Steven Shimizu, Zeke Schmois, Flor De La Cruz, Paul W. Barone, Nigel F. Reuel, Daniel A. Heller, and Michael S. Strano. A rapid, direct, quantitative, and label-free detector of cardiac biomarker troponin t using near-infrared fluorescent single-walled carbon nanotube sensors. *Advanced Healthcare Materials*, 3(3):412–423, 2014.

[33] Prakrit V. Jena, Yosi Shamay, Janki Shah, Daniel Roxbury, Navid Paknejad, and Daniel A. Heller. Photoluminescent carbon nanotubes interrogate the permeability of multicellular tumor spheroids. *Carbon*, 97:99 – 109, 2016.

[34] Daniel Roxbury, Prakrit V. Jena, Ryan M. Williams, Balázs Enyedi, Philipp Niethammer, Stéphane Marcet, Marc Verhaegen, Sébastien Blais-Ouellette, and Daniel A. Heller. Hyperspectral microscopy of near-infrared fluorescence enables 17-chirality carbon nanotube imaging. *Scientific Reports*, 5(14167), 2015.

[35] Eike Verdenhalven and Ermin Malić. Excitonic absorption intensity of semiconducting and metallic carbon nanotubes. *Journal of Physics: Condensed Matter*, 25(24):245302, 2013.

[36] Larry Lüer, Sajjad Hoseinkhani, Dario Polli, Jared Crochet, Tobias Hertel, and Guglielmo Lanzani. Size and mobility of excitons in (6, 5) carbon nanotubes. *Nature Physics*, 5:54–58, 2009.

[37] Friedrich Schppler, Christoph Mann, Tilman C. Hain, Felix M. Neubauer, Giulia Privitera, Francesco Bonaccorso, Daping Chu, Andrea C. Ferrari, and Tobias Hertel. Molar extinction coefficient of single-wall carbon nanotubes. *The Journal of Physical Chemistry C*, 115(30):14682–14686, 2011.

[38] Tetyana Ignatova, Alexander Balaeff, Michael Blades, Ming Zheng, Peter Stoeckl, and Slava V. Rotkin. Two-color spectroscopy of uv excited ssdna complex with a single-wall nanotube photoluminescence probe: Fast relaxation by nucleobase autoionization mechanism. *Nano Research*, 9(2):571–583, 2016.

[39] Stefan A. Maier. *Plasmonics: Fundamentals and Applications*. Springer, 2007.

[40] A. Pekker and K. Kamarás. Wide-range optical studies on various single-walled carbon nanotubes: Origin of the low-energy gap. *Phys. Rev. B*, 84:075475, 2011.

[41] C. L. Kane and E. J. Mele. Size, shape, and low energy electronic structure of carbon nanotubes. *Phys. Rev. Lett.*, 78:1932, 1997.

[42] Ugawa A., Rinzler A. G., and Tanner D. B. Far-infrared gaps in single-wall carbon nanotubes. *Phys. Rev. B*, 60:R11305, 1999.

[43] Borondics F., Kamars K., Nikolou M., Tanner D. B., Chen Z. H., and Rinzler A. G. Charge dynamics in transparent single-walled carbon nanotube films from optical transmission measurements. *Phys. Rev. B*, 74:045431, 2006.

[44] H. Nishimura, N. Minami, and R. Shimano. Dielectric properties of single-walled carbon nanotubes in the terahertz frequency range. *Appl. Phys. Lett.*, 91:011108, 2007.

[45] T. Kampfrath, K. von Volkmann, C. M. Aguirre, P. Desjardins, R. Martel, M. Krenz, C. Frischkorn, M. Wolf, and L. Perfetti. Mechanism of the far-infrared absorption of carbon-nanotube films. *Phys. Rev. Lett.*, 101:267403, 2008.

[46] N. Hamada, S. Sawada, and A. Oshiyama. New one-dimensional conductors: Graphitic microtubules. *Phys. Rev. Lett.*, 68:1579, 1992.

[47] T.-I. Jeon, K.-J. Kim, C. Kang, S.-J. Oh, J.-H. Son, K. H. An, D. J. Bae, and Y. H. Lee. Terahertz conductivity of anisotropic single walled carbon nanotube films. *Appl. Phys. Lett.*, 80:3403, 2002.

[48] N. Akima, Y. Iwasa, S. Brown, A. M. Barbour, J. Cao, J. L. Musfeldt, H. Matsui, N. Toyota, M. Shiraishi, H. Shimoda, and O. Zhou. Strong anisotropy in the far-infrared absorption spectra of stretch-aligned single-walled carbon nanotubes. *Adv. Mater.*, 18:1166, 2006.

[49] G. Y. Slepyan, M. V. Shuba, S. A. Maksimenko, C. Thomsen, and A. Lakhtakia. Terahertz conductivity peak in composite materials containing carbon nanotubes: Theory and interpretation of experiment. *Phys. Rev. B*, 81:205423, 2010.

[50] M. V. Shuba, A. G. Paddubskaya, A. O. Plyushch, P. P. Kuzhir, G. Y. Slepyan, S. A. Maksimenko, V. K. Ksenevich, P. Buka, D. Seliuta, I. Kasalynas, J. Macutkevic, G. Valusis, C. Thomsen, and A. Lakhtakia. Experimental evidence of localized plasmon resonance in composite materials containing single-wall carbon nanotubes. *Phys. Rev. B*, 85:165435, 2012.

[51] Takeshi Nakanishi and Tsuneya Ando. Optical response of finite-length carbon nanotubes. *Journal of the Physical Society of Japan*, 78(11):114708, 2009.

[52] Takahiro Morimoto, Soon-Kil Joung, Takeshi Saito, Don N. Futaba, Kenji Hata, and Toshiya Okazaki. Length-dependent plasmon resonance in single-walled carbon nanotubes. *ACS Nano*, 8(10):9897–9904, 2014.

[53] Th. Förster. Zwischenmolekulare energiewanderung und fluoreszenz. *Annalen der Physik*, 437(1-2):55–75, 1948.

[54] D. L. Dexter. A theory of sensitized luminescence in solids. *The Journal of Chemical Physics*, 21(5):836–850, 1953.

[55] David L. Andrews. *Resonance Energy Transfer: Theoretical Foundations and Developing Applications*, chapter 14. SPIE Press, 2009.

[56] Joel I. Gersten and Abraham Nitzan. Accelerated energy transfer between molecules near a solid particle. *Chemical Physics Letters*, 104(1):31 – 37, 1984.

[57] X. M. Hua, J. I. Gersten, and A. Nitzan. Theory of energy transfer between molecules near solid state particles. *The Journal of Chemical Physics*, 83(7):3650–3659, 1985.

[58] Tian Ming, Huanjun Chen, Ruibin Jiang, Qian Li, and Jianfang Wang. Plasmon-controlled fluorescence: Beyond the intensity enhancement. *The Journal of Physical Chemistry Letters*, 3(2):191–202, 2012.

[59] Lei Zhao, Tian Ming, Lei Shao, Huanjun Chen, and Jianfang Wang. Plasmon-controlled förster resonance energy transfer. *The Journal of Physical Chemistry C*, 116(14):8287–8296, 2012.

[60] Manuela Lunz, Xia Zhang, Valerie A. Gerard, Yurii K. Gunko, Vladimir Lesnyak, Nikolai Gaponik, Andrei S. Susha, Andrey L. Rogach, and A. Louise Bradley. Effect of metal nanoparticle concentration on localized surface plasmon mediated förster resonant energy transfer. *The Journal of Physical Chemistry C*, 116(50):26529–26534, 2012.

[61] Xia Zhang, Cristian A. Marocico, Manuela Lunz, Valerie A. Gerard, Yurii K. Gunko, Vladimir Lesnyak, Nikolai Gaponik, Andrei S. Susha, Andrey L. Rogach, and A. Louise Bradley. Experimental and theoretical investigation of the distance dependence of localized surface plasmon coupled förster resonance energy transfer. *ACS Nano*, 8(2):1273–1283, 2014.

[62] Jean-Claude G. Bunzli and Claude Piguet. Taking advantage of luminescent lanthanide ions. *Chem. Soc. Rev.*, 34:1048–1077, 2005.

[63] Changxia Sun, Jinghe Yang, Lei Li, Xia Wu, Yang Liu, and Shufang Liu. Advances in the study of luminescence probes for proteins. *Journal of Chromatography B*, 803(2):173 – 190, 2004.

[64] Artur S. Gouveia-Neto, Andra F. da Silva, Luciano A. Bueno, and Ernande B. Costa. Luminescent features of novel sol-gel derived lanthanide multi-doped oxyfluoride nano-structured phosphors for white led. *Proc. SPIE*, 7954:795412–795412–8, 2011.

[65] Ki Hyuk Kwon, Won Bin Im, Ho Seong Jang, Hyoung Sun Yoo, and Duk Young Jeon. Luminescence properties and energy transfer of site-sensitive ca6xymgxz(po4)4:euy2+,mnz2+ phosphors and their application to near-uv led-based white leds. *Inorganic Chemistry*, 48(24):11525–11532, 2009.

[66] U Hoemmerich, Ei Ei Nyein, D.S Lee, J Heikenfeld, A.J Steckl, and J.M Zavada. Photoluminescence studies of rare earth (er, eu, tm) in situ doped gan. *Materials Science and Engineering: B*, 105(13):91 – 96, 2003.

[67] Lianhua Tian, Byung-Yong Yu, Chong-Hong Pyun, Hong Lee Park, and Sun il Mho. New red phosphors bazr(bo3)2 and sral2b2o7 doped with eu3+ for {PDP} applications. *Solid State Communications*, 129(1):43 – 46, 2004.

[68] Hai-Qiao Wang, Miroslaw Batentschuk, Andres Osvet, Luigi Pinna, and Christoph J. Brabec. Rare-earth ion doped up-conversion materials for photovoltaic applications. *Advanced Materials*, 23(22-23):2675–2680, 2011.

[69] Bryan M. van der Ende, Linda Aarts, and Andries Meijerink. Lanthanide ions as spectral converters for solar cells. *Phys. Chem. Chem. Phys.*, 11:11081–11095, 2009.

[70] C. Struempel, M. McCann, G. Beaucarne, V. Arkhipov, A. Slaoui, V. Svrcek, C. del Canizo, and I. Tobias. Modifying the solar spectrum to enhance silicon solar cell efficiencyan overview of available materials. *Solar Energy Materials and Solar Cells*, 91(4):238 – 249, 2007.

[71] B.S. Richards. Luminescent layers for enhanced silicon solar cell performance: Down-conversion. *Solar Energy Materials and Solar Cells*, 90(9):1189 – 1207, 2006.

[72] Donald L. Chubb and David S. Wolford. Rare earth optical temperature sensor. *Review of Scientific Instruments*, 71(5):2233–2240, 2000.

[73] B.G. Potter and M.B. Sinclair. Photosensitive and rare-earth doped ceramics for optical sensing: A review. *Journal of Electroceramics*, 2(4):295–308, 1998.

[74] Chao Zhao, Yujun Song, Konggang Qu, Jinsong Ren, and Xiaogang Qu. Luminescent rare-earth complex covalently modified single-walled carbon nanotubes: Design, synthesis, and dna sequence-dependent red luminescence enhancement. *Chemistry of Materials*, 22(20):5718–5724, 2010.

[75] Tianzhi Yu, Jing Meng, Yuling Zhao, Hui Zhang, Xiaoqian Han, and Duowang Fan. Synthesis and rare earth metal ion-sensing properties of aza-crown derivative incorporating with diaryl-1,3,4-oxadiazole. *Spectrochimica Acta Part A: Molecular and Biomolecular Spectroscopy*, 78(1):396 – 400, 2011.

[76] Roger Y. Tsien, Lauren Ernst, and Alan Waggoner. *Fluorophores for Confocal Microscopy: Photophysics and Photochemistry*, pages 338–352. Springer US, Boston, MA, 2006.

[77] Scott L. Klakamp and William DeW. Horrocks. Lanthanide ion luminescence as a probe of dna structure. 1. guanine-containing oligomers and nucleotides. *Journal of Inorganic Biochemistry*, 46(3):175 – 192, 1992.

[78] B. R. Judd. Optical absorption intensities of rare-earth ions. *Phys. Rev.*, 127:750–761, Aug 1962.

[79] G. S. Ofelt. Intensities of crystal spectra of rareearth ions. *The Journal of Chemical Physics*, 37(3):511–520, 1962.

[80] Brian M. Walsh. Judd-ofelt theory: principles and practices. In Baldassare Bartolo and Ottavio Forte, editors, *Advances in Spectroscopy for Lasers and Sensing*, pages 403–433. Springer Netherlands, 2006.

[81] Alexander A. Kaminskii. *Crystalline Lasers: Physical Processes and Operating Schemes*. CRC Press, 1996.

[82] B. R. Judd. Three-particle operators for equivalent electrons. *Phys. Rev.*, 141:4–14, Jan 1966.

[83] Argyrios Malapanis, Vasili Perebeinos, Dhiraj Prasad Sinha, Everett Comfort, and Ji Ung Lee. Quantum efficiency and capture cross section of first and second excitonic transitions of single-walled carbon nanotubes measured through photoconductivity. *Nano Letters*, 13(8):3531–3538, 2013.

[84] Feng Wang, David J. Cho, Brian Kessler, Jack Deslippe, P. James Schuck, Steven G. Louie, Alex Zettl, Tony F. Heinz, and Y. Ron Shen. Observation of excitons in one-dimensional metallic single-walled carbon nanotubes. *Phys. Rev. Lett.*, 99:227401, Nov 2007.

[85] Kaihui Liu, Xiaoping Hong, Sangkook Choi, Chenhao Jin, Rodrigo B. Capaz, Jihoon Kim, Wenlong Wang, Xuedong Bai, Steven G. Louie, Enge Wang, and Feng Wang. Systematic determination of absolute absorption cross-section of individual carbon nanotubes. *Proceedings of the National Academy of Sciences*, 111(21):7564–7569, 2014.

[86] Olga A. Dyatlova, Jordi Gomis-Bresco, Ermin Malic, Hagen Telg, Janina Maultzsch, Guofang Zhong, Junfeng Geng, and Ulrike Woggon. Dielectric screening effects on transition energies in aligned carbon nanotubes. *Phys. Rev. B*, 85:245449, Jun 2012.

[87] J. Lefebvre, J.M. Fraser, Y. Homma, and P. Finnie. Photoluminescence from single-walled carbon nanotubes: a comparison between suspended and micelle-encapsulated nanotubes. *Applied Physics A*, 78(8):1107–1110, 2004.

[88] Kaihui Liu, Jack Deslippe, Fajun Xiao, Rodrigo B. Capaz, Xiaoping Hong, Shaul Aloni, Alex Zettl, Wenlong Wang, Xuedong Bai, Steven G. Louie, Enge Wang, and Feng Wang. An atlas of carbon nanotube optical transitions. *Nature Nanotechnology*, 7:325–329, April 2012.

[89] C. Fantini, A. Jorio, M. Souza, M. S. Strano, M. S. Dresselhaus, and M. A. Pimenta. Optical transition energies for carbon nanotubes from resonant raman spectroscopy: Environment and temperature effects. *Phys. Rev. Lett.*, 93:147406, Sep 2004.

[90] Sofie Cambré, Silvia M. Santos, Wim Wenseleers, Ahmad R. T. Nugraha, Riichiro Saito, Laurent Cognet, and Brahim Lounis. Luminescence properties of individual empty and water-filled single-walled carbon nanotubes. *ACS Nano*, 6(3):2649–2655, 2012.

[91] Christoph Mann and Tobias Hertel. 13 nm exciton size in (6,5) single-wall carbon nanotubes. *The Journal of Physical Chemistry Letters*, 7(12):2276–2280, 2016.

[92] J. Jiang, R. Saito, Ge. G. Samsonidze, A. Jorio, S. G. Chou, G. Dresselhaus, and M. S. Dresselhaus. Chirality dependence of exciton effects in single-wall carbon nanotubes: Tight-binding model. *Phys. Rev. B*, 75:035407, Jan 2007.

[93] Mildred S. Dresselhaus, Gene Dresselhaus, Riichiro Saito, and Ado Jorio. Exciton photophysics of carbon nanotubes. *Annual Review of Physical Chemistry*, 58(1):719–747, 2007.

[94] Ermin Malić, Janina Maultzsch, Stephanie Reich, and Andreas Knorr. Excitonic absorption spectra of metallic single-walled carbon nanotubes. *Phys. Rev. B*, 82:035433, Jul 2010.

[95] C. Thomsen, S. Reich, and J. Maultzsch, editors. *Carbon Nanotubes: Basic Concepts and Physical Properties*. Berlin: Wiley-VCH, 2004.

[96] Hiroshi Ajiki and Tsuneya Ando. Electronic states of carbon nanotubes. *Journal of the Physical Society of Japan*, 62(4):1255–1266, 1993.

[97] Tsuneya Ando. Excitons in carbon nanotubes. *Journal of the Physical Society of Japan*, 66(4):1066–1073, 1997.

[98] Tsuneya Ando. Theory of electronic states and transport in carbon nanotubes. *Journal of the Physical Society of Japan*, 74(3):777–817, 2005.

[99] S. V. Goupalov, A. Zarifi, and T. G. Pedersen. Calculation of optical matrix elements in carbon nanotubes. *Phys. Rev. B*, 81:153402, Apr 2010.

[100] S. V. Goupalov. Fine structure of exciton levels in carbon nanotubes: A semianalytical approach. *Phys. Rev. B*, 84:125407, Sep 2011.

[101] S.V. Goupalov. Excitons in semiconductor carbon nanotubes: A momentum-space perspective. *Chemical Physics*, 413:20 – 28, 2013. Photophysics of carbon nanotubes and nanotube composites.

[102] Y. Miyauchi, R. Saito, K. Sato, Y. Ohno, S. Iwasaki, T. Mizutani, J. Jiang, and S. Maruyama. Dependence of exciton transition energy of single-walled carbon nanotubes on surrounding dielectric materials. *Chemical Physics Letters*, 442(46):394 – 399, 2007.

[103] A. R. T. Nugraha, R. Saito, K. Sato, P. T. Araujo, A. Jorio, and M. S. Dresselhaus. Dielectric constant model for environmental effects on the exciton energies of single wall carbon nanotubes. *Applied Physics Letters*, 97(9), 2010.

[104] Tsuneya Ando. Environment effects on excitons in semiconducting carbon nanotubes. *Journal of the Physical Society of Japan*, 79(2):024706, 2010.

[105] Seiji Uryu and Tsuneya Ando. Environment effect on cross-polarized excitons in carbon nanotubes. *Phys. Rev. B*, 86:125412, Sep 2012.

[106] Jack Deslippe, Catalin D. Spataru, David Prendergast, and Steven G. Louie. Bound excitons in metallic single-walled carbon nanotubes. *Nano Letters*, 7(6):1626–1630, 2007.

[107] Jesse M. Kinder, Garnet Kin-Lic Chan, and Jiwoong Park. Uniform peak optical conductivity in single-walled carbon nanotubes. *Phys. Rev. B*, 84:125428, Sep 2011.

[108] Vasili Perebeinos, J. Tersoff, and Phaedon Avouris. Scaling of excitons in carbon nanotubes. *Phys. Rev. Lett.*, 92:257402, Jun 2004.

[109] Benjamin O. Tayo and Slava V. Rotkin. Charge impurity as a localization center for singlet excitons in single-wall nanotubes. *Phys. Rev. B*, 86:125431, Sep 2012.

[110] P. J. Burke, Shengdong Li, and Zhen Yu. Quantitative theory of nanowire and nanotube antenna performance. *IEEE Transactions on Nanotechnology*, 5(4):314–334, July 2006.

[111] G. W. Hanson. Fundamental transmitting properties of carbon nanotube antennas. *IEEE Transactions on Antennas and Propagation*, 53(11):3426–3435, Nov 2005.

[112] Sophocles J. Orfanidis. *Electromagnetic Waves and Antennas*. Rutgers University, 2014.

[113] Thomas Rylander, Pär Ingelström, and Anders Bondeson. *Computational Electromagnetics*. Springer Science and Business Media, 2 edition, 2012.

[114] P. Papakanellos, P. Paschalidis, and G. Fikioris. On the extended thin-wire kernel. *IEEE Transactions on Antennas and Propagation*, PP(99), 2016.

[115] G. Ya. Slepyan, M. V. Shuba, S. A. Maksimenko, and A. Lakhtakia. Theory of optical scattering by achiral carbon nanotubes and their potential as optical nanoantennas. *Phys. Rev. B*, 73:195416, May 2006.

[116] Andrei M. Nemilentsau. Tutorial: Linear surface conductivity of an achiral single-wall carbon nanotube. *Journal of Nanophotonics*, 5(1):050401–050401–7, 2011.

[117] Daniel Y. Joh, Jesse Kinder, Lihong H. Herman, Sang-Yong Ju, Michael A. Segal, Jeffreys N. Johnson, Garnet K.-L. Chan, and Jiwoong Park. Single-walled carbon nanotubes as excitonic optical wires. *Nature Nanotechnology*, 6:51–56, Nov 2010.

[118] T. Holstein. Imprisonment of resonance radiation in gases. *Phys. Rev.*, 72:1212–1233, Dec 1947.

[119] T. Holstein. Imprisonment of resonance radiation in gases. ii. *Phys. Rev.*, 83:1159–1168, Sep 1951.

[120] C. Muzikar. Coherence phenomena in the radiation of identical oscillators constituting a crystal. *JETP*, 14(4), April 1962.

[121] O. A. Dubovskii. Superradiance of polaritons in finite one-dimensional crystals of increasing length: Passage from a dimer to an infinite crystal. *Physics of the Solid State*, 40(11):1937–1941, 1998.

[122] V.M. Agranovich. *Theory of Excitons*. Nauka, Moscow, 1968.

[123] A. Davydov. *Theory of Molecular Excitons*. Plenum Press, 1971.

[124] Anatoly A. Svidzinsky, Fu Li, Hongyuan Li, Xiwen Zhang, C. H. Raymond Ooi, and Marlan O. Scully. Single-photon superradiance and radiation trapping by atomic shells. *Phys. Rev. A*, 93:043830, Apr 2016.

[125] Motoaki Bamba and Hajime Ishihara. Qed of excitons with nonlocal susceptibility in arbitrarily structured dielectrics. *Phys. Rev. B*, 78:085109, Aug 2008.

[126] Pascal Anger, Palash Bharadwaj, and Lukas Novotny. Enhancement and quenching of single-molecule fluorescence. *Phys. Rev. Lett.*, 96:113002, Mar 2006.

[127] Tetyana Ignatova, Andrei M. Nemilentsau, and Slava V. Rotkin. *Handbook on Carbon Nano Materials*, chapter Near-field optics of SWNTs and FRET in their nanoscale complexes, pages 287–319. World Scientific Publishing, Inc., 2012.

[128] Zubin Jacob. Hyperbolic phonon polaritons. *Nature Materials*, 13:1081–1083, November 2014.

[129] Kaijun Feng, William Streyer, S. M. Islam, Jai Verma, Debdeep Jena, Daniel Wasserman, and Anthony J. Hoffman. Localized surface phonon polariton resonances in polar gallium nitride. *Applied Physics Letters*, 107(8), 2015.

[130] Joshua D. Caldwell, Lucas Lindsay, Vincenzo Giannini, Igor Vurgaftman, Thomas L. Reinecke, Stefan A. Maier, and Orest J. Glembocki. Low-loss, infrared and terahertz nanophotonics using surface phonon polaritons. *Nanophotonics*, 4, April 2015.

[131] Xiaoji G. Xu, Behnood G. Ghamsari, Jian-Hua Jiang, Leonid Gilburd, Gregory O. Andreev, Chunyi Zhi, Yoshio Bando, Dmitri Golberg, Pierre Berini, and Gilbert C. Walker. One-dimensional surface phonon polaritons in boron nitride nanotubes. *Nature Communications*, 5, August 2014.

Vita

Education

January 2012 - Present

Lehigh University
Doctor of Philosophy
Physics
Graduation date: September 4, 2016

August 2010 - January 2012

Lehigh University
Master of Science
Physics

August 2006 - May 2010

Moravian College
Bachelor of Science
Physics
Graduated with Honors

Teaching Experience

Research Assistant, Lehigh University (June 2016 - Present)
Teaching assistant, Lehigh University (January 2016 - May 2016)

- Taught two sections of PHY 11 Recitation.

Research Assistant, Lehigh University (January 2014 - December 2015)
Teaching assistant, Lehigh University (August 2013 - December 2013)

- Taught two sections of PHY 11 Recitation.

Research Assistant, Lehigh University (June 2012 - August 2013)
Teaching assistant, Lehigh University (August 2010 - May 2012)

- Taught two semesters of PHY 12 labs.
- Taught one semester of PHY 05 lab.
- Taught one semester of PHY 105 lab.

Research experience

Doctoral research conducted with Prof. Slava V. Rotkin
Studying near field electromagnetic interactions of a carbon nanotube/rare earth ion system for bio-sensing applications.
REU Program at the College of William and Mary in Williamsburg, VA (Summer 2009) with Prof. Seth Aubin
Assisted with experiments of Bose-Einstein Condensates. Designed a UV LED circuit to observe and measure the effect of light induced atomic desorption (LIAD) on the Rubidium atoms in the magneto-optical trap to increase the number of trapped atoms for the condensate. Also updated computer code used in controlling the experiments.
Honors Project at Moravian College in Bethlehem, PA (Fall 2009 - Spring 2010) with Prof. Kelly Krieble

"Segregation of Granular Materials in a Viscous Medium" Studied the effects of granular segregation with beads of varying mass vibrated in air and deionized water. Also designed and helped to build the experimental apparatus used in the experiment.

Conferences/Papers

Conference Presentations:

- "Excitonic Contribution to Near-Field Enhancements of a Carbon Nanotube Antenna," American Physical Society March Meeting; Baltimore, MD, 2016 (Oral)
- "Sensitization of Rare Earth Ions With Carbon Nanotube Plasmonic Antennas," Electrochemical Society 227th Meeting; Chicago, IL, 2015 (Oral)

Publications:

- "Near-Field Enhancements of a Carbon Nanotube Excitonic Antenna" (in the process of submission).
- "Optical to Near Infrared Antenna Resonances of Carbon Nanotubes" (in the process of submission).